The Impact of Cerebral Microinfarction on Blood-Brain Barrier Permeability and Behaviour in Mice

Melissa Filadelfi

Thesis submitted to the University of Ottawa
in partial fulfillment of the requirements for the
Master of Science in Neuroscience

Department of Cellular and Molecular Medicine
Faculty of Medicine
University of Ottawa

ABSTRACT

From mid- to late-life aging, many individuals acquire hundreds or even thousands of tiny strokes, known as microinfarcts. These lesions are not apparent using conventional neuroimaging and are therefore primarily detected through histopathological analysis. Notably, clinical and preclinical researchers are unsure of how cerebral microinfarction impacts the brain's vasculature and its effect on motor output. This thesis aims to characterize a mouse model of cerebral microinfarction to assess the impact of these microscopic lesions on blood-brain barrier (BBB) integrity and motor behaviour. For the first experiment, mice were unilaterally injected through the left common carotid artery with GFP microspheres (20 µm) and were sacrificed at different time points post-surgery (days 1, 3, 7, 14, and 21). All mice received an intravascular injection of Evans Blue dye (100 µl) through the tail vein thirty minutes prior to being transcardially perfused in order to evaluate BBB extravasation, a measurement of BBB disruption. To evaluate motor performance post-microinfarction, sham and microinfarct mice underwent a battery of behavioural tasks prior to and post-surgery. Cerebral microinfarction resulted in acute BBB disruption, where albumin leakage was most prominent one day following surgery. With our microinfarct mouse model, a Python script was developed to semi-automatically detect and register the microspheres to specific brain regions using the Allen Mouse Brain Atlas (version 3). Additionally, using several gross and fine motor behavioural tasks, analyses performed across both experimental groups revealed no significant motor impairments. Having a better insight into how these microscopic lesions affect brain structure and function in preclinical models would increase our understanding of how cerebral microinfarction impacts the human brain.

TABLE OF CONTENTS

LIST OF FIGURES

LIST OF TABLES

LIST OF SUPPLEMENTAL FIGURES

LIST OF ABBREVIATIONS

BBB	Blood-brain barrier
AD	Alzheimer's disease
VCID	Vascular cognitive impairment and dementia
CAA	Cerebral amyloid angiopathy
BCAS	Bilateral carotid-artery stenosis
ICA	Internal carotid artery
CCA	Common carotid artery
NVU	Neurovascular unit
MRI	Magnetic resonance imaging
MCAO	Middle cerebral artery occlusion
Mfsda2a gene	Major facilitator super family domain containing 2a gene
IVM injections	Intravascular microsphere injections
EB dye	Evans Blue dye
SPRT	Single pellet reaching task
NDS	Neurological deficit score
ECA	External carotid artery
GFP	Green fluorescent protein
FJ stain	Fluoro-Jade C stain
PBS	Phosphate-buffered saline
ROI	Region of interest
ANTs	Advanced normalization tools

SEM	Standard error of the mean
ANOVA	Analysis of variance
CT imaging	Computed tomographic imaging
DWI	Diffusion weighted imaging
OA647	Alexa 647-conjugated ovalbumin
GMS	Global motor score
PD	Pairwise discrimination
ITI period	Inter-trial interval period
LDI	Laser Doppler Imaging
MEP	Motor evoked potentials

ACKNOWLEDGEMENTS

First and foremost, I would like to express my sincere gratitude to Dr. Greg Silasi for allowing me the opportunity to complete my M.Sc. in Neuroscience in his laboratory. Despite the stress and workload of starting up his new lab, Dr. Greg Silasi always made time to provide useful insight into my project and steered me in the right direction whenever he thought I needed it.

I would also like to thank my co-supervisor Dr. Dale Corbett. Thank you for taking the time to provide advice and support and throughout these past two years. After having so many students under his wing, including myself, I will be grateful for his guidance and leadership.

Additionally, I would like to thank all current and past members within the Silasi lab: Sarah Zhang, Zanna Vanterpool, Gilles Salameh, Matthew McDonald, Matthew Jeffers and Frank Wu. Whether it was those morning coffee runs, conversations or one-on-one talks, every moment helped me get through these past two years. Thank you to all who provided me with advice, assistance and guidance with my writing, analyses and scientific skills.

I would also like to thank my Master's degree Thesis Advisory Committee members Dr. Diane Lagace and Dr. Paul Albert for taking the time to provide me with feedback throughout these past two years.

Last but not least, I would like to sincerely thank my family and friends for their support, motivation and encouragement throughout my academic career. Thank you for always being there for me whenever I needed someone to talk to and for cheering me up when needed.

STATEMENT OF CONTRIBUTIONS

Melissa Filadelfi completed all brain tissue sectioning for Experiment 1 using the Blockface imaging.

Melissa Filadelfi completed all tail vein injections of Evans Blue dye prior to the mice being sacrificed and Fluor Jade staining.

Dr. Greg Silasi performed completed all surgeries for both Experiment 1 and 2.

Melissa Filadelfi, Matthew Jeffers and Matthew McDonald were the three independent raters that were blinded to images and were asked to "manual threshold" each image to what they deemed was EB signal (see Figures 4 & 13, pages 18 & 35).

Matthew McDonald trained Ilastik to detect Evans Blue signal from background signal and batch processed the remaining 78 test set using the training set of images (see Figures 4 & 13, pages 18 & 35).

Melissa Filadelfi imaged (EVOS FLAuto2 microscope) and analyzed the total number of intravascular microspheres (IVMs) and Evans Blue dye in the lesioned hemisphere using a customized Image J script and Ilastik created and trained by **Matthew McDonald** (see Figure 12 & 14, pages 33 & 37).

Matthew McDonald imaged the second set of brains from Experiment 1 (10 brains) using the Apotome microscope.

Frank Wu, Matthew Jeffers and Matthew McDonald all collaborated in creating a Python script using the Allen Mouse Brain Common Coordinate Framework (version 3) to semi-automatically detect IVMs throughout the brain and within specific brain regions (see Figure 5, page 21).

Matthew McDonald compared the difference between manual and automated IVM detection using the Python script (see Figure 15, page 39).

Melissa Filadelfi compared and correlated the manually labelled IVMs in blockface images to manually labelled IVMs in histological sections to determine whether IVMs were falling out of the tissue during sectioning (see Figure 16, page 40).

Melissa Filadelfi completed all behavioural testing and analysis (see Figure 17-21, pages 44-48; APPENDIX B Supplemental Figure 22-25, pages 71-75).

Melissa Filadelfi completed the cognitive testing using the Bussey-Saksida mouse touchscreen chamber and analysis **(**see APPENDIX C Figure 26-27, pages 76-78).

Melissa Filadelfi completed the pilot study where motor mapping and laser Doppler imaging was performed on the microinfarct mice at baseline and at different time points post-microinfarct surgery (see APPENDIX D Figure 28-29, pages 79-80).

INTRODUCTION

1.1 Cerebral Microinfarcts

Microinfarcts are small microscopic lesions that are 10 times [1] more prevalent than symptomatic stroke. Due to the difficulty in detecting these small lesions using conventional neuroimaging [2-3], microinfarcts are vastly understudied relative to their prevalence. Cerebral microinfarcts are a common feature amongst the aging population, in which they are important biomarkers of many brain pathologies. These microscopic lesions are also a common finding in patients following symptomatic stroke [4-6], where microinfarct load is associated with a two-fold increased risk of a subsequent focal stroke [7-8]. Cortical cerebral microinfarcts have also been found in Alzheimer's disease patients [9, 10-13] contributing to both white matter loss and aggravation of brain degeneration. In addition to stroke and Alzheimer's disease (AD), cerebral microinfarction are commonly observed in other brain pathologies including vascular cognitive impairment and dementia (VCID) [2, 14-15], cerebral amyloid angiopathy (CAA) [3, 14, 16-20] and arteriosclerosis [21-23]. The incidence of microinfarction has been reported in patients with vascular dementia (62%), AD (43%) and in individuals who are ≥75 years old who have not been diagnosed with dementia (24%) [2, 4, 9]. Surprisingly, preclinical models of microinfarction are lacking, making it especially difficult to discern the impact of microinfarction on cognition, motor function, and how critical these lesions may be towards disruption of brain networks and its vasculature.

1.2 What Do We Know About Cerebral Microinfarcts?

Microinfarcts are presumed to be of ischemic origin [4], defined as foci of cellular death or tissue rarefaction[1] that are 0.05 to 3 millimetres in diameter [14-15]. Compared to focal ischemic strokes, individuals may acquire hundreds or even thousands of these microscopic lesions throughout their lifetime [3, 24]. Microinfarcts create a widespread form of damage [13, 25] that can extend beyond the areas of tissue rarefaction [4] and affect 2% of brain volume [14]. Cerebral microinfarcts are a known consequence of cerebral small vessel disease [4, 9, 26-27] (e.g. cerebral amyloid angiopathy), microemboli [4-5, 23], and hypoperfusion [4, 10], where each case results in the blockage of either penetrating or perforating arteries. The most common features of cerebral microinfarcts is the presence of tissue pallor and the dense microvascular meshwork that contains string vessels [2, 28].

The presence of the string vessels within the infarct zone acts as a marker of disturbances within the circulation in and around the microinfarcts [28]. Therefore, advanced neuroimaging that can detect changes in cerebral perfusion may play an important role in localizing cortical microinfarcts at earlier time points. In addition to coinciding with other pathologies, these small lesions are present in approximately 30% of otherwise healthy individuals [9] over the age of 65 years. More recently, the incidence of these miniscule lesions has been established to be increased after cardiac surgeries [29], and mechanical thrombectomy [30-31]. For example, the number of new microinfarcts can be increased 7.6-fold after cardiac surgery [29] and new microinfarcts were also found to develop in one-fifth of patients who underwent mechanical thrombectomy[30].

Compared to healthy individuals, the incidence of microinfarction is nearly doubled in the elderly that suffer from cognitive decline or dementia [13, 32-33]. In fact, the presence of microinfarcts can increase the risk of acquiring dementia and cognitive deficits two-fold [5-6, 34]. Cerebral microinfarcts do not appear to affect all cognitive systems equally, having the strongest impact on perceptual speed [34] and the weakest association with semantic and episodic memory [15, 34]; a hallmark of AD. In addition to a decline in processing speed, microinfarcts can reduce an individual's capacity to recover cognitive function after an acute ischemic stroke, increasing the cognitive vulnerability that is typically seen within the acute phase of a stroke [6]. In contrast to other pathologies (i.e. AD, cerebral amyloid angiopathy, arteriosclerosis, VCID), the relationship between cerebral microinfarction and dementia in aged populations is not well-understood. It is not clear whether microinfarction directly affects certain cognitive systems or indirectly exacerbates other vascular pathologies associated with cognition [15]. An example of this is seen where in addition to being associated with microinfarction, white matter demyelination/hyperintensities and microbleeds lead to diffuse changes throughout the brain including disruption of cognitive networks [35].

While a relationship between microinfarction and cognitive decline exists, less is known about their impact on motor function. This is especially important because with advanced age, a decline in sensorimotor control and function occur over time [36-39], where the decline in fine motor control, balance, and gait affect the ability of older individuals to perform daily activities of independence and living. A significant limitation to studying the impact of microinfarction on cognitive/motor performance in humans is that the onset and location of microinfarcts are

unpredictable and individuals are often unaware of their existence. Making investigation more difficult, microinfarction is often not discovered until a post-mortem autopsy is performed [24, 40]. Since post-mortem quantification of microinfarcts is only accomplished in a small portion of the human brain, the total number of microinfarcts that are reported during histological examinations significantly underestimates the total burden of infarction [40]. In addition, it is difficult for clinical studies to isolate the negative consequences of microinfarction from other comorbid pathologies. Using animal models to re-create the widespread distribution of microinfarcts provides us with a method to shed light on this problem; however, few models actually re-create the clinically observed brain-wide distribution of microinfarcts.

1.3 Animal Models of Microinfarction

1.3.1 Importance of Animal Models

Animal modelling of microinfarction has the potential to significantly contribute to our understanding of the impact of microinfarction on the brain. Through different experimental techniques microinfarct size, location, and load can be manipulated along with parallel testing of cognitive and motor function. In addition, it is much more realistic to quantify the total burden of microinfarction through histological analysis. In humans it is not possible to determine when microinfarction occurred, making it impossible to investigate their acute impact, leaving only the potential to assess the delayed and chronic impact of microinfarction. Since microinfarcts can be experimentally produced in animal models, both the acute and chronic impact of cerebral microinfarction can be assessed. To date, several different rodent models have been used to recapitulate microinfarction in a controlled environment.

1.3.2 Laser-Induced Occlusion of Single Penetrating Arterioles

By coupling laser irradiation with *in vivo* two-photon imaging, single-penetrating arterioles can be selectively occluded with photothrombosis [41-42]. To include an arterial, a photosensitive dye (Rose Bengal) is introduced into the circulation of a rodent and when the vessel is irradiated with green excitation light, the coagulation process is initiated, resulting in a localized-ischemic lesion [43]. These types of occlusions are generated near the pial surface, creating wedged or column-shaped cortical infarcts [44]. Laser-induced occlusion models are used to create reproducible cortical photothrombosis in rats and mice, where the surgical procedure is minimally invasive

and mortality rate is low [45]. This type of model allows for exquisite control over the location of the ischemic lesion, allowing for the size of the cortical lesions to be controlled by adjusting the plasma concentration of the Rose Bengal and the intensity and duration of the green laser [45]. Limitations of this model are that the lesions are restricted to the cortex and there is an end-arterial occlusive nature, making the lesions resistant to blood flow following surgery. Notably, this type of microinfarct model only produces an infarct in one area of the brain (dependent on the location of the laser); however, in humans these lesions occur throughout the entire brain. Therefore, the laser-induced occlusion model does not accurately mimic the widespread distribution of microinfarcts.

1.3.3 Bilateral-Carotid Artery Stenosis (BCAS)

Bilateral carotid-artery stenosis (BCAS) uses microcoils to induce chronic cerebral microinfarcts. Although mainly a model of VCI, after long periods (6 months) [46] of BCAS, mice develop subcortical microinfarcts. Advantages of using this model are that the mortality rate is normally less than 2%, and the severity of cerebral hypoperfusion can be controlled through the regulation of the internal diameters of the microcoils [47].The disadvantages of using BCAS models include a lack of motor dysfunction since it primarily impacts the hippocampus[47], an abrupt decrease in cerebral blood flow that occurs with the placement of the coil, and the duration of time before microinfarcts develop.

1.3.4 Intra-Carotid Injection of Microemboli

The injection of microemboli into the circulatory system of the brain is another method that has been used to create a widespread distribution of microinfarcts. To date, two types of microemboli have been injected through the internal carotid artery (ICA) to produce microocclusions: cholesterol crystals [13, 48] and fluorescent microspheres [49]. These microemboli have been shown to produce a wide-spread form of damage throughout the brain where the incidence of microinfarction has been quantified in several brain regions (i.e. the cortex, hippocampus and thalamus) [48-49]. The type of infarcts that are seen in the cortex and pial surfaces include wedged and column-shaped lesions while smaller microinfarcts occur in deeper cortical layers [40]. To obtain a reliable microinfarct model using microemboli, the size and number of emboli injected are important factors to consider. A limitation of using cholesterol crystals [13, 48] to produce

microinfarction is that different immunofluorescent antibodies (i.e. GFAP, CD68, CD11b, and NeuN) are required to localize the microinfarcts throughout the rodent brain, whereas the location of the fluorescent microspheres [49] is easily detected using a fluorescent microscope. While cholesterol crystals are variable in size (40 to 100 µm in diameter) and cannot be quantified easily in brain sections, fluorescent microspheres of a discrete size (20 to 50 µm in dimeter) and can mimic the shower of lesions that are apparent in the human brain [50]. This in turn allows for easy post-mortem localization of lodged microspheres within brain vasculature. Models such as the laser-induced microlesions and intra-carotid injection of microemboli allow researchers to determine the effect of microinfarcts on brain structure and connectivity, independent from other brain pathologies [40]. However, with intra-carotid injection models, researchers have less control over lesion location and occluded vessels are permanently blocked, mimicking microinfarct cases without reperfusion [45].

1.4 Brain Microvascular Network and Cellular Death

1.4.1 The Blood-Brain Barrier

The neurovascular unit (NVU) is formed from a complex structural and functional multicellular relationship between the brain and vasculature. The cellular components which make up the NVU are the neurons, perivascular astrocytes, microglia, pericytes, endothelial cells, and the basement membrane [51], all of which collectively protect the brain's ionic balance and refute the passage of neurochemicals from the rest of the body [52-54]. In addition to controlling the cerebral blood flow [55], the NVU plays several roles throughout the brain; however, the two main responsibilities are the maintenance cerebral homeostasis and conservation of the BBB [51]. The NVU links neurons to the cerebral vessels through neurovascular coupling, where the blood supply is matched to the demand of neurons via changes in the intraluminal diameter of the vessels [51, 56]. The cellular components from the NVU also play a fundamental role in the development and maintenance of the BBB. An example of which are the endothelial cells that provide paracellular permeability through the BBB via endothelial tight junctions, and contribute towards the BBB homeostatic function by metabolizing enzymes [51, 57]. While the NVU is responsible for a large portion of the central nervous system, the BBB is more confined to isolating the central nervous system from the systematic circulation [52] to protect the central nervous system from toxins, pathogens, injury and inflammation [58-59]. The blood vessels within

the central nervous system are formed from two distinct cell types: endothelial cells, which form the walls of the vessels, and mural cells that sit above the endothelial layer [59]. The endothelial cells of the central nervous system are held together by tight junctions that lead to firm regulation for the movement of ions, molecules and cells between the blood and the brain [58]. Although the endothelial cells are the important contributing cells to the BBB, properties and the functions of the BBB are controlled through the interactions between murals cells, immune cells, glial and neural cells.

Patients suffering from an acute ischemic stroke undergo magnetic resonance imaging (MRI) within the first hours after the onset of the stroke, at which point the disruption of the BBB can be identified. To date, most information about BBB disruption in humans mainly comes from larger focal stroke. For instance, the permeability of the BBB has been linked to post-stroke edema [54], where the first phase begins with the regulation of endothelial transcytosis during the early period of reperfusion (6 hours following stroke). In comparison to the first phase, the second phase reveals major remodeling of the tight junction complexes between 24-48 hours following stroke [60]. After the onset of an acute ischemic stroke, the BBB is promptly disrupted, resulting in its integrity being diminished during the acute and early subacute phases of stroke. During the acute phase, infiltration and accumulation of peripheral immune cells into the parenchyma contributes to the progression of the injury [61], at which point prolonged disruption to the BBB is associated with stroke severity [54, 62]. Even though the filtering capacity of capillaries are robust, disease or injury (e.g. stroke) to the brain results in the rupture and acute permeability of the BBB, allowing pathogens to infiltrate [53]. A series of protein transformations and degradations occur during BBB disruption. These changes include tight junction degradation and redistribution, modifications in astrocytic end feet and pericyte coverage, whereby the cytoskeleton of the endothelial cells undergo further transformation [58, 63]. The tight junctions and the adhesion properties of the cerebral capillaries are what maintain the BBB integrity [58]. During the acute phase of the BBB permeability, the configuration of the tight junctions are normal, however between 48-58 hours after stroke, these protein complexes become degraded, leading to a second peak of BBB permeability [54, 58]. This second peak of permeability leads to uncontrolled entry of blood and molecules into the brain parenchyma, spreading further damage throughout the brain.

Since it is challenging to study BBB disruption in humans, preclinical models are needed to grasp a better understanding of when these disruptions occur throughout the brain. To date, a vast majority of preclinical stroke models have assessed BBB disturbance using focal ischemic stroke models. Preclinical middle cerebral artery occlusion (MCAO) models of stroke have revealed that at 4 and 24 hours after stroke, there's an increase in ischemic BBB breakdown [60, 64-65]. In contrast to larger ischemic strokes, an intra-carotid injection of microemboli stroke model injected cholesterol crystals (60 to 100 μm in size) to create a widespread form of damage throughout the brain to investigate the disruption of the BBB [48]. It was discovered that the perivascular albumin staining was evident at 4 days post-occlusion; however, the histological marker did not persist beyond 1 week [48]. Another study evoked cortical spreading depolarizations over the right hemispheres of mice where BBB disruption was assessed using Evans blue or dextran between 3-4 hours post depolarizations [66]. It was found that cortical spreading depolarizations induced the opening of the BBB to water and larger molecules between 3-6 hours and lasting 24 after, all of which was mediated by endothelial transcytosis [66]. While the general analysis of BBB disruption is beneficial to determine time periods of extravasation, molecular mechanisms that control the BBB formation is critical. A study demonstrated spatiotemporal development profiles of BBB functionality in embryonic mice, whereby they discovered that the major facilitator super family domain containing 2a (Mfsda) gene is expressed in the BBB [67]. Genetic ablation of the Mfsda2a gene resulted in BBB extravasation from embryonic period to adulthood [67]. Following the ablations, electron microscopy showed an increase in endothelial cell vesicular transcytosis in Mfsda2a knockout mice [67]. Overall, their keys findings suggest that Mfsda2a is an important gene that helps in the regulation of the BBB function by overcoming transcytosis in the endothelial cells [67].

In contrast to focal strokes, not much is known about the impact microinfarction has on the BBB in humans since these microscopic lesions are normally discovered during post-mortem histological analyses. Therefore, the acute stages of BBB disruption after microinfarction cannot be studied without preclinical models.

1.4.2 Cellular Death and Neuronal Injury

Together, the central nervous system and the immune system are strongly interconnected and communicate with one another through different networks [68]. Microglia are the innate immune cells that dwell throughout the brain parenchyma [69] responding first during an immune defence throughout the central nervous system. Macrophages and other immune cells (i.e. dendritic cells and lymphocytes) surround the blood vessels, choroid plexus and leptomeninges (combination of arachnoid and pia matter) monitoring immune functions that occur throughout the brain [69]. These monocytes will engulf and digest cellular debris and foreign substances, cleaning up the central nervous system. After brain ischemia, reactive microglia and macrophages infiltrate the site of damage, peaking around four days post-injury in both rats and mice.

Acute cerebral microinfarcts are defined as being either incomplete or cavitated, with evidence of cell injury or death and the infiltration of immune cells [2]. Throughout the cortex post-microinfarction, cellular death occurs along with delayed demyelination, microglial activation and neuronal damage [13]. The microinfarct core contains BBB leakage and an increased amount of oxidative protein damage within cells, vasculature, and astrocytes, while degenerating cells are located around the border of the infarct [13, 41]. Furthermore, microinfarction results in the formation of a cellular migratory path of microglia and macrophages along the stroke border and subcortical white matter tracts that can extend into the contralateral hemisphere [41, 70].

1.5 Histopathological Analysis of Microinfarction in Humans and Animal Models

Through clinical histological examination, acute cerebral microinfarcts have been defined as foci of cellular injury without the presence of cavitation or cell death[4]. In contrast, chronic cerebral microinfarcts are described as being focal cavitated tissue with the presence of gliosis and several remaining macrophages [2, 4] that can occur in the superficial, middle and deep layers of the cortex [28]. Smaller lesions may contain only neuronal cell loss with or without the presence of macrophages or gliosis with folding of the surrounding tissue [4]. At the chronic phase of microinfarction, activated macrophages tend to remain within the core of the infarct where they can uptake extracellular granules, which are a result from neuronal cell death, and iron deposits that remain due to neuroinflammation [28]. Histological findings that are common in all chronic microinfarcts include tissue pallor, loss of neurons and the accumulation of lipofuscin pigments (granules) that are surrounded by a dense microvasculature network within the infarct core [28].

Microinfarcts have also been shown to vary in regard to their shape, size and the amount of iron accumulation in the microinfarct core which influences their detection using clinical neuroimaging [28]. Using haematoxylin and eosin staining [25], cortical red hypoxic neurons are evident surrounding the infarct core [4]. Although many researchers use haematoxylin and eosin-staining to readily identify acute and subacute cerebral microinfarcts, immunohistochemical staining has also been used as a marker of tissue injury. Examples include the marker CD68 for macrophages, human leukocyte antigen to label activated microglia [9, 12], and glial fibrillary acidic protein for gliosis [2, 4]. While the sensitivity and specificity for different histological markers remains unclear, these approaches make the microinfarcts stand out and easier to quantify [25].

Cerebral microinfarction induced in animal models results in a similar injury profile to humans. The main difference that is found between humans and rodents is the angioarchitecture. The rodent cortex contains more penetrating venules compared to penetrating arterioles, the inverse of what is seen in the human cortex [71]. When assessing cerebral microinfarcts in both humans and rodents, the size, shape and location of these lesions tend to show notable similarities. These similarities are thought to occur due to a proportional cortical vascular scale between the two species [14, 71]. While brain size may differ between species, the penetrating arterioles range in diameter between 15-30 μm [72] and 15-40 μm [73] across the cortex in both rodent and human brains respectively.

1.6 Animal Models of Cerebral Microinfarction Induced Cognitive and Motor Deficits

Recently, a clinical study reported patients who had cerebral microinfarction show subtle motor deficits. In humans, cerebral microinfarcts have an impact on brain structure as well as cognitive [5-6, 15, 34] and motor function [36]. Similarly, rodent models using either unilateral or repeated bilateral injections of cholesterol crystals to induce microinfarction have revealed deficits in cognition and motor learning tasks. Several cognitive tasks have been used in animal models with hippocampal [50] and striatal injuries [10, 13] to reveal impairments in spatial memory acquisition and retention [48]. While the relationship between microinfarction and cognitive function has been investigated in several studies [13, 41, 48], less is known about the impact of microinfarcts on motor function. For example, following intra-carotid injection of cholesterol crystals (60 to 100 μm in diameter) to induce microinfarction in rats, it has been demonstrated that motor learning on the Rota-Rod task was impaired [48]. In contrast to the Rota-Rod task, intra-

carotid injection of cholesterol crystals in rats (60 to 100 µm) or in mice (40 to 70 µm) resulted in no significant difference in locomotor activity between sham-operated animals and embolized animals [13, 48]. Notably, intra-carotid injections of fluorescent microspheres in mice resulted in a significantly higher neurological deficit score (NDS) over four weeks compared to sham mice [50]. Additionally, using the clasping reflex test to analyze limb dystonia, is was concluded that post-surgery, the microinfarct mice had a higher clasping score, where sham mice did not go above zero when compared to baseline performance [50].

Although several motor tasks have revealed significant differences between microinfarct animals and sham-operated controls, many of these impairments are subtle. For my thesis, a more comprehensive behavioural assessment was warranted to evaluate basic neurological deficits, balance, hindlimb/forelimb function, sensorimotor deficits, spontaneous forelimb and skilled forepaw use. While both the rotarod and NDS have poor sensitivity to detect small deficits, and the open field test measures general motor deficits, the tasks that I have chosen are more sensitive for detecting minor deficits [74].

1.7 Rationale

Cerebral microinfarction is difficult to study in humans. These microscopic lesions go undetected using clinical neuroimaging and are primarily detected once the person has passed away. Furthermore, few preclinical studies model the widespread injury that has been observed throughout the human brain. Using intra-carotid injections of fluorescent microspheres to create the microscopic lesions has numerous benefits compared to other models of microinfarction. We are able to create a widespread injury throughout the brain, where we can easily detect each fluorescent microsphere and their location throughout the brain vasculature. Our cerebral microinfarct mouse model allowed us to mimic the diverse distribution of infarcts that is normally seen within the general population by targeting the arterioles of the brain.

While BBB breakdown has been assessed following larger focal strokes, the time course of its integrity has not yet been investigated in cerebral microinfarction. While it is difficult to longitudinally study the impact of microinfarction in humans, experimentally inducing microinfarction permits the investigation of the time course of BBB disruption across time. The first study of this thesis addresses whether intravascular microsphere (IVM) injections disrupts

the BBB and characterizes how long the disruption persists. It was hypothesized that IVM injections would result in acute disruption of the BBB where Evans Blue (EB) dye would be most evident within the parenchyma during the first week post-surgery.

Due to small sampling of the human brain, the total damage that occurs from microinfarction is a plausible estimation based on smaller sections that have been analyzed. A limitation to studying microinfarcts in humans is that one cannot obtain a precise number of how many infarcts occur throughout the entire brain and in which specific brain regions these lesions are located. Therefore, using our model, quantification of the total number of IVMs throughout the brain was to be completed to determine whether this model of microinfarction would produce a widespread distribution of IVMs throughout the brain, being variable amongst animals. Thus we analyzed the distribution of IVMs across several experimental days post-IVM surgery and performed whole-brain localization of IVMs in a subset of mice to validate a semi-automated Python script to automatically localize IVMs throughout the mouse brain. This script will be used to determine how IVM load in specific brain regions (e.g. motor cortex) impacts motor function.

Furthermore, while most preclinical studies have focused their attention on evaluating the impact of microinfarction on cognition, the second experiment of this thesis evaluates the impact of microinfarcts on motor function. The evaluation of motor impairment in a clinical setting is problematic for researchers to conduct due to the difficulty in controlling other pathologies that may coincide with microinfarcts. I hypothesized that mice with induced microinfarction would result in subtle motor impairments acutely after surgery.

MATERIALS & METHODS

Experiment 1

2.1 Animals & General Procedures

All experimental procedures were conducted in accordance with the guidelines of the Canadian Council on Animal Care and approved by the Animal Care Committee at the University of Ottawa. All mice were housed in a 12-hour light/12-hour dark cycle and were provided with food and water *ad libitum*.

To investigate whether intravascular microsphere (IVM) injections result in BBB disruption, we conducted a time course experiment to determine if, and when, BBB integrity was compromised (Figure 1). In the first set of experiments, a total of 38 mice (see APPENDIX A Table 1) were distributed into five experimental groups that were sacrificed at different time points post-microinfarction (Day 1 n=10, Day 3 n=12, Day 7 n=6, Day 14 n=4, and Day 21 n=6).

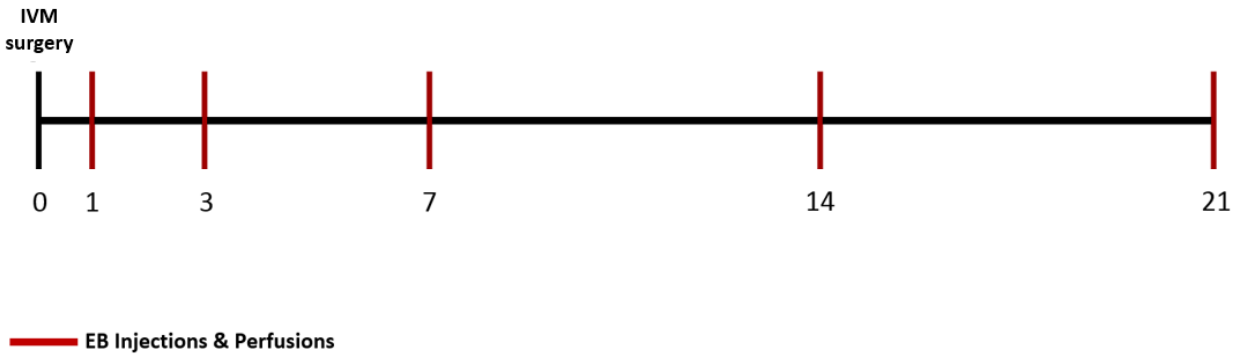

Figure 1. Experimental timeline for the time course of BBB disruption. Mice were sacrificed days 1, 3, 7, 14, and 21 post-surgery where they received EB dye injections prior to being perfused (n= 38).

2.2 Experimental Surgery

2.2.1 Preparation of Microsphere Solution

To perform the IVM surgeries, a microsphere stock solution was purchased (FluoroSpheres polystyrene, Polysciences, Cat# 19096-2; 20µm particles packaged as 2.5% aqueous suspension; 5.68 x 10^6 particles/ml). The microsphere size was selected based on the approximate size of the arterioles within mice, ranging between 10 to 20 µm in diameter. The microsphere working solution was prepared the morning of the surgeries. The microsphere stock solution was mixed in a vortex mixer for approximately 1 minute before and after being placed inside a sonicator (ultrasonic bath 1.9L) for 5 minutes to agitate the liquid in order to prevent the microspheres from adhering to one another. Next, 4.0 µl was extracted from the stock solution and added to 2 ml of saline, giving a final concentration of 1.14 x 10^4 particles/ml of saline for our working solution. Each mouse that received the microinfarct surgery was injected with 100 µl of the working solution (1138 microspheres/injection). Immediately prior to each surgical injection, the working solution was mixed (~ 20 seconds) using a vortex to ensure that the microspheres were separated from one another. If a yellow-green film was visible at the top of the solution, the microspheres were not separated properly and the solution would be mixed again until the yellow-green film disappeared. Prior to surgeries, two samples (100 µl each) were extracted from the working solution, imaged using the EVOS FLAuto2 microscope (GFP 510nm) and analyzed in Image J to determine the number of particles that were in each injection

2.2.2 Intravascular Microsphere Surgery

Mice were anesthetized with isoflurane (2% induction, 1.5% maintenance in air) until they were unresponsive to a foot pinch. A saline (1 ml) and Meloxicam injection (5mg/ml; undiluted) were given subcutaneously to the mice followed by a surgical preparation; neck area being shaved and sterilized with alcohol and the eyes being lubricated (1 drop/eye with Optixcare eye lube; 20g/0.70oz). For each surgery, all mice were surgically prepared followed by a small neck incision (~1 cm) to allow access to the common carotid artery (CCA). Once the vasculature was accessible, the external carotid artery (ECA) was temporarily clamped and the area was irrigated with saline. Using a syringe (31-gauge needle), we injected 100 µl from the working solution (~20 µm in size; 1138 microspheres/100µl) into the left CCA (Figure 2A), resulting in a widespread distribution of micro occlusions throughout the mouse brain (Figure 2B)[49]. After

removing the needle, surgifoam (absorbable gelatin sponge) was then placed onto the CCA to aid coagulation and the neck incision was closed. Following surgery mice were placed in an incubator chamber (35-37 °C) until they were awake and began to move. Subsequently, mice were returned to their home cage.

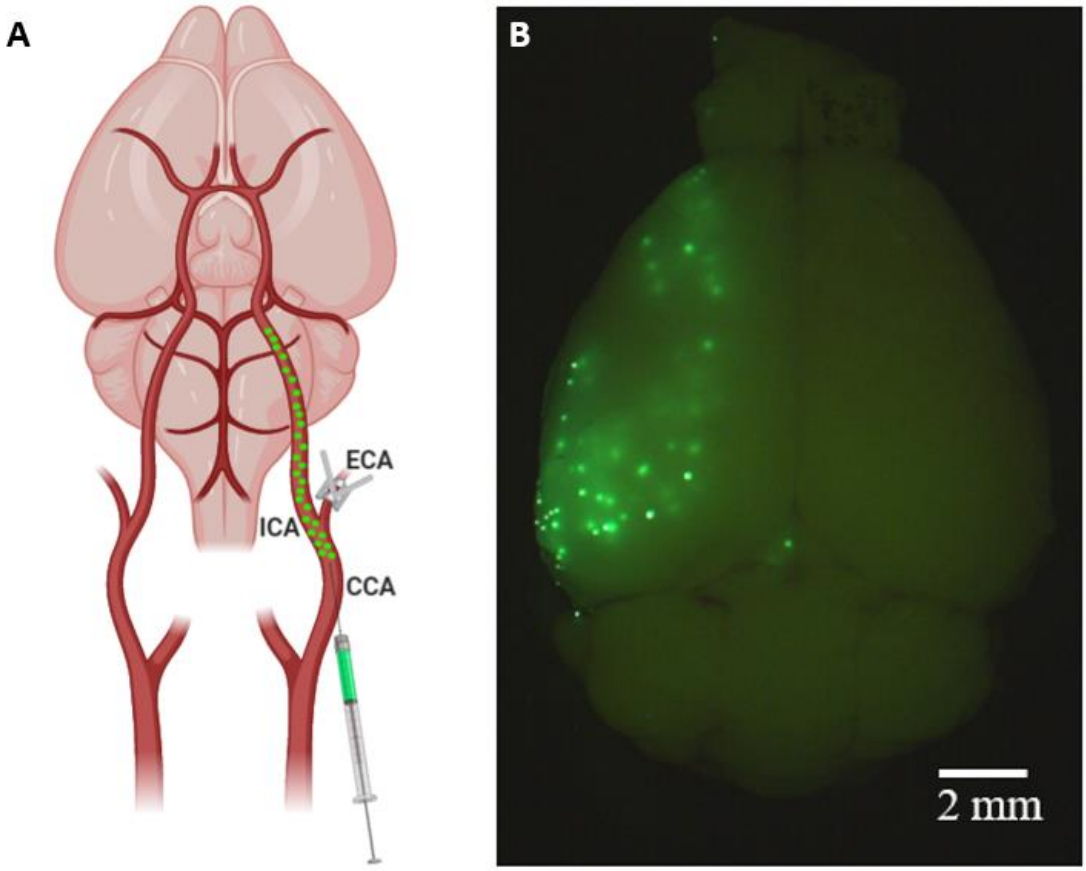

Figure 2. Microinfarct surgery. (A) A ventral view of the unilateral intravascular microsphere (IVM) injection [49]. (B) Dorsal view of GFP-labelled microspheres within the left hemisphere.

2.3 Intravascular Injections of Evans Blue (EB)

A mouse tail illuminator restrainer was used to confine an awake mouse in a tube in order to proceed with the tail vein injections. To clearly see the veins, the tails of the mice were swabbed with 70% ethanol and placed within a slit where light warmed the tail to expose the veins. To assess BBB permeability, mice were injected intravascularly with EB dye (2% solution in saline; MW= 960.81 g/mol; 100 µl/mouse) through the tail vein 30 minutes prior to perfusion. BD ultra-fine insulin needles with a 31 gauge were used for the tail vein injections.

2.4 Euthanization & Histology

2.4.1 Perfusion, Tissue Sectioning & Histology

Mice were anesthetized with sodium pentobarbital (working solution=65mg/mL; injection=1.6mg/25µl) and transcardially perfused with 10 mL of phosphate-buffered saline (PBS) followed by 50 mL of 10% neutral buffered formalin (flow rate for perfusions= 3-5 mL/min). Brains were carefully removed and post-fixed in formalin at 4°C for a minimum of 24 hours. Sections were cut at 50 µm using a modified vibratome to accommodate blockface imaging. Serial sections were collected along the anterior/posterior axis between -2000 to 3000 (0=anterior commissure) and mounted on 1% gelatin-coated slides. To assess the number of IVM in each section and EB dye extravasation in Experiment 1, slides were also stained with DAPI (4′,6-diamidino-2-phenylindole) and imaged at 4X magnification using an EVOS FLAuto2 microscope (GFP 510nm: IVM, Texas Red: EB 680nm).

2.4.2 Blockface Imaging

The long-term goal of using this IVM model of microinfarction is to automate the process of counting and localizing IVMs. Serial blockface imaging has been used to obtain 3D data from thick volumes of tissue, where one must image the sections prior to being cut; continually imaging the entire blockface [75]. With slide-mounted sections it is difficult to maintain the normal shape of the brain, reducing the potential to register IVMs to a mouse brain atlas. Therefore, we have begun to develop a blockface imaging technique (Figure 3A) using a Raspberry Pi camera and a blue light fixed to a vibratome in order to capture serial images of the tissue block to visualize the location of the IVMs (Figure 3B). In order to delineate the edges of the tissue in the blockface images, we immersed the tissue in a block of opaque (black) agarose. Prior to

immersing the brain in to the block, a drop of black India ink was mixed in with the agarose gel (0.1g of agarose/5 ml of dH_2O) so the entire blockface would become black in colour. The blockface was then glued to a vibratome, whereby each serial section of the tissue was captured using the Raspberry Pi camera prior to being sectioned. After cutting through the entire blockface, a stack of images was generated going from the anterior to the posterior sections that were cut. To localize IVM to specific brain regions, it is essential to visualize certain structures of biological tissue and create a three-dimensional (3D) reconstruction of the sample. By using serial blockface imaging, this removes the problem of having to deal with delicate tissue sections, which is quite often difficult and distorted using histological sections [76]. Brains from Experiment 1 (38 brains) have been imaged, sectioned and used for our EB quantification and analysis for IVM distribution.

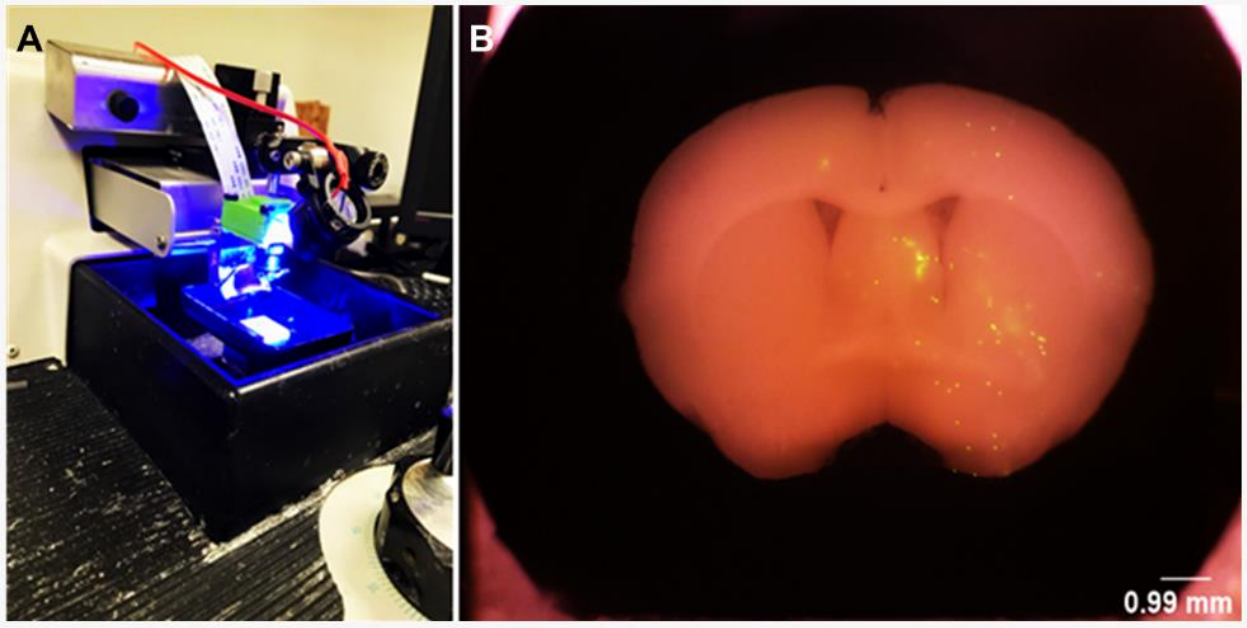

Figure 3. Serial Blockface imaging set-up. (A) Blockface imaging using the vibratome. (B) A serial section captured using the blockface imaging (green dots= microspheres).

2.4.3 Semi-Automatic Detection of EB Dye Using Ilastik

Quantification and analyses of EB signal was conducted using Ilastik, a deep neural net pixel classification software (ILASTIK version 1.3.2.) [77]. This software was used to semi-automatically detect the EB signal across all sections that were captured and imaged using the EVOS FLAuto2 microscope. This pipeline was used to determine the amount of EB extravasation that occurred in each brain at a given time point post-microinfarction. From the histological sections imaged using the EVOS FLAuto2 microscope, a total of 100 images with varying EB signal were selected. Three independent raters were blinded to images and were asked to "manually threshold" each image to what they deemed was EB signal (Figure 4A-C). This step was completed using a custom Image J script where all 100 images were placed in a random order followed by the raters manually thresholding each image (Image > Adjust > Threshold). Of the 100 images, each image was presented three times to each rater in order to assess intra-rater reliability (i.e. each image was assessed 9 independent times in total). Each pixel within an image was assessed for EB signal. If a pixel was deemed to have EB signal each time a rater manually thresholded the image and across the three independent raters (9 separate times), this was considered "True signal". Ilastik was then trained on 22 of these 100 manually scored images to detect the EB signal versus background signal (Figure 4C). To assess the capacity of Ilastik to detect EB signal, we compared the remaining 78 manually evaluated images to the same images when processed using this training algorithm.

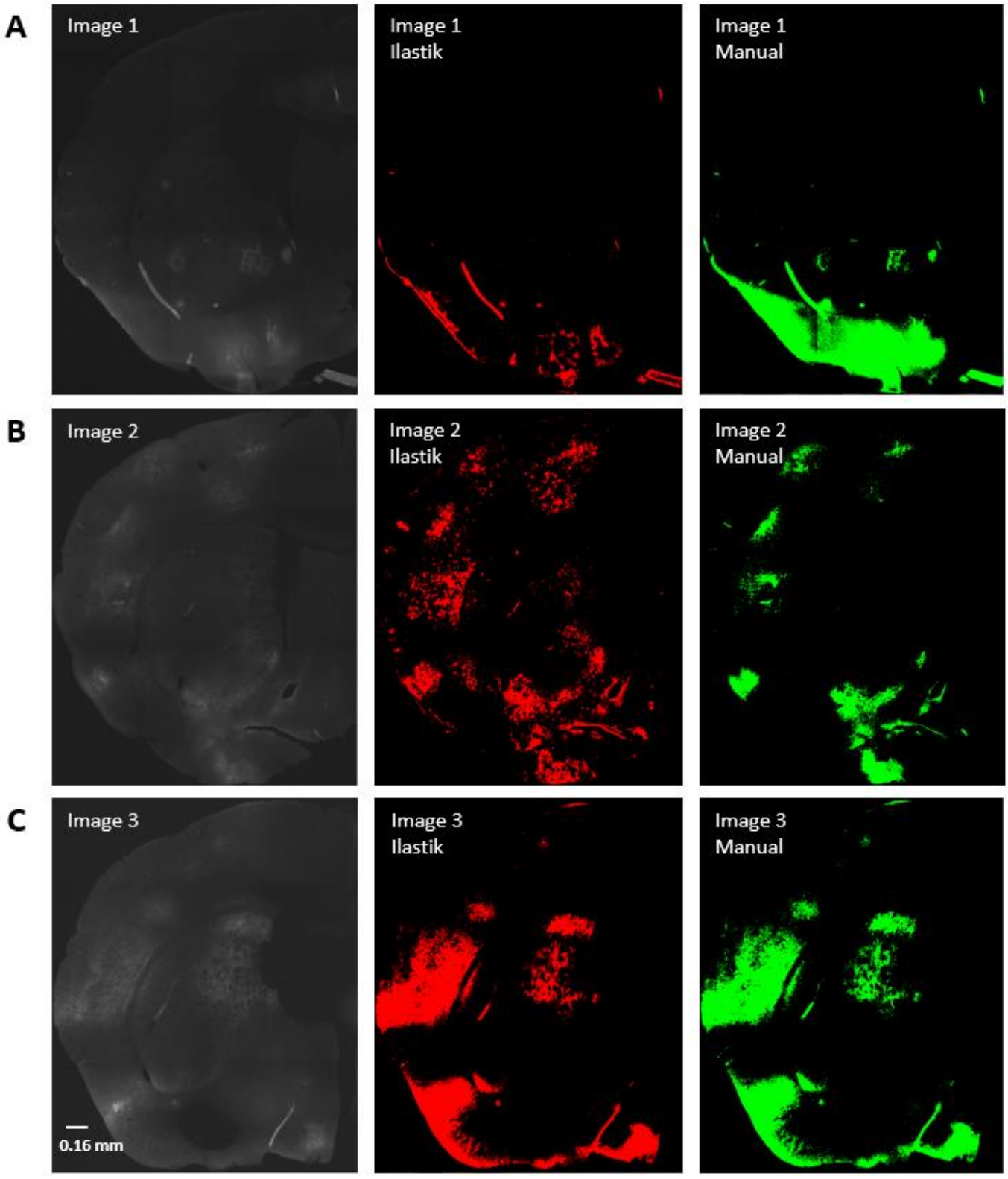
A
Image 1
Image 1
Ilastik
Image 1
Manual
B
Image 2
Image 2
Ilastik
Image 2
Manual
C
Image 3
Image 3
Ilastik
Image 3
Manual
0.16 mm

Figure 4. Ilastik EB Classification (EB signal=white). (A) Left panel: Image of EB where Ilastik underestimated EB signal the most compared to manual computation. Middle panel: Ilastik EB classification. Right panel: manual EB classification. (B) Left panel: Image of EB where Ilastik overestimated EB signal the most compared to humans. Middle panel: Ilastik EB classification. Right panel: manual EB classification. (C) Left panel: EB image that Ilastik was good at classifying. Middle panel: Ilastik EB classification. Right panel: Manual EB classification.

2.4.4 IVM and EB Dye Quantification

All brains were selected to quantify the number of IVMs in all sections using a customized Image J script, and a total of 35 brains were used assess the change in EB extravasation throughout the brains at each time point post-surgery. Three brains were excluded for the EB analysis due to unsuccessful intravascular injections of the dye. A region of interest (ROI) of each brain section was identified by thresholding the image to the DAPI signal. These ROIs were then divided into right and left hemispheres by manually drawing a line down the midline of the brain section. The anterior/posterior coordinates of each section were determined relative to the posterior portion of the anterior commissure. The number of IVMs were identified by thresholding to the GFP signal and running the analyze pixels function where particles greater than 10 μm were counted as IVMs. EB damage for all sections was determined based on the Ilastik segmentation maps produced by the aforementioned training dataset and the area of EB signal was calculated using ImageJ's analyze pixels function. Total volume of damage was determined by summing the area of EB signal throughout serial sections. In addition to analyzing the raw values for the total number of IVMs and EB volume, we normalized each value (both the number of IVMs and EB volume) to the area of the ipsilesional and contralesional hemispheres to create a common scale between mice across time without distorting the experimental errors across experimental days.

2.4.5 IVM Distribution and Localization

To further our goal to develop a workflow to automate the allocation of IVMs to given brain regions based on the Allen mouse brain atlas, a Python script was developed to manually align all serial blockface images of each section and to manually label the microspheres throughout the entire brain (to be used to ultimately validate our automated approach). This script was used in a subset of mice from Experiment 1 (n=8) to determine if manually counting the IVMs was

significantly different from the automated detection of the IVMs. Furthermore, the long-term goal will be to also apply this approach to Experiment 2 to perform whole-brain localization of IVMs in order to determine how IVM load in specific brain regions (i.e. motor cortex) impacts behaviour.

Manual Labelling of IVMs

Blockface images that were captured during sectioning were placed into a single stack of images per brain. While the images show both tissue and agarose, only the brain tissue was selected for segmentation. After thresholding all images to grayscale (Figure 5A), a bounding blue box was calculated around the center area of the tissue. The blue box is expanded by 75 pixels in both the width and height of the image (Figure 5B). Any pixels that were located outside of the blue box were identified as background signal, while the pixels located within the box were further used for segmentation (Figure 5C). All images were then manually aligned to the brain tissue that was centered within the image based on the user's selection of the anterior commissure (ac; the last section where the ac was seen crossing the midline). The brain section was then rotated after the user drew a vertical line down the images, separating the two hemispheres (Figure 5D left and right panels). Images were aligned by clicking a common feature between serial sections (i.e. IVMs; Figure 5E). IVMs were then either manually counted or automatically detected (Figure 5F) where the x, y, z coordinates for each IVM was written and saved as a csv file. This step was completed using both methods to validate the automated detection of the IVMs.

Automatic IVM Detection

Once the IVMs were detected based on thresholding to IVM signal and their x, y, z coordinates were saved, each IVM was clustered across serial sections and the true depth and location of the IVMs were identified (Figure 5G). Masks were further generated for the true location of each IVM. Each brain image was then transformed to the fixed Allen Brain Atlas (Mouse CCF, Reference Atlas, Version 3 2017) using advanced normalization tools (ANTs) [78]; an image registration and segmentation toolkit (Figure 5H left panel). This transformation of the Allen Brain Atlas to each image was then applied to the masks of the IVMs, allowing the Python script to detect the location of each IVM throughout specific brain regions (Figure 5H right panel).

Once all transformations and registrations were completed, an anatomical tree of brain regions was then produced for each brain (Figure 6).

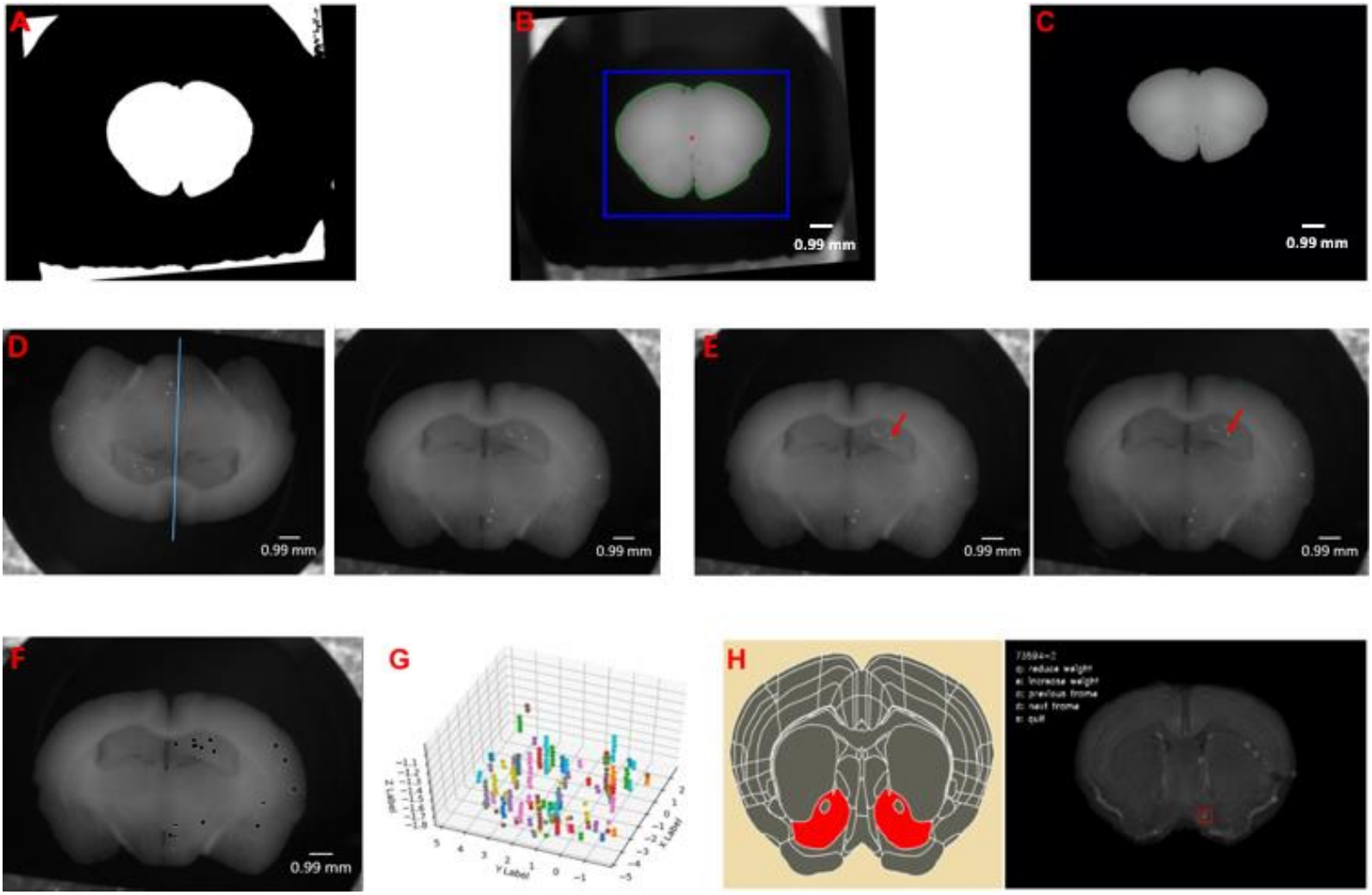

Figure 5. Manual and automated IVM detection. (A-C) To obtain a finalized image to use for segmentation, images are thresholded to grayscale and a bounding blue box is traced to crop out the pixels located exterior to the brain tissue (50 µm). (D) The images become centered by selecting the last section where the anterior commissure is seen midline. The brain is then rotated by drawing a line (blue line) between both hemispheres (left to right panel). (E) All images within the stack are then aligned based on common features (i.e. red arrows= IVMs; or brain structures if no IVM is present). Each individual IVM is represented as a white dot (F) IVMs were either manually counted or automatically detected using the Python script (black dots = manually labelled IVMs). (G) A sample of the location of several IVMs that were identified within 8 serial brain sections. IVMs are clustered across serial sections where the true depth/location of the IVMs are identified. (H) Each brain image is then transformed to the fixed Allen Brain Atlas (version 3) using ANTs (left panel; red brain area= nucleus accumbens). This transformation is then applied to the IVMs (right panel; red box= IVM in the nucleus accumbens), allowing the Python script to detect the location of each IVM throughout the brain.

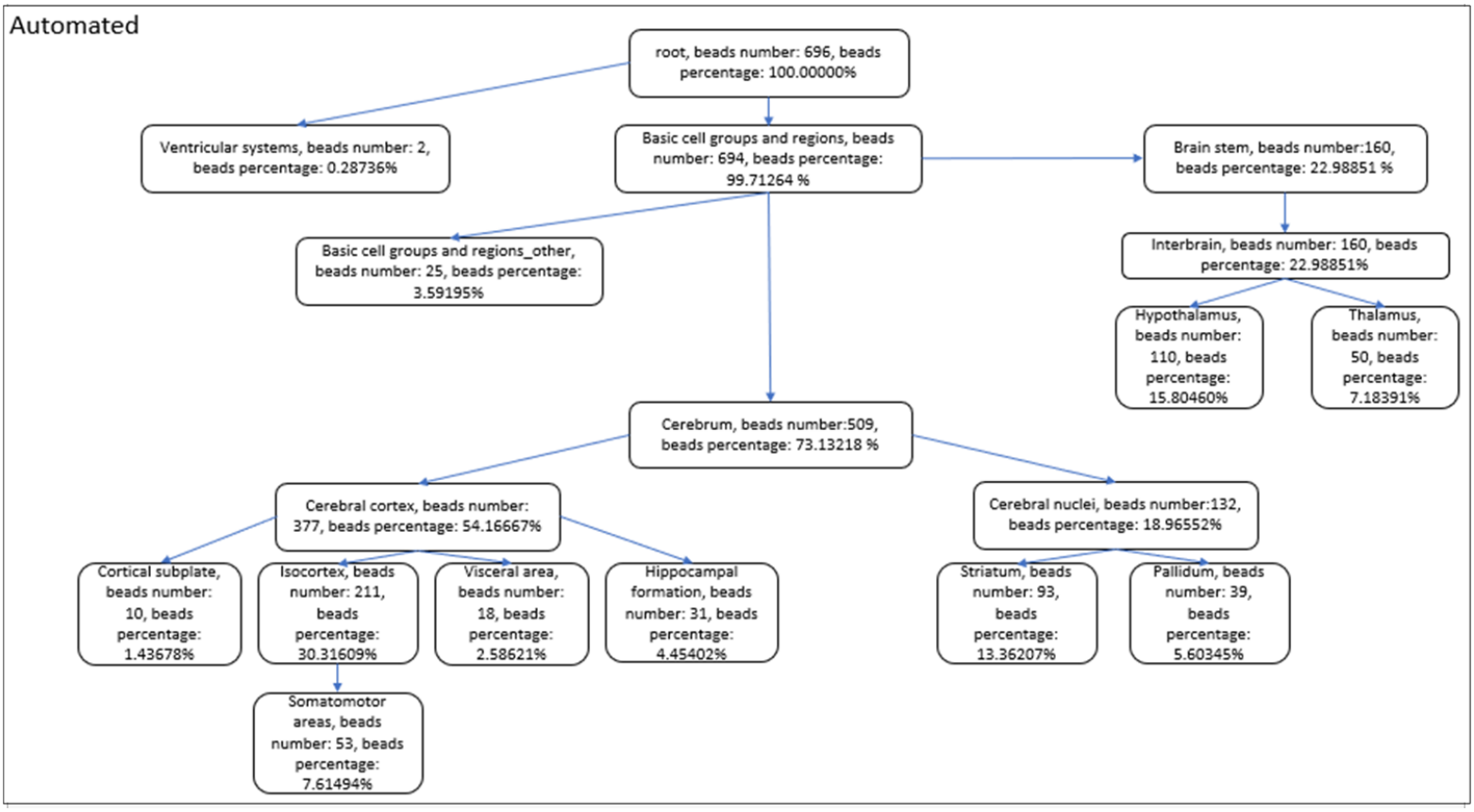

Figure 6. IVM localization output data. Output data from the transform matrix that is applied to the bead localization step in the automated microsphere script. The panel shows the automatic localization of the microspheres and their distribution within specific brain regions.

Experiment 2

In a second experiment, a battery of gross and fine motor behavioural tests were used to evaluate whether IVMs induced behavioural impairments in certain motor domains and if so, how the motor performance changed over time. A total of 35 mice (see APPENDIX A Table 1) were trained at baseline on the single pellet reaching task (SPRT; 7days/week for 3 weeks), the tapered beam task (3 trials in 1 day), adhesive removal task (5 days; performance of last 2 days were averaged), cylinder task (1 day) and NDS (1 day; 4 testing categories/mouse; Figure 7). Following the baseline training for SPRT, two mice were excluded from the experiment because they did not learn how to reach for the pellets during the second phase of the task (see Materials and Methods section 2.5.5). All mice that were assigned to the microinfarct group underwent the same experimental procedures as in the first experiment (see Material & Methods section 2.2.2; each injection= 1138 microspheres/100 µl) however, the side of injection (left or right CCA) for both sham and microinfarct mice was based on paw preference during the second phase of the SPRT baseline training (sham and IVM injections: contralateral to preferred paw; see Materials & Methods section 2.5.5). For sham injections, the same steps were completed; however, 100 µl of saline was injected into the CCA rather than the microsphere working solution. Following sham and IVM surgeries, motor performance using the SPRT was scored every day while the remaining behavioural tasks were assessed on days 3, 7, 14 and 21, followed by all mice being sacrificed the next day. Data were collected and analyzed for the remaining 28 mice (sham= 14; microinfarct= 14; mortality rate= 15.2%). The day after all behavioural testing was completed, all mice were euthanized in the same manner as in the first experiment (see Materials & Methods section 2.4). Brains were removed and kept in storage for further processing.

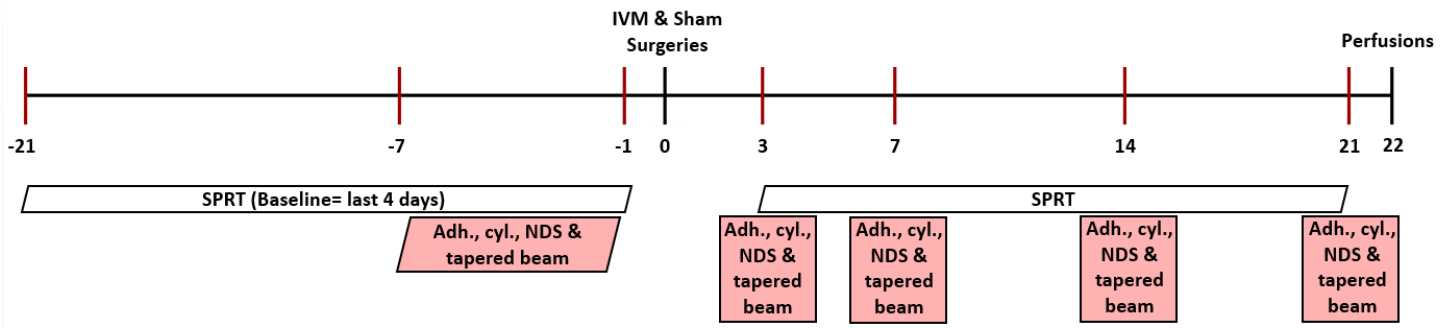

Figure 7. Experimental timeline for behavioural testing of mice before and after sham and IVM surgery. Single pellet reaching task (SPRT; baseline testing = -22 to -1 days prior to surgery; days 3-22 post-surgery), adhesive removal test (adh), cylinder test (cyl) and tapered beam were tested at baseline (1 week prior to surgery) and days 3, 7, 14 and 21 post-surgery. All mice were perfused once behavioural testing was completed (Sham= 14; IVM= 14).

2.5 Behavioural Testing

Every behavioural test, except for the NDS, was recorded using a Raspberry Pi camera to capture high definition videos of each mouse's performance.

2.5.1 Neurological Deficit Score (NDS)

The NDS was used to assess neurological impairments following sham and microinfarct surgeries [50]. This test consisted of four categories that were scored separately, where both the left and right side of the body were evaluated (max score= 16). Mice were placed on a flat surface and gently lifted by the base of their tails until the forepaws were no longer touching the table. Forelimb flexion **(0-2)** was graded from 0 (uniform extension of forelimb), to 2 (full wrist flexion / shoulder adduction) where a score of 1 represented shoulder adduction. Hindlimb flexion **(0-1)** was graded similarly to forelimb flexion. A score of 0 represented the absence of hindlimb flexion whereby a mouse extended its hindlimbs parallel to its body and a score of 1 signified the presence of hindlimb flexion. To observe C-shape lateral bending of the body **(0-2)**, the mouse was again lifted by the base of its tail and held several inches above the surface of the table to observe which side the mouse bent its torso towards. This allowed the experimenter to note whether the mouse had no impairment (0= absence of C-shaped bending), impairment was slightly present (1= mouse bent its torso slightly) or if the mouse had a severe C-shape bending of the body (2= complete trunk flexion) on either side of the body. The last category was the forepaw grasp **(0-3)** graded with a 0 (normal grasping behaviour with both paws), 1 (grasps normally with one paw and uses some contralateral digits), 2 (grasps normally with one paw and uses contralateral wrist/arm) or a 3 (cannot grasp with either paw). The experimenter observed each paw by gently lifting the mouse by the base of its tail and placing it above a horizontal metal wire where it used its forelimbs to grasp the wire. For Experiment 2, mice were scored at baseline and days 1, 3, 7, 14 and 21 post-surgery. Once all data collection was completed, left and right side scores were summed together (all categories) for each mouse at each time point.

To determine whether microinfarction resulted in neurological impairments, the mean NDS score was calculated for both groups and graphed across experimental time points. The NDS ranged from 0 (no neurological impairments) to 16 (severe neurological impairments).

2.5.2 Tapered Beam Test

The tapered beam test was used to assess forelimb and hindlimb function and balance in mice while crossing a tapered beam (length: 100 cm, tapered from 3.5 cm (start) to 0.5 cm (end); ledges: 1 cm below the upper surface and 1 cm wide) [79] to their home cage (Figure 8). A mirror was placed on the right side of the beam against the wall to easily visualize if the mouse displaced its foot from the upper surface of the beam. This task required the mice to cross a beam that gradually become narrower towards the end. Over the course of one training day, mice were habituated to the task by being placed at different intervals along the beam (⅓ from the end, ½ along the beam, at the start of the beam) starting closest to their home cage (end of beam). Once they learned to walk along the entire beam without turning backwards, each mouse was video recorded the same day to capture their baseline performance (3 runs along the beam/mouse). On testing days, mice had to cross the beam three times while being filmed. All runs were recorded using a Raspberry Pi camera (mounted on a tripod that was placed horizontally to the beam). Mice were tested at baseline and days 3, 7, 14 and 21 following surgery. The total number of steps taken along the beam and number of foot faults was counted over the three trials by scoring the videos frame-by-frame for each mouse. The percentage of foot faults was calculated as shown below. The mean was calculated across all three trials for each mouse and followed by the average being taken for each group (sham and microinfarct).

$$\%\, Foot\ Faults = \frac{Total\ \#\ of\ foot\ faults\ from\ contralateral\ paw}{Total\ \#\ of\ steps\ of\ cotralateral\ paw} \times 100$$

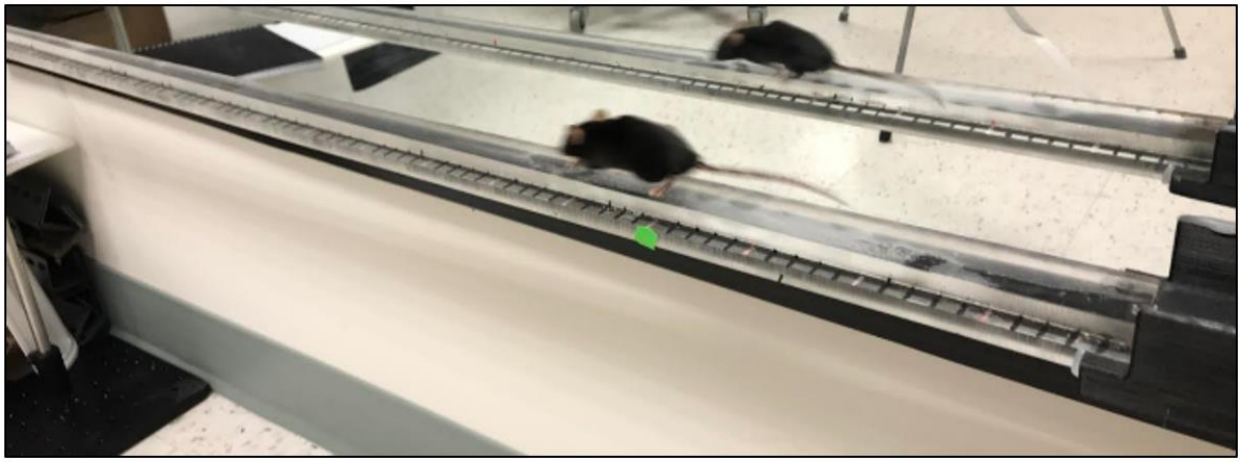

Figure 8. Tapered beam task used to assess balance, forelimb and hindlimb function.

2.5.3 Adhesive Removal Test

The adhesive removal test was used to assess sensorimotor deficits (e.g. tactile responses) and motor asymmetry. This task was completed by placing a small piece of adhesive tape (0.5 cm^2) on the palms of both forepaws followed by placing the mice into a clear, hollow, Plexiglas cylinder (height= 15 cm, diameter= 10 cm; Figure 9A). Mice were filmed from below a clear tabletop, where they had to remove both pieces of tape prior to being taken out of the cylinder; a maximum of 2 minutes was the time limit that was given for this task. If the mouse did not remove the tape from its paw within the fixed time, the mouse received the maximum time of 120 seconds. Baseline testing consisted of 5 days, where the first 3 days were considered as training days and the last two days (days 4 & 5) were testing days. Mice were also tested once on days 3, 7, 14 and 21 following surgery. The videos were analyzed frame-by-frame to record the time it took the mouse to make contact with its mouth to the tape (Figure 9B) and the time at which the tape was removed (completed for both forepaws). All measures for baseline scores were averaged across the last two days and compared against the scores from each experimental time point to determine if microinfarction resulted in sensorimotor deficits.

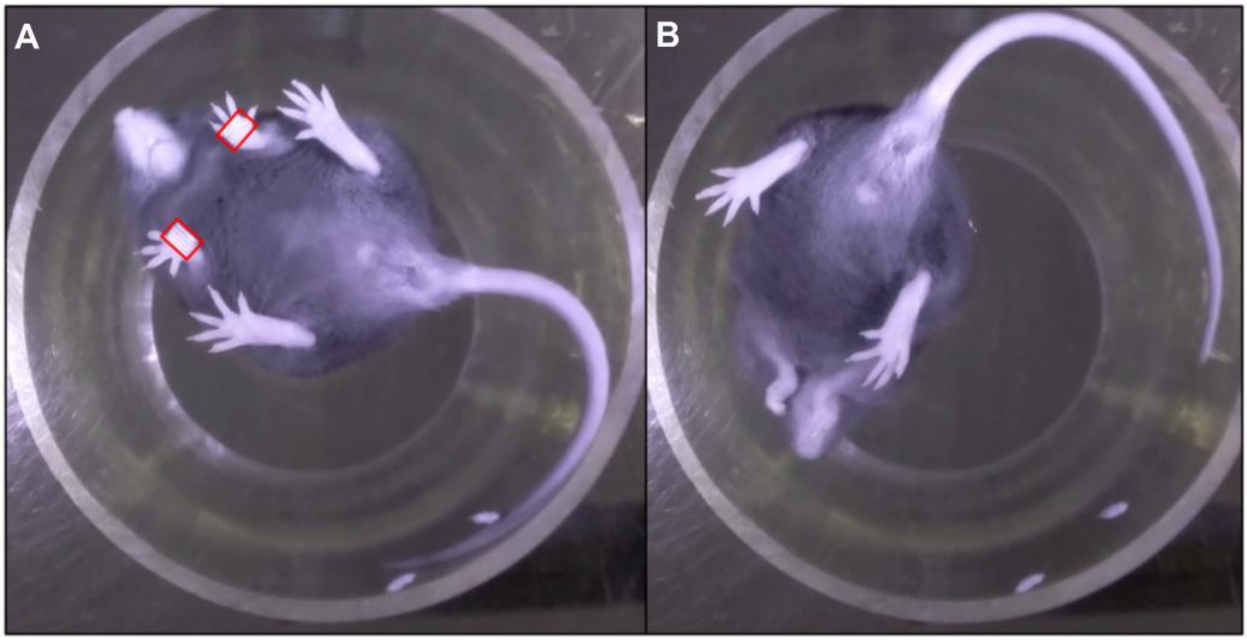

Figure 9. Adhesive tape removal task used to assess sensorimotor deficits. (A) Adhesive tape attached to both forepaws. (B) Mice had to make contact with each paw to remove the tape.

2.5.4 Cylinder Test

The cylinder test was used to assess spontaneous forelimb use and asymmetry. Mice were placed in a hollow, Plexiglas cylinder (height= 15 cm, diameter= 10 cm) where they explored the environment until 25 rear ups with its forepaws against the cylinder were completed (Figure 10A). A rear up consisted of the mouse rearing onto its hindlimbs and touching the wall of the cylinder with either paw or both forepaws (Figure 10B). The first contact on the wall within each rear up was scored, followed by the mouse placing their paws on the floor before the next rear up was assessed. All movements were recorded from below a clear tabletop with the Raspberry Pi camera. No training days were given for this task and testing days were performed at baseline, and days 3, 7, 14 and 21 following surgery. All videos were assessed frame-by-frame to determine which forepaw contacted the wall first (left, right or both). After video scoring was completed for all mice, the percentage use of the contralateral limb was quantified with the equation below. All mice were then placed into their appropriate group (sham or IVM) for further analysis.

$$\%\ \boldsymbol{Use\ of\ contralateral\ limb} = \frac{\frac{\mathbf{1}}{\mathbf{2}}(\#\ \boldsymbol{of\ bilateral\ touches}) + (\#\ \boldsymbol{of\ contralateral\ touches})}{\mathbf{25}\ \boldsymbol{touches}}$$

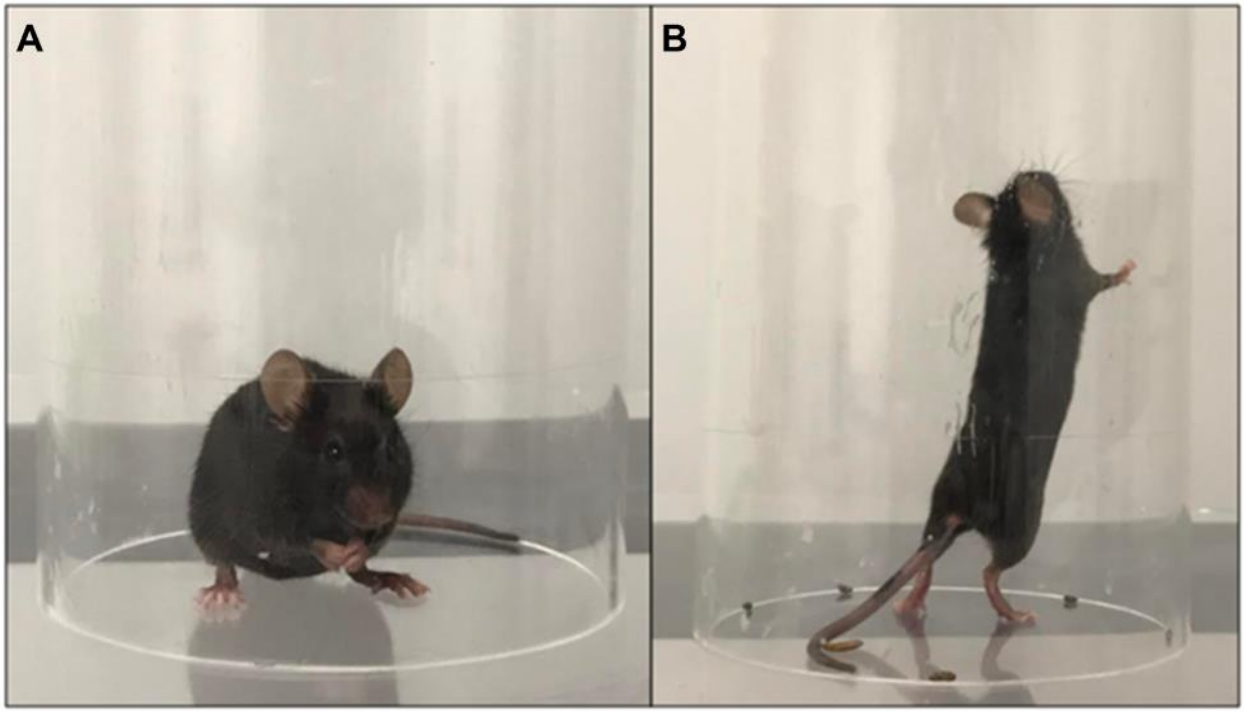

Figure 10. Cylinder task used to assess spontaneous forelimb use and asymmetry. (A) Mice were placed in a Plexiglas box where they explored their environment. (B) A rear up against the wall. The paw that contacted the wall first during each initial rear up was recorded.

2.5.5 Single Pellet Reaching Task (SPRT)

The SPRT was used to assess skilled forepaw use before and after sham/microinfarct surgery by placing the mice in a Plexiglas reaching box (20 cm tall, 19.5 cm deep, and 9 cm wide, measured from outside the box; 0.5 cm thickness of Plexiglas; divot holes ~1.5 cm away from the start of the ledge) and scoring their behaviour based on their ability to reach and grasp a millet seed (Figure 11A). Training and testing days occurred 7 days a week. Two to three days before being habituated to the apparatus, mice were food restricted and millet seeds were introduced within their home cage. The day before the first training day, baseline body weights were recorded. Body weight was maintained at 80% of baseline weight throughout the experiment by giving 1-

1.5g of food per mouse each day once behavioural testing was completed. This was done to ensure that the mice would be sufficiently motivated to reach for the seeds. The first phase of the SPRT (1 day) consisted of the mice having 15 minutes to become habituated to the box while pellets were placed on the floor and reaching tray. This phase allowed the mice to become familiarized with the apparatus and for them to start eating the pellets. The second phase of the task (2-3 days, 10-15 minutes/mouse) was to develop skillful reaching and to determine paw preference. Pellets were placed in both divot holes to give the mice two targets and were replaced right away when they were displaced from the ledge. When the mice developed skillful reaching, paw dominance was determined by analyzing which paw was used most frequently to grasp the pellets. The goal of the third phase (2-3 days, 10-15 minutes/mouse) was to develop a pattern of reaching allowing researchers to analyze each reach as a distinct and separate event. After displacing the pellet from the ledge, whether it was successful or not, the mice had to learn to return to the back wall of the box before the experimenter placed a new pellet. If the mice did not move to the back, a single pellet was dropped at the back of the box to encourage the walk-back. This reinforcement was only done if the mice did not learn the full sequence of the reaching task. Non-rewarding behaviour had to be eliminated (phase 4, 1-2 days, 10-15 minutes/mouse). This was achieved by not replacing the pellet in the next trial if the mouse continued to reach after the pellet was displaced or removed. This taught the mice to sniff and verify if the pellet was in place prior to reaching.

Phases 1-4 occurred within the first week of training, where scoring the performance of the mice (phase 5, 2 weeks) started at the beginning of the second week. Each animal was given a maximum of 10 minutes each day to retrieve up to 30 pellets. If a mouse reached through the slit and obtained the pellet either on its first try or after several attempts, the performance was scored as a successful grasp (Figure 11B). The number of attempts that were made for a successful grasp were scored (i.e. if a mouse successfully grasped a pellet one its 5^{th} try, a total of 5 attempts were recorded). If the mouse pushed or knocked the pellet off of the indentation, it was considered as a knock, and if the pellet fell from their paws, this trial would be scored as a drop. Baseline competency was defined as a plateau in the animal's reaching scores across 4 consecutive days (i.e. the reaching scored from the last 4 testing days did not differ significantly from one another). Experimental testing days began 3 days following the sham/microinfarct surgery and ended at day 21 post-injection. The number of successful pellets retrieved, number

of pellets presented, the percent successful reaches (formula below), and the number of attempts made for a successful grasp were calculated and analyzed before and after stroke for both sham and microinfarct groups.

$$\%\ \boldsymbol{Successful\ Reaches} = \frac{\boldsymbol{\#\ of\ successful\ pellets\ retrieved}}{\boldsymbol{Total\ \#\ of\ pellets\ presented}} \times \mathbf{100}$$

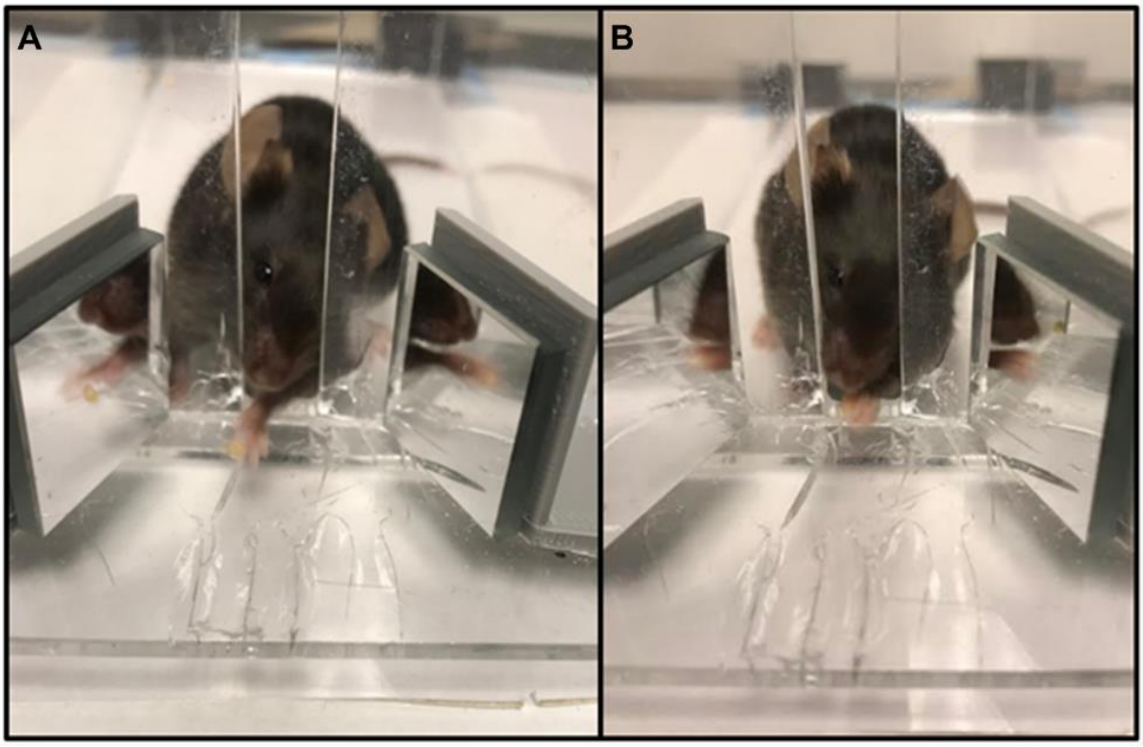

Figure 11. Single pellet reaching task used to assess skilled forepaw. (A) A mouse reaching for a millet seed with its left forepaw. (B) A successful grasp completed.

2.6 Statistical Analysis

Histological data from the first experiment was analyzed using a one-way analysis of variance (ANOVA) and Tukey's post-hoc analysis to assess the amount of EB signal and the total number of IVMs that occurred in both the ipsilesional and contralesional hemispheres at different time points post-microinfarction. A paired sample t-test was used to determine whether there was a significant difference between manually labelled IVMs using histological sections or the blockface images. The behavioural data was analyzed using a three-way repeated-measures ANOVA to test the effects of time and condition (sham vs microinfarction) on motor performance between two cohorts of mice. A paired t-test and a linear regression analysis was used to determine if the number of IVMs that were counted between the user and the automatic IVM detection were significantly different from one another. All statistical analyses were performed using SPSS (IMB Corp., Armonk, USA) and GraphPad Prism 8 (San Diego, CA, USA). All p values <0.05 were considered statistically significant and all values were reported as sample means ± the standard error of the mean (SEM).

RESULTS

Experiment 1

3.1 Time Course of Blood-Brain Barrier Breakdown after Cerebral Microinfarction

The total number of microspheres across the brain was quantified at various time points after IVM surgery. In addition to the raw numbers being assessed, the total number of IVMs in both hemispheres was normalized to the total area of either the ipsilesional or contralesional hemisphere (see Materials & Methods section 2.4.4). A one-way repeated-measures ANOVA with time as a factor indicated that a main effect of time was detected ($p=0.0234$). A post hoc analysis using Tukey's multiple comparisons tests showed that the normalized number of IVMs in the ipsilesional hemisphere was greater at day 21 when compared to day 1 ($*p=0.0261$) and day 3 ($*p=0.0291$) post-IVM surgeries (Figure 12A, E-F). In contrast to the normalized number of IVMs in the ipsilesional hemisphere, no significant differences were observed for the raw number of IVMs that were lodged throughout the ipsilesional hemisphere ($p=0.0968$; Figure 12B). Additionally, no significant differences were detected for the normalized ($p=0.0729$; Figure 12C) and raw number of IVMs ($p=0.0972$; Figure 12D) that were lodged throughout the contralesional hemisphere across experimental days post-surgery.

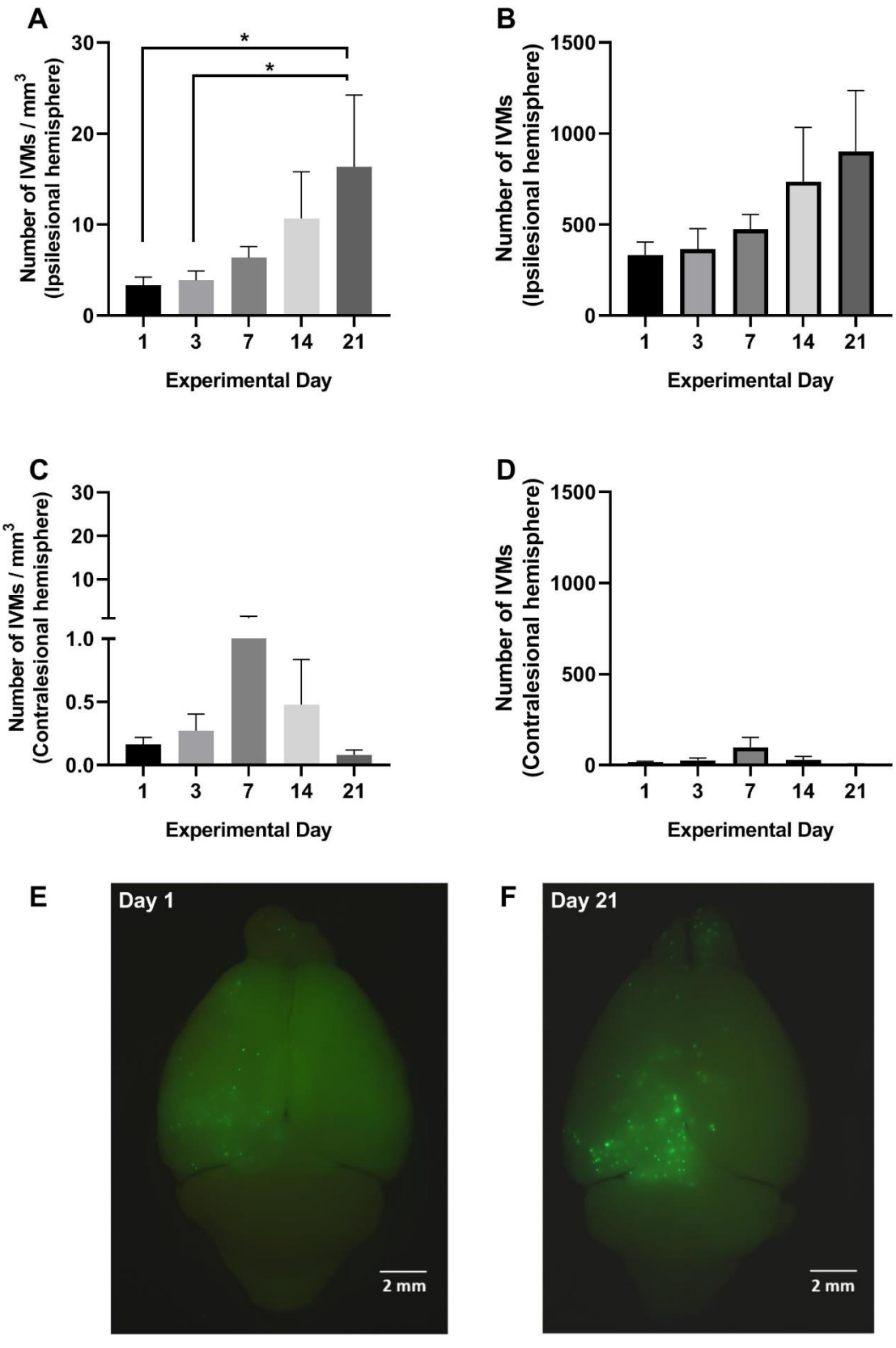
A
Number of IVMs / mm3 (Ipsilesional hemisphere)
30
20
10
0
*
*
1
3
7
14
21
Experimental Day
B
Number of IVMs (Ipsilesional hemisphere)
1500
1000
500
0
1
3
7
14
21
Experimental Day
C
Number of IVMs / mm3 (Contralesional hemisphere)
30
20
10
1.0
0.5
0.0
1
3
7
14
21
Experimental Day
D
Number of IVMs (Contralesional hemisphere)
1500
1000
500
0
1
3
7
14
21
Experimental Day
E
Day 1
2 mm
F
Day 21
2 mm

Figure 12. The number of IVMs throughout the brain across experimental days post-IVM surgery. (A) The number of IVMs in the ipsilesional hemisphere across experimental days post-surgery; normalized to the volume of the ipsilesional hemisphere (n=38). There was a significantly increased (p= 0.0234) number of IVMs (normalized) within the brains of mice that were sacrificed 21 days following surgery when compared to days 1 (*p= 0.0261) and 3 (*p= 0.0291). (B) There was no significant difference in the raw number of IVMs across experimental time points post-surgery in the ipsilesional hemisphere (p=0.0968). (C-D) No significant difference occurred between the normalized (p=0.0728; C) and raw number of IVMs (p=0.0972; D) in the brains of mice across each time point post-surgery. (E-F) A representative dorsal view of GFP-labelled microspheres throughout the brain of a mouse that was sacrificed at 1 day (E) and 21 days (F) post-surgery, illustrating the increased number of IVMs over time. Values are presented as sample means ± SEM.

We wanted to determine how Ilastik based image classification of EB signal throughout the brain compared to human classification, therefore three blinded experimenters manually thresholded images to identify EB labeled region. Using a repeated measures ANOVA, our analysis showed that individual human raters were consistent in their own EB classification; however, classification between each other was significantly different (intra-rater reliability within-subjects $p=0.22$; inter-rater reliability between-subjects $p<0.001$; Figure 13A). Once Ilastik batch processed the remaining test set, it was determined there was an increase amount of EB signal within the ipsilesional cortex compared to the contralesional cortex (Figure 13B). Furthermore, the difference in methods (automated vs manual) further assessed that there was an increase amount of EB signal within the ipsilesional hemisphere compared to the contralesional (Figure 13C). The area of EB signal that was manually identified was then compared to what Ilastik classified as EB signal. A linear regression analysis was then used to model the relationship between the Ilastik EB classification with the between-rater agreement of EB classification. These two classification methods had a strong linear relationship in detecting EB signal ($p<0.05$; $r=0.86$; $r^2=0.74$; Figure 13D). Therefore, Ilastik was able to accurately predict EB signal.

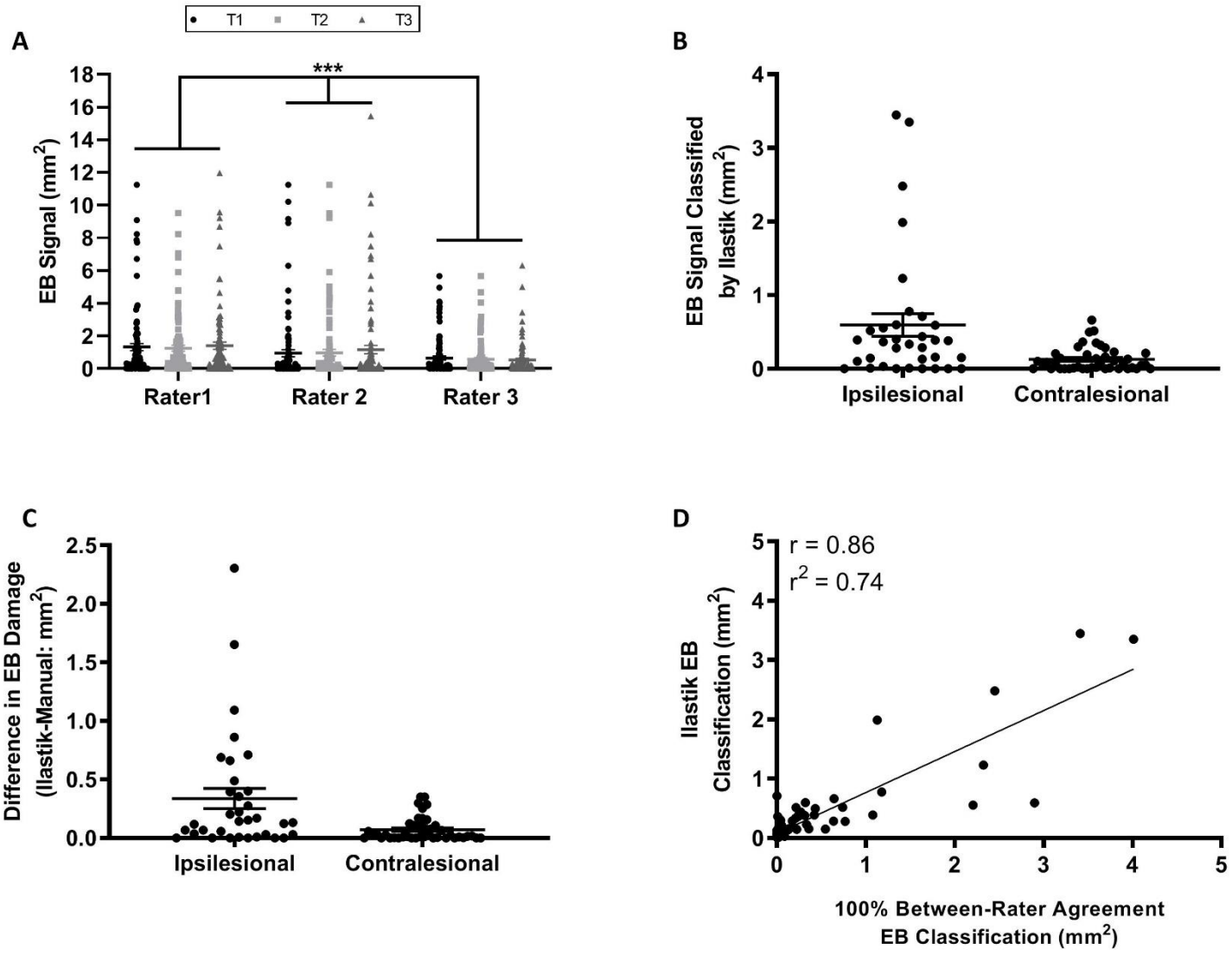

Figure 13. Ilastik EB Classification. (A) EB Classification across 100 images scored 3 separate times. Statistically significant difference for inter-rater reliability between subjects (***$p<0.001$) while intra-rater reliability within subject was not significant ($p=0.22$). (B) EB signal in both ipsilesional and contralesional cortex. As expected, Ilastik detected EB signal to a much greater extent in the ilpsilesional cortex. (C) Difference (Ilastik-Manual training) in EB damage within a given hemisphere. An example of the two largest outliers are presented in Figure 9, panels A and B. Automated and manual methods were equivalent in detecting the EB damage in either hemisphere. (D) Correlation between Ilastik EB classification and manual EB classification. These two measures of EB were significantly correlated ($n=77$; $p<0.05$; $r=0.86$; $r^2=0.74$). Values are presented as sample means ± SEM.

To determine the time course of BBB disruption, the EB signal detected in each coronal section was analyzed using Ilastik, followed by the volume being quantified in Image J. Similar to the total number of IVMs, the EB volume was normalized to the total area of either the ipsilesional or contralesional hemisphere to determine the total volume of EB dye in both hemispheres. A one-way repeated-measures ANOVA with time as a factor indicated that IVM injections resulted in time-dependent BBB permeability after surgery ($p=0.0104$; Figure 14A, E-F). A post hoc analysis using Tukey's multiple comparisons tests revealed that the EB extravasation within the ipsilesional hemisphere was significantly larger one day ($p=0.0104$) following surgeries when compared to mice sacrificed at 3 days ($*p=0.0138$) and 21 days ($*p=0.0224$) post-IVM surgeries. In contrast to the ipsilesional hemisphere, there was no significant change in EB volume that occurred throughout the contralesional hemisphere post-surgery ($p=0.1579$; Figure 14B), indicating that most of the BBB disruption was unilateral. Additionally, within the mice that were sacrificed 1 day following surgery, there was no significant correlation between the number of IVMs that were detected within the ipsilesional hemisphere to the volume of EB ($p=0.7262$; $r^2= 0.01863$; Figure 14C; $n=9$). While the number of IVMs was not significantly correlated to the volume of EB, we were interested in knowing the distribution of the IVMs and EB volume throughout the anterior/posterior axis of the mouse brain. The number of IVMs and EB volume in the lesioned hemispheres were averaged at each anterior-posterior coordinate and normalized to the area of each corresponding brain section (Figure 14D) for mice that were sacrificed one day following surgery ($n=9$). This graph illustrates the distribution of lodged IVMs throughout the brain, specifically the motor cortex region (dotted black lines) along with the volume of EB extravasation observed. Throughout the motor cortex there is an even distribution of IVMs and EB signal, where these numbers increase going towards the posterior end of the brain. Importantly, our analyses only extended 1.8 mm posterior of bregma.

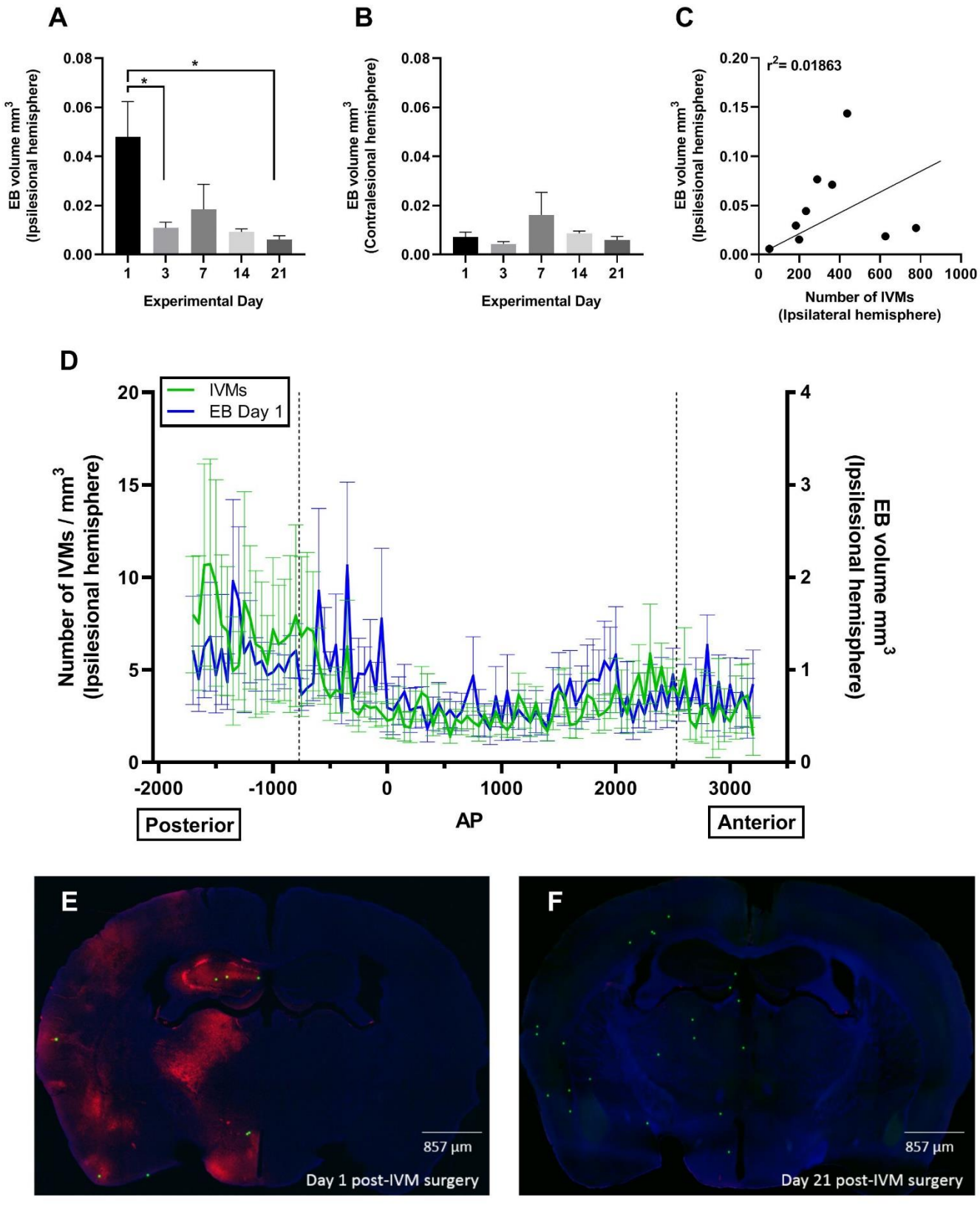
A
EB volume mm3 (Ipsilesional hemisphere)
0.08
0.06
0.04
0.02
0.00
*
*
1
3
7
14
21
Experimental Day
B
EB volume mm3 (Contralesional hemisphere)
0.08
0.06
0.04
0.02
0.00
1
3
7
14
21
Experimental Day
C
EB volume mm3 (Ipsilesional hemisphere)
r2= 0.01863
0.20
0.15
0.10
0.05
0.00
0
200
400
600
800
1000
Number of IVMs (Ipsilateral hemisphere)
D
IVMs
EB Day 1
Number of IVMs / mm3 (Ipsilesional hemisphere)
20
15
10
5
0
EB volume mm3 (Ipsilesional hemisphere)
4
3
2
1
0
-2000
-1000
0
1000
2000
3000
Posterior
AP
Anterior
E
857 µm
Day 1 post-IVM surgery
F
857 µm
Day 21 post-IVM surgery

Figure 14. EB extravasation and volume of damage across experimental days post-IVM surgery. (A) The change in volume of EB extravasation throughout the ipsilesional hemisphere of mice at each time point post-surgery (n= 35). There was a significant increase (p=0.0104) in the amount of EB signal 1 day following surgeries when compared to days 3 (*p=0.0138) and 21 (*p=0.0224). All volumes were normalized to the area of the ipsilesional hemisphere. (B) The volume of EB extravasation in the contralesional hemisphere at each time point post-surgery (n=35). There was no significant different between the volume of EB dye between experimental days (p=0.1579). All volumes were normalized to the area of the contralesional hemisphere. (C) There was no significant correlation between the number of IVMs and the volume of EB dye (normalized) throughout the ipsilesional hemisphere at day 1 post-surgery (p=0.7262; r^2= 0.01863; n=9). (D) The distribution of IVMs and the volume of EB dye throughout the anterior/posterior axis from mice that were sacrificed the day after surgeries. Both IVMs and the volume of EB were normalized to the area of each ipsilesional hemisphere (dotted lines= motor cortex). (E-F) The change in EB extravasation throughout the lesioned hemisphere between days 1 and 21 day post-IVM injections (images captured at 4x magnification; red=EB, green=IVM, blue=DAPI; n=35). Values are presented as sample means ± SEM.

Several brains from the first experiment were analyzed using a custom Python script to localize the number IVMs throughout the brain, whereby manual and automated IVM detection was compared. Using a paired t-test and a linear regression analysis, we determined there was no significant difference between the number of IVMs that were counted between the user and the automatic IVM detection (Figure 15B; mean of differences (Auto-Manual) = -84.25 ± 68.81; p=0.3), resulting in a strong significant correlation between the two methods (Figure 15C; r^2=0.93; p=0.0001). Individual paired t-tests were used to analyze the difference between user and automated detection and registration of IVMs in specific brain regions (Figure 15D-F). No significant differences were observed between the two methods (manual vs. auto) for IVMs located in the primary motor area (mean of differences = 0.2500 ± 5.314; p=0.9638), primary somatosensory area (mean of differences = -4.375 ± 7.018; p=0.5528) and the striatum (mean of differences = -7.000 ± 13.73; p=0.6259). Our Python script further allows us to automatically detect and register IVMs to areas of interest throughout the entire brain (Figure 15G) and at different levels of an anatomical tree (Figure 15H-K). Significantly more IVMs were detected in the blockface images when compared to histological sections (n=8 same brains used from Figure 14; mean of difference= -174.1 ± 72.52; p=0.0474; Figure 16A). This decrease of IVMs in histological sections was likely a result of dealing with fine delicate tissue, where IVMs may have fallen out during sectioning or while manipulating the sections on the slides. While there may be a subtle difference between both quantification methods, there is still a significant

correlation between quantifying histological sections and blockface images (Figure 16B; r^2=0.9204; p<0.0001).

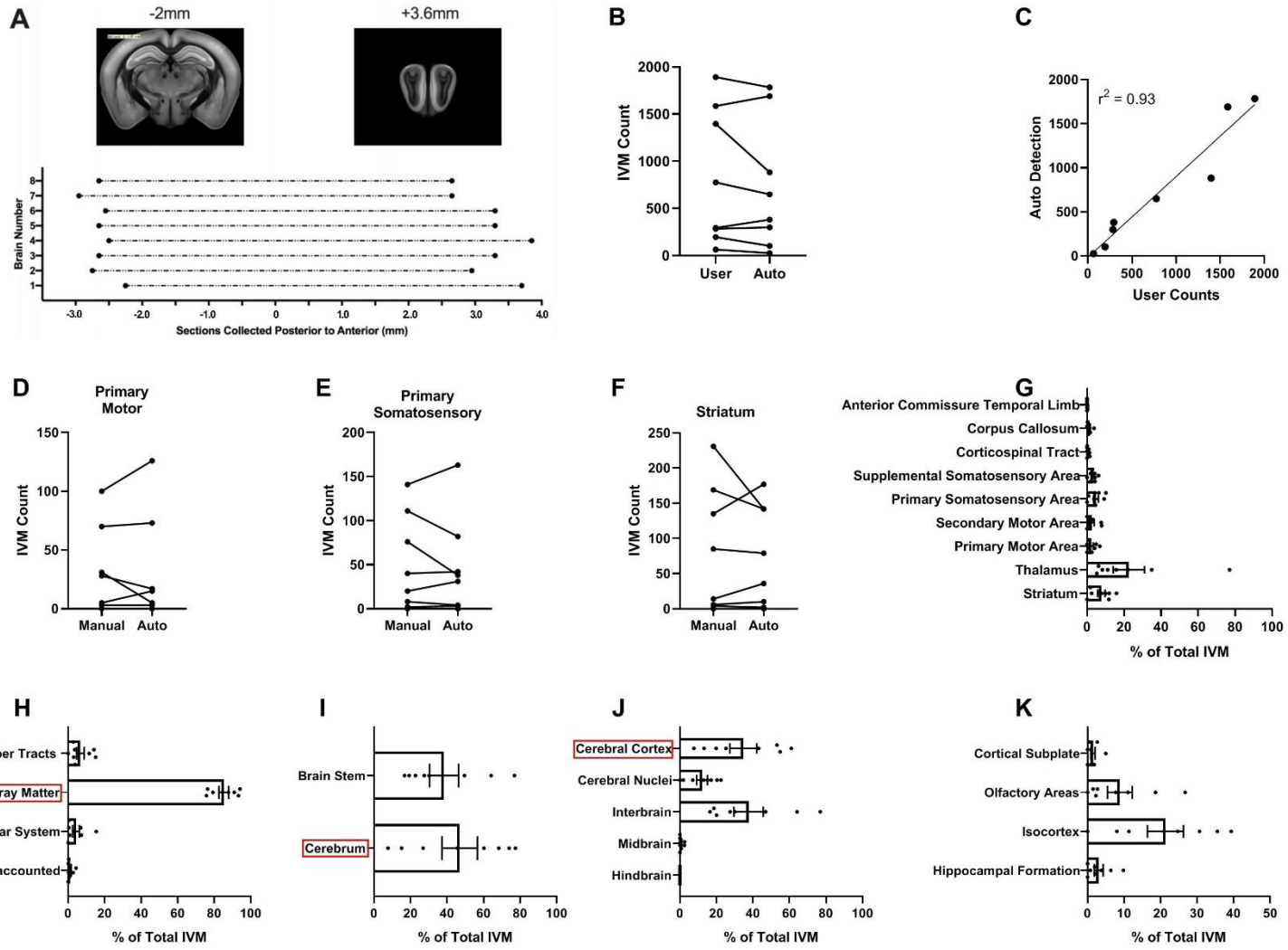

Figure 15. Comparison between manual and automated IVM detection. (A) Coronal sections collected for each mouse brain via blockface imaging (n=8). (B) User identified IVMs vs. automatic detection; no significant difference between methods (mean of differences (Auto – Manual) = -84.25 ± 68.81; p=0.3). (C) The number of IVMs counted by the user vs. automated IVM counts are significantly correlated (r^2=0.93). (D-F) IVMs that were manually counted throughout the entire brain, transformed and registered based on our Python script and ANTs vs. IVMs that were automatically detected and registered from our Python script and ANTs. (G) Distribution of automatically detected IVMs transformed and registered to areas of interest (based on our Python script and ANTs; percent of total IVMs). (H-K) Percent of total IVMs that were automatically detected at different levels of an anatomical tree based on the Allen Mouse Brain Common Coordinate Framework (Version 3). Brain regions outlined in red are further classified from left to right. Values are presented as sample means ± SEM.

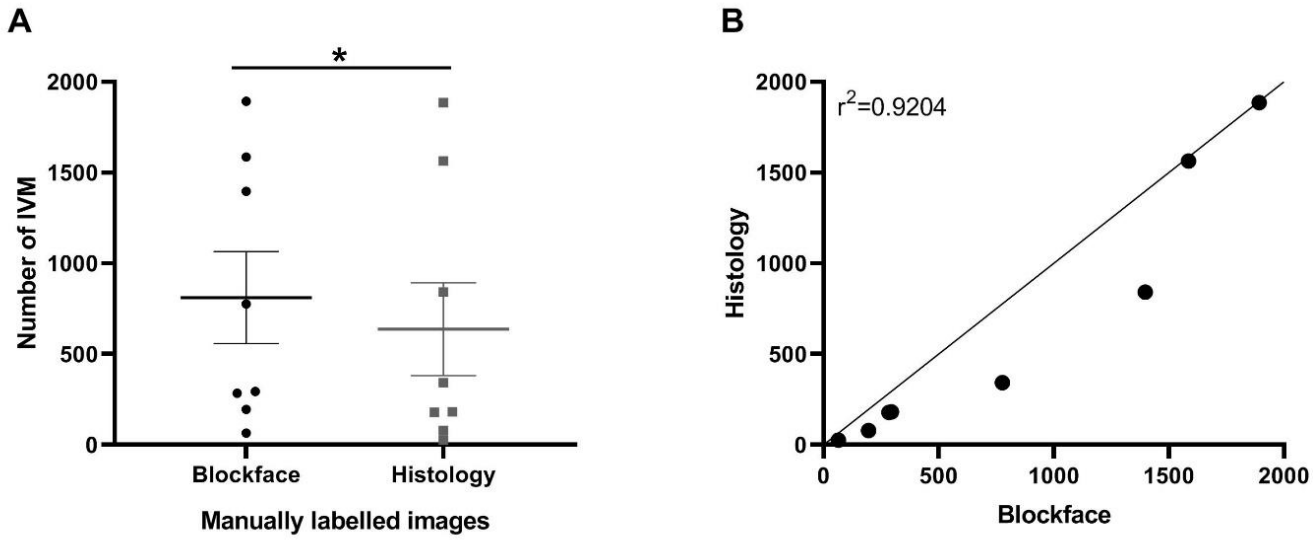

Figure 16. Comparison between manually labelled IVMs in blockface images versus histological sections. (A) The number of IVMs counted in both blockface images was significantly greater compared to IVMs counted using histological sections (n=8; mean of differences = -174.1 ± 72.52; p=0.0474). (B) Both methods show a strong significant correlation between each other when labelling IVMs (r^2=0.9204; p<0.0001). Values are presented as sample means ± SEM.

Experiment 2

3.2 Cerebral Microinfarction Does Not Impact Motor Function

To determine if IVMs induced motor impairments over time, mice were tested on a battery of gross and fine motor behavioural tests at baseline and days 3, 7, 14 and 21 following sham and IVM surgeries. A three-way repeated-measures ANOVA was used to test the effects of time and condition (sham vs IVM) on motor performance between two cohorts of mice. No significant differences were observed between the two cohorts of mice on all tasks ($p>0.05$). Therefore, data from both cohorts of mice were collapsed together. The NDS was used to assess possible neurological deficits post-surgery. A repeated-measures ANOVA showed no group effect ($p=0.824$) nor a group x time interaction ($p=0.737$); however there was an effect of time ($p=0.009$) in both sham and IVM mice across all experimental days post-surgery (##$p<0.001$). In fact, the deficit in NDS score following surgery was persistent and remained elevated between days 1 to 21 for both groups (Figure 17). The tapered beam task was used to assess forelimb and hindlimb function and balance before and after sham and IVM surgeries. A repeated-measures ANOVA indicated that there was no effect of time ($p=0.176$) or group ($p=0.277$) for the percentage of forelimb faults. However, a post hoc analysis indicated a group x time interaction ($p=0.039$), resulting in sham mice having a significant increase in the percentage of foot faults by their contralateral forelimb when compared to IVM mice at day seven following surgery ($p=0.034$; Figure 18A). The difference between sham and IVM mice was not persistent and normalized by day 14 post-surgery ($p=0.440$). Moreover, there was no effect of time ($p=0.605$), group x time interaction ($p=0.969$) or group effect ($p=0.384$) for the percentage of foot faults done by the contralateral hindlimb (Figure 18B). In addition to the contralateral forelimb and hindlimb, the percentage of foot faults were also analyzed for the ipsilateral forelimb and hindlimb (Supplementary Figure 22). A repeated-measures ANOVA indicated no time ($p=0.828$) or group effects ($p=0.103$); however, a significant group x time interaction ($p=0.001$) was observed. A post hoc analysis revealed that the group x time interaction occurred 7 days following surgery ($p=0.034$) resulting in IVM mice having a significant increase in the percentage of foot faults using their ipsilateral forelimb. This difference in foot faults between groups was not observed at days 14 and 21 (Supplementary Figure 22A) post-surgery. For the percentage of ipsilateral hindlimb foot faults, a repeated-measures ANOVA showed no time

effect (p=0.796), group x time interaction (p=0.893) or group effect (p=0.581) (Supplementary Figure 22B).

The adhesive removal test was used to evaluate sensorimotor deficits and asymmetry before and after sham and IVM surgeries. A repeated-measures ANOVA showed no group effect (p=0.959) for the amount of time it took mice to make contact with the adhesive tape; however, a group x time interaction (p=0.038) was evident seven days following surgery where sham mice took longer to make contact with the tape on their contralateral paw when compared to IVM mice (Figure 19A). Furthermore, a post hoc analysis showed a time effect (p=0.002) at day 7 (p<0.001), 14 (p=0.037), and 21 (p=0.018) following surgery, whereby IVM mice showed a decrease in the time that was needed to make contact with the adhesive tape compared to baseline and day 3 performance. When assessing the amount of time it took the mice to remove the tape from their contralateral paw (Figure 19B), a repeated-measures ANOVA showed no group effect (p=0.569) or group x time interaction (p=0.78) over time. Both groups of mice removed the tape faster after 1 week post-surgery, where a post hoc analysis indicated a significant time effect (p=0.005) at days 7 (p<0.001) and 14 (p=0.006). Ipsilateral contact and removal times were further assessed (Supplementary Figure 23). For the contact time using the ipsilateral forepaw, no group effect (p=0.753) or a group x time interaction (p=0.43) were observed; however, significant time effects (p=0.011) were detected at days 7 (p<0.001), 14 (p=0.028), and 21 (p=0.012) following surgery (Supplementary Figure 23A). These time effects were due to both sham and IVM mice contacting the tape faster on their ipsilateral paw 7 days post-surgery. Following day 7, sham mice took longer to make contact with the tape while IVM mice remained below baseline performance. The repeated-measures ANOVA showed that the time it took to remove the tape from the ipsilateral paw resulted in no significant group effect (p=0.585) or group x time interaction (p=0.317). However, a post hoc analysis showed a time effect (p=0.022) that occurred 7 days (p<0.001) after surgery, in which both groups took less time to remove the tape from their ipsilateral paw (Supplementary Figure 23B).

The cylinder task was used to assess spontaneous forelimb use and asymmetry before and after sham and IVM surgeries. A repeated-measures ANOVA showed no group effect (p= 0.561), group x time interaction (p=0.415) or time effects (p=0.972) for the use of the contralateral forelimb (Figure 20) or ipsilateral forelimb (no group effect p=0.561, group x time interaction

p=0.415 nor a time effect p=0.972 were observed; Supplementary Figure 24). Though no significant effects were detected, over time the IVM mice show a slight increase in their preference for the ipsilateral forepaw compared to baseline performance. While the SPRT was used to assess skilled forepaw use before and after IVM and sham surgeries, a repeated-measures ANOVA showed no group effect (p=0.545) nor a group x time interaction (p=0.211) for the percentage of successful reaches. However, there were significant time effects (p=0.01) that were detected using a post hoc analysis between days 3-6 (p=0.008) and days 7-10 (p=0.024) when compared to baseline performance (Figure 21). These time effects resulted in both groups of mice showing a decrease in the percentage of successful reaches made during days 3-6 post-surgery. Following days 3-6, IVM mice showed a slow increase in the percent of successful reaches made during days 7-10 while the performance of sham mice remained below baseline scores. In addition to the percentage of successful reaches, three kinds of analyses were performed: the number of successful pellets retrieved, number of pellets presented, and the number of attempts made to successfully grasp a pellet (Supplementary Figure 25). A repeated-measures ANOVA showed that the average number of successful pellets retrieved resulted in no group effect (p=0.353) nor a group x time interaction (p=0.798). However, a post hoc analysis indicated significant time effects (p=0.009) during days 3-6 (p<0.001) and 7-10 (p=0.025) following surgery independent of group (Supplementary Figure 25A). Similarly, no group effect (p=0.269) or group x time interaction (p=0.095) were observed for the number of pellets presented; nonetheless, there was a significant time effect (p<0.001) detected during days 3-6 (p<0.001), where the number of pellets presented decreased for both groups of mice, particularly for the sham mice (Supplementary Figure 25B). Lastly, while there were no group effect observed (p=0.183) using a repeated-measures ANOVA, there was a group x time interaction (p=0.059) for the number of attempts made to successfully retrieve a pellet. A post hoc analysis indicated that sham mice made more attempts between days 3-6 (p=0.036) and 11-14 (p=0.007) (Supplemental Figure 25C) compared to IVM mice. Additionally, a significant time effect (p=0.003) was shown for the number of attempts made across all experimental days post-surgery (days 3-6 p=0.013; days 7-10 p=0.036; days 11-14 p=0.015; days 15-18 p=0.010; days 19-22 p=0.003) independent of the group.

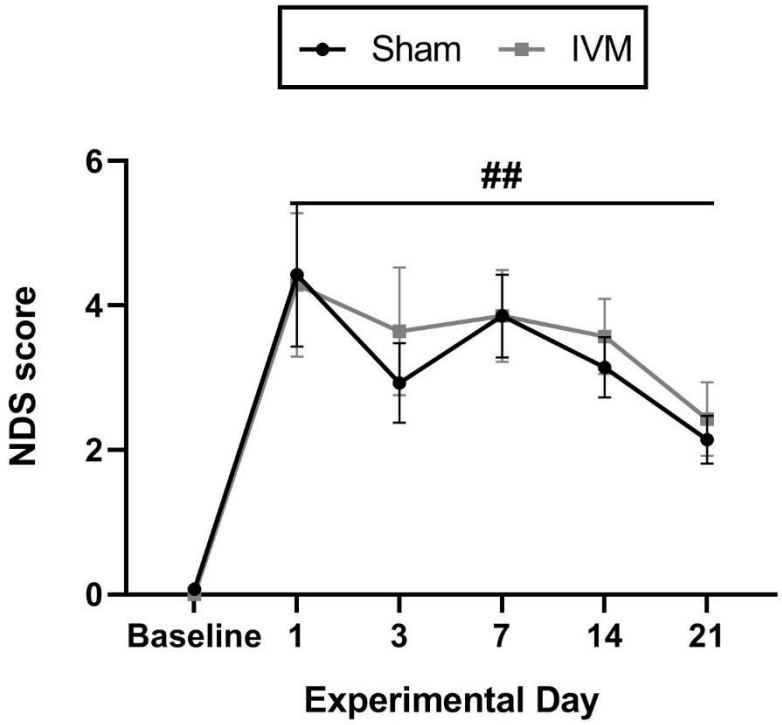

Figure 17. Neurological deficits scores before and after sham and IVM surgeries. NDS scores were taken at baseline and several days following sham and IVM surgeries (days 1, 3, 7, 14 and 21) prior to being sacrificed (sham=14, IVM=14). A time effect ($p=0.009$) was observed between experimental days 1-21 when compared to baseline scores (## $p<0.001$), where both sham and IVM mice had an increase in neurological deficits 1 day following surgery followed by a slow decline throughout the remaining experimental days. No group effects ($p=0.824$) or group x time interaction ($p=0.737$) were observed post-surgery. Values are presented as sample means ± SEM.

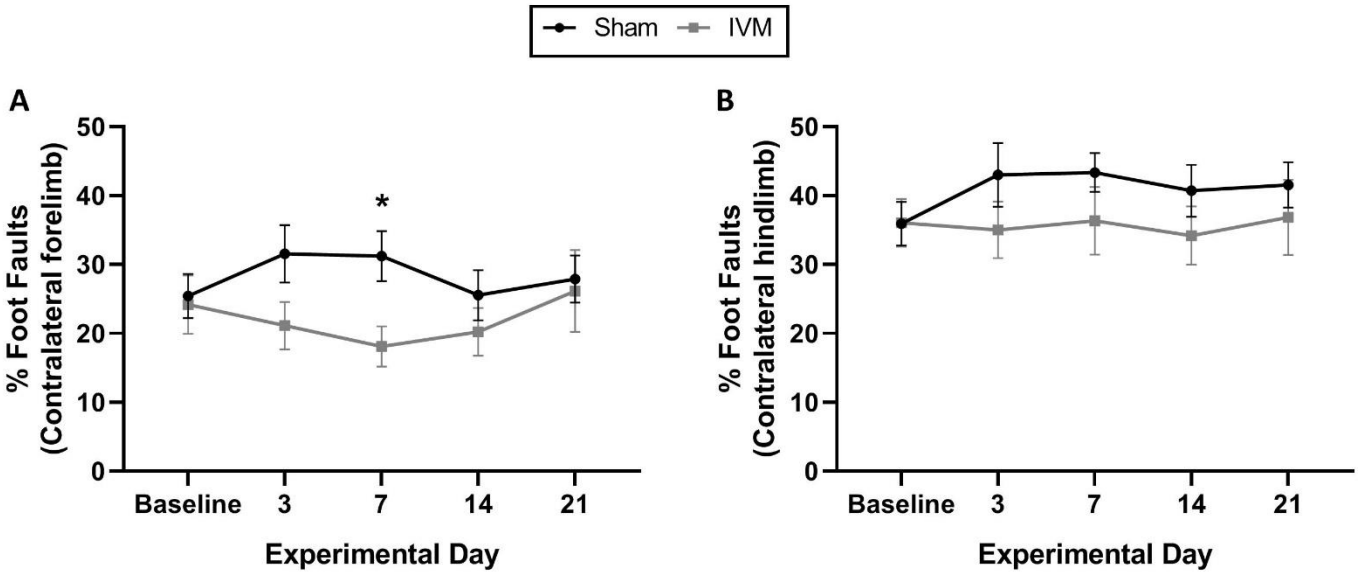

Figure 18. Tapered beam test before and after sham and IVM surgeries. (A) Percent foot faults for the contralateral forelimb. A group x time interaction (p=0.039) occured 7 days following surgery, (*p=0.034) where sham mice had a significant increase in the percentage of foot faults using their contralateral forelimb. An effect of time (p=0.176) or group effect (p=0.277) were not detected across experimental days post-surgery. (B) Percentage of foot faults for contralateral hindlimb (sham=14, IVM=14). No group effects (p=0.384), group x time interaction (p=0.969) or time effects (p=0.605) were observed for the percentage of foot faults of the contralateral hindlimb. Values are presented as sample means ± SEM.

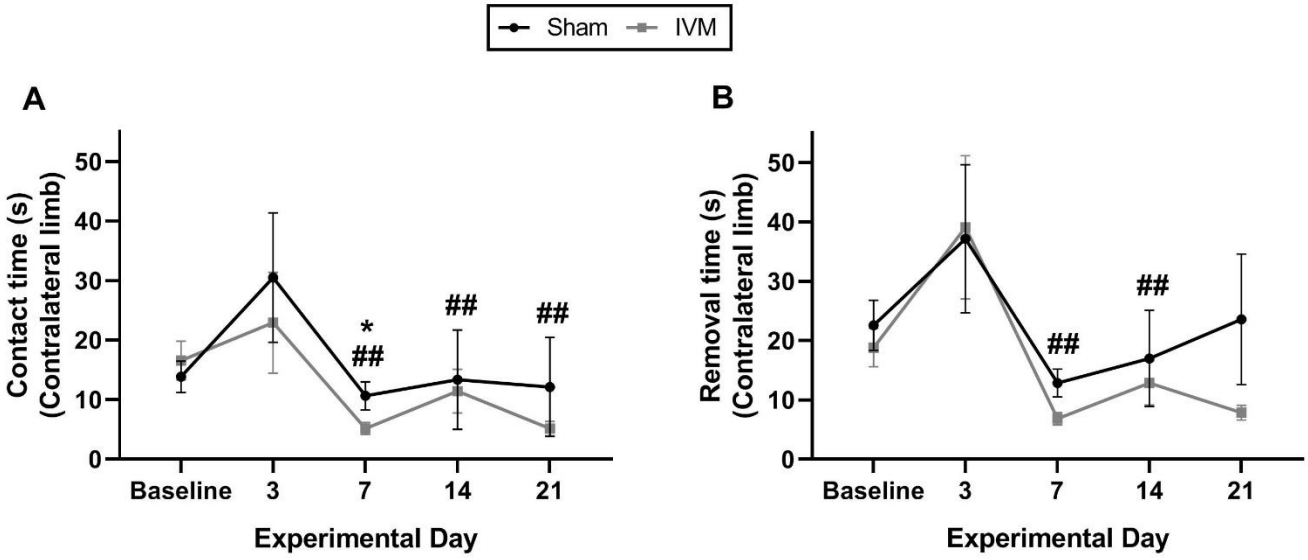

Figure 19. Adhesive removal test before and after sham and IVM surgeries. (A) Contact time made between the contralateral forelimb and adhesive tape. A group x time interaction occurred at day 7 post-surgery (* p=0.038), where sham mice took a significantly longer time compared to IVM mice to make contact with the tape on the contralateral paw. Additionally, an effect of time (p=0.002) occurred at days 7 (##p<0.001), 14 (##p=0.037) and 21 (## p=0.018), where the IVM mice showed a decrease in the amount of time it took to make contact with the tape when compared to baseline performance. No group effect were observed (p=0.959). (B) Removal time of the adhesive tape with the contralateral forelimb. No group effect (p=0.569) or group x time interaction (p=0.78) were observed; however, a time effect (p=0.005) occurred at days 7 (##p<0.001) and 14 (##p=0.006) post-surgery, where both groups of mice showed a decrease in the amount of time it took to remove the tape from their contralateral paw when compared to baseline performance (sham=14, IVM=14). Values are presented as sample means ± SEM.

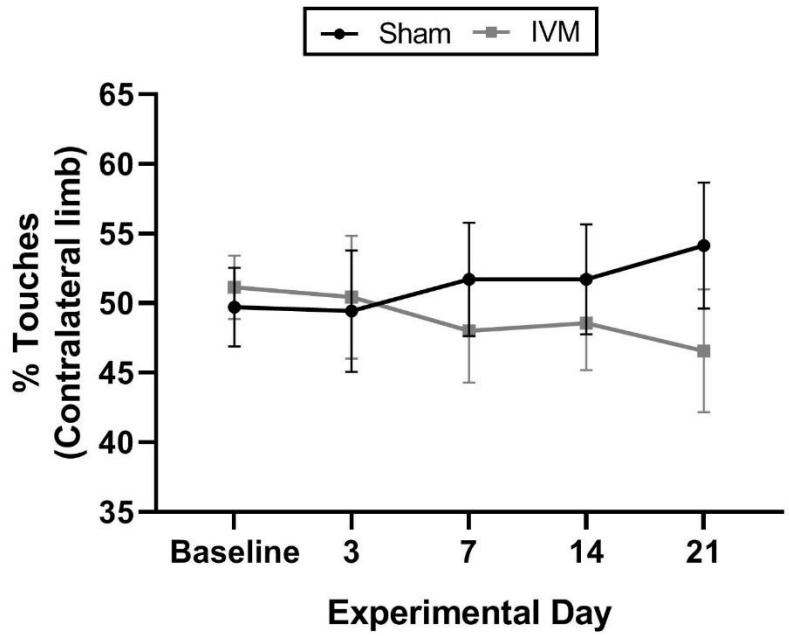

Figure 20. Spontaneous forelimb use in the cylinder test before and after sham and IVM surgeries. The percent touches made by the contralateral forelimb against the wall of the cylinder. No group effects (p=0.561), group x time interaction (p=0.415) or time effects (p=1) were observed across experimental days post-surgery (sham=14, IVM=14). Values are presented as sample means ± SEM.

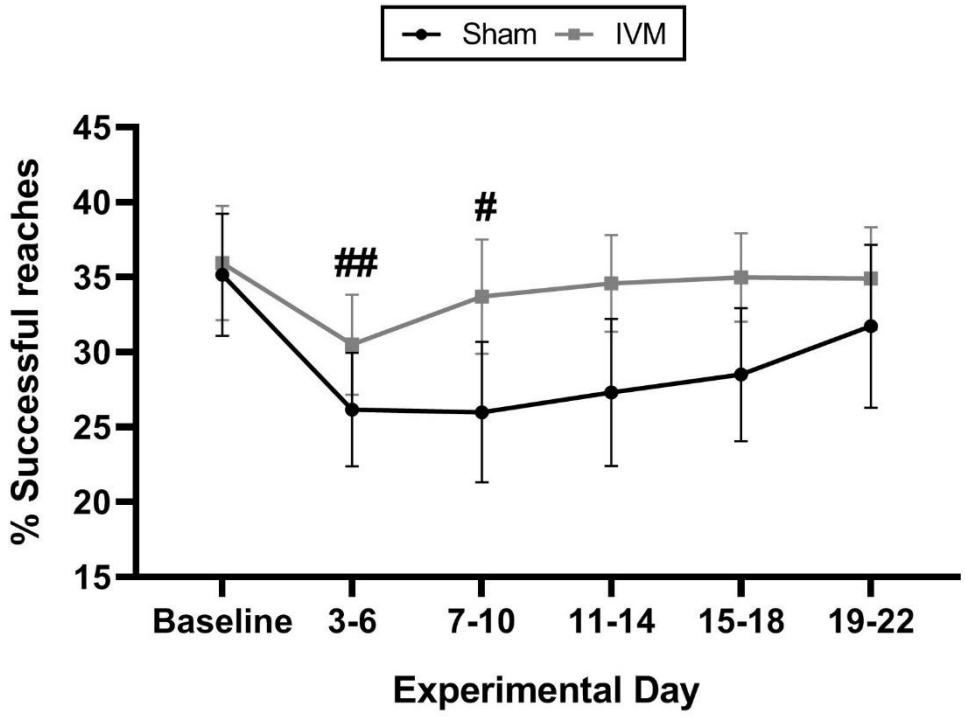

Figure 21. Skilled forelimb reaching in the single pellet reaching task before and after sham and IVM surgeries. The percentage of successful reaches was calculated as [(# of successful pellets retrieved / total # of pellets presented) X 100] for both sham (n=14) and IVM (n=14) groups. No group effects (p=0.545) or group x time interaction (p=0.211) were observed; however there was an effect of time (p=0.01) between bins 2 (days 3-6; ## p=0.008) and 3 (days 7-10; # p=0.024) when compared to baseline performance. These time effects resulted in a decrease in the percent of successful reaches that were made from both groups between days 3-6. Following the first four experimental days, the percent of successful reaches remained below baseline for sham mice (days 7-10) while IVM mice showed an increase in performance, similar to baseline scores. Values are presented as sample means ± SEM.

DISCUSSION

With growing interest in the impact of cerebral microinfarction, there still remains a lack of research in investigating the structural (i.e. brain vasculature) and functional (i.e. cognitive and motor impairments) consequence that these microscopic lesions have on the brain. Using intra-carotid injections of fluorescent microspheres has allowed us to mimic the diverse distribution of infarcts that is seen within the general population. The first study of my thesis addresses whether IVM injections disrupts the BBB and characterizes how long the disruption persists. After a cohort of mice underwent the IVM surgery, an intravascular injection of EB dye through the tail vein was administered 30 minutes prior to the animals being sacrificed at different time points. The total number of IVMs and EB volume was quantified in all animals for each experimental time point. The second experiment of this thesis evaluates the impact of microinfarcts on motor function. The performance of mice was evaluated before and after sham or IVM surgery using a battery of gross and fine motor behavioural tests.

Experiment 1

4.1 The Number of IVMs Increase Over Time After Intra-Carotid Injections Of Microspheres.

A strength of the IVM model of microinfarction is widespread distribution[49]. For the first experiment, the amount and distribution of injected IVMs over time was quantified. It was hypothesized that this model of microinfarction would produce a widespread distribution of IVMs throughout the brain, being variable amongst animals. In agreement with this hypothesis, variation in the number of IVMs between animals was evident. Specifically, we observed a variable distribution of IVMs throughout the ipsilesional hemisphere (average number of total IVMs in ipsilesional hemisphere= 94%) with approximately 6% of total IVMs being located in the contralesional hemisphere. However, it was found that by day 21 post-IVM surgery, the number of IVMs increased throughout the brain when compared to animals that were sacrificed at earlier time points. This increase in IVMs may have potentially been due to the microspheres being lodged within the brain parenchyma over time, while mice that were sacrificed at earlier time points (days 1 and 3) most likely had IVMs remaining within functioning vessels. If this is

the case, those IVMs would have been washed out during perfusions, resulting in a decreased number of IVMs at earlier time points.

Silasi and colleagues performed a similar surgical procedure for IVM injections in mice, however mice were sacrificed at day 8 and 10 following surgery [49]. With the IVM model of microinfarction, they were able to re-create the distribution of the IVMs by reconstructing the brains from low-magnification images (150 µm sections) [49]. With their analysis, only the total number of IVMs were quantified in several brain structures. Although the majority of IVMs were lodged in the cortex and thalamus, the incidence of microinfarction was significantly greater in the hippocampus and white matter[49].

In contrast to the intra-carotid injection of IVMs, Wang and colleagues used a mouse model of diffuse microinfarcts through unilateral injections of 3500 ± 500 cholesterol crystals (40-70 µm in diameter) also through the ICA [13]. In his study, the number of lesions was not reported; however, they were able to report lesion distribution and size within the cortex, subcortical structures, hippocampus and white matter [13]. Their analysis was done by creating a heat map depicting CD68-positive lesion locations (histological marker for reactive microglia and macrophages) [13]. The heat maps were then projected onto three anatomical representative brain sections to quantify both lesion distribution and size [13]. A reduction in lesion size at days 14 and 28 was further observed in incomplete lesions compared to cavitated lesions [13]. Similarly, Rapp and colleagues injected cholesterol crystals (60-100 µm in diameter) through the rat ICA, whereby rats were sacrificed 4 days, 1, 2, and 4 weeks post-injection [48]. Although they reported the infarct volume in rats, where the largest volume of injury was < 2.0 mm^3 after repeated embolization with 150 crystals (using a T2-weighted MRI), there were no data that showed a change in infarct volume over time [48]. In contrast to intra-carotid injections, Summers and colleagues used targeted photothrombosis to occlude single penetrating vessels of the cortex to mimic microinfarction. The hyperintense regions in the inversion recovery T2-weighted, and average diffusion weighted images were manually outlined using MRIcron software [14] to determine the area of damage. However, only the microinfarct area was reported 1-2 days post-occlusion [14]. A limitation of equating larger lesions to individual IVMs is that not all IVMs produce lesions throughout the brain, whereas larger focal strokes can produce discernible tissue damage. This has been seen using the IVM model of microinfarction, where across the entire

brain, only 16.4% of lodged microspheres produced identifiable damage to the neuronal structure [49].

We discovered that over time, there is a significant increase in the number of IVMs that become lodged throughout the brain. This increase in IVMs may have potentially been due to the IVMs bypassing the brain. Smaller branches from the ICA have been shown to circumvent the brain (i.e. posterior communicating arteries) which in turn bypasses the Circle of Willis. An example of such branching includes the opthalamic artery, which leaves the internal carotid artery to supply blood to the eyes [80]. Overall, no other lab has reported the total number of emboli that was lodged throughout each brain over several experimental weeks. Therefore, to confirm if our findings are true, we will continue to increase the sample size at each time point to determine if this increase in IVMs is valid or if the number of IVMs remain consistent over time. In order to quantify and localize the IVMs through the whole brain, our laboratory has used blockface imaging during serial sectioning. The serial images that were captured during sectioning were then used for reconstruction of IVM location along the AP axis of the brain. IVMs were further identified in specific brain regions using the Allen mouse brain atlas.

4.2 IVMs Resulted In Acute BBB Breakdown.

BBB disruption is evident in both clinical and preclinical settings after the onset of a larger focal ischemic stroke [61, 81-82]. In contrast to focal strokes, the time course of BBB permeability when impacted by microinfarcts is not well understood. This study sought to assess whether IVM injections, an animal model of microinfarction, resulted in BBB disruption and for how long the disruption persisted. It was hypothesized that IVM injections would result in acute disruption of the BBB, where EB dye would be most evident within the parenchyma during the first week post-surgery. After processing the EB signal through Ilastik and quantifying its volume in Image J, it was concluded that my hypothesis was supported, whereby EB volume was greatest 1 day post-IVM surgery throughout the ipsilesional hemisphere, followed by the dye being unnoticeable over time. EB volume was also evident within the contralesional hemisphere. Mice that were sacrificed 1 day following IVM surgeries contained approximately 5% of the total number of IVMs and 13% of EB volume in the contralesional hemisphere (ipsilesional hemisphere IVMs= 95%; EB volume= 87%). Since there was a modest amount of IVMs and EB

volume in the contralesional hemisphere, this does not create a problem when analyzing and quantifying the impact our model has on the brain. Within the general population, there's no control over the location of each microinfarct throughout the human brain. Rather than ignoring these numbers, we should appreciate that our model can mimic the reality that these infarcts have on humans and grasp a better understanding as to where each IVM is being lodged throughout the brain and the impact they have on the BBB and surrounding cells. To further investigate the impact of IVMs on BBB integrity, our next steps will be to histologically stain for necrotic cells using Fluoro Jade C stain in order to align sites of EB volume with the number of IVMs and dead neurons.

Though microinfarction is common amongst the elderly population, the time course of BBB disruption has not yet been identified. This lack of evidence is predominantly due to microinfarcts primarily being detected through post-mortem histopathological analyses or on advanced MRI once the patient has suffered from a larger, focal stroke. By the time these microscopic lesions have been detected, the brain has already begun remodelling and clearing out the debris after injury. Additionally, while some studies have assessed BBB leakage in patients impacted by cerebral microinfarction, these patients are also affected by other microvascular pathologies such as CAA [20]. In clinical studies that assess BBB leakage in those affected by microvascular brain pathologies, the results are not caused by microinfarction alone, rather they're influenced by a number of diseases. Therefore, it is difficult to investigate the impact of microinfarction in clinical populations. Most of what we know about BBB integrity comes from the clinical studies that assess focal ischemic strokes [61-62, 81-82]. BBB disruption has been detected using clinical imaging methods, including perfusion computerized tomography (CT), dynamic contrast-enhanced MRI or diffusion weighted imaging (DWI) [83-84]. These modalities are widely used tools that detect the extravasation of intravenously administered exogenous tracers. One clinical study measured the evolution of BBB permeability shortly after acute ischemic stroke in humans using MRI. Each patient initially underwent a single dynamic contrast-enhanced MRI to measure the BBB permeability during their first workup [82]. A total of 42 patients were included in the final analysis, undergoing a second round of dynamic contrast-enhanced MRI approximately 23.8 hours after the onset of stroke symptoms [82]. MRI scans were taken between 1.3-90.7 hours across all patients [82]. BBB permeability was defined using DWI with leakage being highest within the infarct zone compared to the contralateral hemisphere [82].

Notably, the BBB permeability was found to be greatest at 6-48 hours after the onset of the acute ischemic stroke [82]. Similarly, Giraud and colleagues sought to identify MRI factors that were associated with early BBB changes after acute ischemic stroke. A total of 44 patients received admission MRI scans with a follow up MRI within 3 hours after the first scan to analyze BBB changes [62]. In this study, the presence of leptomeningeal and parenchymal contrast enhancement on T1-weighted imaging was characterized as BBB disruption [62]. Follow up examinations and imaging were performed 2 days and 1 month after the last MRI session to assess any BBB changes and infarct size [62]. Their study showed that BBB disruption within the first 3 hours after stroke was uncommon; whereas BBB rupture at later time points was more frequent (2 days after stroke) [62]. Compared to our preclinical microinfarct mouse model where we were able to investigate the impact of IVMs on BBB integrity over 3 weeks, data from both clinical studies was not acquired longitudinally. Although we have knowledge that BBB disruption is occurring several hours after the onset of an ischemic stroke, there is no evidence as to what is happening to the BBB after microinfarction since those acute time points cannot be probed.

Wang and colleagues assessed BBB function 3 days after surgeries (intra-carotid injection of cholesterol crystals or saline injections). Both sham and microinfarct mice were anesthetized and injected with 15 µl 1% Alexa 647-conjugated ovalbumin (OA647) into the blood stream through a femoral artery catheter [13]. Animals were sacrificed 30 minutes after injections, followed by coronal sections being immunolabelled for GFAP and CD68 to identify the location of the lesions. Alexa 647-conjugated ovalbumin extravasation was then imaged within and surrounding areas of the GFAP and CD68 labelled regions [13]. With their microinfarct model, they found that at 3 days post-surgery, mild cerebral edema was observed [13]. BBB disruption was evaluated using the images that captured the OA647 extravasation, showing smaller lesions that contained highly localized BBB disruption while larger lesions had widespread BBB leakage [13]. Additionally, Rapp and colleagues assessed BBB breakdown by evaluating the matrix metalloprotenaise activation, along with albumin extravasation, microglia and astrocyte activation at 4 days, 1, 2, and 4 weeks post-embolization [48]. Coronal sections were used for immunohistochemistry. Microglia and astrocytes were labelled with CD11b and GFAP, while the BBB was assessed using MMP staining by in situ zymography [48]. From their results, BBB leakage was evident at 4 days and did not persist beyond 1 week following injury [48].

With our microinfarct mouse model, we were able to create a time course of BBB disruption, looking at both the acute and delayed changes of the BBB. While many studies, preclinical and clinical, look more at the earlier stages of BBB integrity, it is important to analyze the impact these lesions have longitudinally. It is unclear as to whether the BBB repairs itself quickly and efficiently after stroke by re-establishing cerebral blood flow through the microvascular bed [58], enhancing neurogenesis [85-86] and angiogenesis [87-89], or whether there is a second opening of the BBB. For this experiment, we used EB dye to evaluate BBB disruption post-IVM surgeries; however, this dye normally binds to larger proteins (i.e. albumin) [76]. We concluded that IVMs cause acute BBB disruption that does not persist past one week post-occlusion; however, it is not definite that the BBB is completely sealed at later time points post-surgery. Although larger molecules cannot pass through the BBB over time, there is the possibility of smaller molecules leaking into the parenchyma due to minor openings within the BBB. To continue investigating the impact of IVMs on the brain, we will next evaluate Fluoro Jade C histological staining to determine the location of necrotic cells around each IVM. Additionally, we will examine the correlation between the volume of dead neurons to the number of IVMs being lodged throughout the brain.

4.3 Evans Blue Dye Used For Assessing BBB Integrity

For the first experiment, we used EB dye to assess EB extravasation post-IVM injections to determine the time course of BBB disruption. To do so, mice were intravascularly injected through the tail vein approximately 30 minutes prior to perfusion. To analyze the EB dye, 100 images of varying EB dye were manually thresholded by three independent raters to what they deemed was EB signal. Ilastik, a deep neural net pixel classification software, was then used to train the program to identify EB signal from background noise (i.e. anything without EB). After batch processing the remaining images and creating binary masks of EB signal, Image J software was used to quantify the volume of EB dye. While our lab created a novel method to evaluate EB dye, many labs have had issues with quantifying the magnitude of the dye or BBB dysfunction. This has previously been done by extracting the dye from the tissue using various solvents at different time points and estimating the amount of dye colorimetrically, spectrophotometrically, or fluoro-spectrometrically [76].

Several preclinical models have previously used different methodologies to assess and quantify BBB leakage using EB dye [90-93]. Rather than using conventional ultraviolet spectrophotometry, one preclinical model developed an optical imaging method, based on excitation and emission spectra of EB dye, to evaluate BBB integrity and to quantitatively plot vascular leakage within different brain regions [90]. Heat maps were generated from the images by using filter paper to plot out the EB dye, whereby brain regions with varying amounts of EB dye would exhibit different colours on the map [90]. With this type of method, different areas of a single brain section were used to quantify the signal intensity corresponding to different colour regions [90]. This method has allowed Jaffer and colleagues to quantify the amount of accumulated EB dye in various brain structures in response to BBB disruption [90]. In addition to plotting vascular leakage post-stroke, Reeson and colleagues have used Image J to estimate the distribution of EB dye in different brain regions [91-92]. After inducing a photothrombotic stroke in the forelimb somatosensory cortex, mice were injected with 4% EB dye at 3, 7 and 28 days following stroke [91]. Subsequently to imaging the EB dye in each brain section, all serial images were analyzed using National Institutes of Health Image J software [91]. This software allowed Reeson and colleagues to visualize the extravasation of the dye by subtracting vessel masks from the original image stacks, obtaining superficial, middle, and deep measurements of the EB fluorescence [91].While our lab was able to create a semi-automated method to define regions of EB dye throughout the brain using Ilastik and to quantitatively measure its volume using Image J, these past two studies also generated novel methods to assess BBB disruption between superficial and deep layers of the cortex.

EB dye is a commonly used histological marker of BBB integrity, whereby the number of labs that have used this dye increased over the past several years [76]. Although it may be difficult to accurately assess EB extravasation throughout preclinical models, different modalities exist to evaluate and quantify EB dye.

Experiment 2

4.4 Cerebral Microinfarction Did Not Result In Any Motor Impairments

The objective of the second experiment was to evaluate the impact of IVMs on motor function post-surgery. It was hypothesized that mice with induced microinfarction would have subtle motor impairments acutely after surgery. The battery of behavioural tests included tasks that

were sensitive for detecting minor deficits such as sensorimotor deficits (tactile responses), spontaneous forelimb use and skilled forepaw use. From our data, it was apparent that IVMs did not result in any motor deficits post-surgery when compared to sham-operated mice. These effects may have occurred due to both our sham and IVM surgeries being invasive, which may have potentially led to the sham mice showing comparable neurological deficits and a decrease in motor performance similar to that of IVM mice. Additional explanations for the effects that were observed may have been due to the sensitivity of certain behavioural tests. The NDS and cylinder tests have a very low sensitivity for identifying deficits after induced strokes, while the tapered beam and adhesive removal tests are moderately sensitive [74]. The only behavioural task that was used and is highly sensitive to motor deficits post-stroke is the SPRT [74]. However, because our microinfarct mouse model creates a widespread form of damage, the severity of motor deficits is unlikely to be comparable to the deficits seen with focal ischemic strokes where injury typically targets the forelimb motor cortex. Furthermore, the location of the IVMs throughout the brain has not yet been identified in this cohort of mice. Once all serial images from each brain are analyzed, we will be able to quantify the total number of IVMs that were lodged within the motor cortex region for each animal. Using additional highly sensitive motor tasks (i.e. lever pulling) in future experiments and localizing IVMs throughout the motor cortex region will allow us to determine whether IVMs significantly impact motor function post-surgery.

Although the association between microinfarction and cognitive decline has been previously investigated, less is known about the impact microinfarction has on motor output. One neuropathology study [36] recently associated microvascular brain pathology to late life motor impairment. Brains from 850 deceased participants were evaluated for microvascular brain pathology including cerebral amyloid angiopathy, arteriosclerosis and cerebral microinfarction [36]. Microscopic cerebral infarcts were identified by a neuropathologist after brains were histologically stained with Hematoxylin & Eosin stain [36]. Once the brains were analyzed, the microvascular brain pathology was associated with global motor scores (GMS) proximate to death. The GMS in this study was a compilation of motor tests that included the grip and pinch strength test, finger tapping, Purdue pegboard test, gait and balance [36, 39]. From their study, Buchman and colleagues concluded that cerebral microinfarction was related to decreased motor function, specifically in manual dexterity and gait [36] whereas walking speed and hand strength

were not impaired. While this study contained a large sample size to determine if these microscopic lesions altered motor function, only subtle motor deficits were reported. In contrast, our experiment contained fourteen sham and fourteen IVM mice, both of which showed a drop in performance post-surgery; however, there was no effect of IVMs on motor performance. A large limitation of this clinical-histopathological study is that brain images of other pathological processes were not included in the analysis. This can include white matter integrity, neuronal, glial, or inflammatory changes that may have potentially contributed to the motor deficits that were observed [36]. Although this study was the first to evaluate how microinfarction influences motor function, there still has not yet been an investigation using in-vivo MRI.

While it may be difficult to investigate the relationship between microinfarction and motor function at the clinical level, several preclinical models have used diverse behavioural tasks to investigate how their model impacts behaviour. Wang and colleagues tested their sham and microinfarct mice using an open field test to evaluate the presence of general motor deficits [13]. Both groups of mice were evaluated once a day on days 7 and 14 following surgeries, where they were placed inside an open field arena and their behavioural performance was recorded [13]. The activity of the mice was recorded for 10 minute sessions and it was found that there was no significant difference between both groups over time for the path travelled (a measure of gross motor function) or the percentage of time spent in the middle of the arena (a measure of anxiety) [13]. Similarly, after sham and repeated bilateral injections of cholesterol crystals (given at an interval of 2 weeks), Rapp and colleagues tested both groups of rats using the open field and Rota Rod test [48]. With a 3-day testing period, no significant differences were observed between sham and embolized rats with the open field test [48]. Additionally, both sham and embolized rats improved in motor performance using the Rota Rod test, showing a decrease in fall latency over time [48]. However, the embolized rats had a significantly lower performance compared to the sham rats, making more falls on the rod after 4 days of training [48]. Compared to the cholesterol injection microinfarct models, Balbi and colleagues induced microinfarction in mice in a similar fashion to our IVM injections [50]. The motor performance for both groups of mice was evaluated using the NDS and clasping reflex test [50]. For the NDS, both sham and microinfarct mice received a score of 0 at baseline performance, followed by their scores increasing to 0.1 (sham mice) and 1.8 (microinfarct mice) on average 1 day following surgery [50]. After four weeks, it

was observed that microinfarct mice had a significantly higher NDS score compared to sham mice, indicating impaired motor function [50]. Additionally, microinfarct mice showed a trend of a higher clasping score compared to sham mice receiving a score of 0 each time [50]. In our behavioural experiment, no group effect was observed between sham and microinfarct mice using the NDS; however, both groups showed a time effect across experimental days post-surgery when compared to baseline performance. Notably, while Balbi and colleagues injected 2000 ± 500 microspheres per injection, we injected approximately 1138 microsphere during each injection. The difference in the number of injected microemboli may further explain why we did no see similar behavioural deficits compared to previous studies [13, 48, 50].

Although no motor deficits were observed in our experiment, the battery of behavioural tests were more sensitive for detecting minor deficits compared to the gross motor tasks that were previously used (i.e. open field, Rota Rod and NDS). To continue investigating whether IVMs cause motor impairments, injection of 2000 ± 500 microspheres per microinfarct injection should be completed to determine if a larger number of microemboli produce behavioural impairments and a naïve group of mice will be needed to determine if IVMs are causing the decrease in performance or if both sham and IVM surgeries are invasive enough to cause deficits. Additionally, the brains from these animals will be sectioned and analyzed using our Python script to localize the IVMs and determine how many IVMs were lodged within the motor cortex region. Once we know how many IVMs are located within the motor region, we can look more closely at each animal to determine whether IVMs had a large or subtle impact on their motor performance post-surgery.

Limitations And Future Directions Of The Study

Limitations that arose throughout the first experiment include improper intravascular injections of the EB dye, which resulted in a smaller sample size to assess the BBB integrity post-microinfarction. Furthermore, it has been concluded that while brains are being sectioned, the IVMs are pushed out of the tissue, resulting in a loss of IVMs in histological sections. This in turn allows us to rely on the blockface images to accurately determine the total number of IVMs that have been lodged throughout the brain vasculature. For the second experiment, IVMs did not impact motor performance post-surgery. This may have been a result of both the sham and IVM surgeries being invasive, resulting in both groups of mice showing a decrease in performance

after surgery. It is not surprising that motor impairments were not observed using our battery of behavioural tasks because our IVM injection model produces a widespread form of damage, whereby microinfarcts are typically less than 1 mm in diameter [40]. Mice that are induced with smaller strokes often do not reveal impairments beyond a few days when compared to larger focal strokes that specifically target the motor cortex [48, 50]. Furthermore, since we do not have control over the location of each IVM, it is difficult to determine whether the motor cortex of mice contained IVMs during the testing period. Therefore, to determine if the motor cortex contained any IVMs, we will perform whole-brain localization to determine how many IVMs were lodged in specific brain regions (i.e. motor cortex). Once the number of IVMs has been determined, we will be able to look closely at each individual animal to determine whether IVMs were lodged within the motor cortex and if so, whether IVMs impacted the performance in each behavioural test.

Although we try to align human microinfarction with our widespread distribution of IVMs throughout the brain, a major misalignment with our model is that we are working with young, healthy adult mice, being equivalent to 20 years of age in humans. In the aging population, those that are affected by microinfarction also have other underlying comorbidities [21, 23, 27] or an existing focal stroke [5-8]. In order to precisely align preclinical models with the clinical relevance of microinfarction, it is important to take into consideration all of the possible underlying factors (i.e. age, disease comorbidities, or an existing focal stroke) that are normally seen in humans. Therefore, future work with this model can incorporate age (12-16 months old) and pre-existing stroke conditions or induce a focal stroke post-IVM surgery to determine the impact of microinfarction on the brain as well as behaviour.

CONCLUSION

Our results indicated that cerebral microinfarction in mice resulted in acute BBB disruption, where albumin leakage was significantly greatest one day following surgery and declined throughout the first week. Additionally, while microinfarction has previously been associated with cognitive deficits, a battery of gross and fine motor behavioural tests revealed that cerebral microinfarction does not result in motor impairments. With our microinfarct mouse model, we developed a novel method using a Python script to semi-automatically detect and register IVMs to specific brain regions using the Allen Mouse Brain Atlas (version 3). This registration method may further be used to quantify and localize the total number of IVMs lodged throughout the motor cortex region in order to determine if IVM load impacts motor function. Furthermore, we now have a semi-automated method for identifying histological markers such as EB dye. This software will allow us to continue identifying additional histological markers in a timely manner (i.e. Hematoxylin and Eosin stain or Prussian blue). Although other preclinical microinfarct models assessed cognitive deficits or motor impairments by using non-sensitive tests, future work with our model can incorporate both cognitive and motor tasks to determine the full range of impairments that may occur post-IVM surgery. Moreover, we can further align our microinfarct mouse model with how microinfarction occurs throughout humans by including factors such as age, pre-existing stroke conditions or inducing a focal ischemic stroke post-IVM injection to determine the impact of microinfarction on both the brain and behaviour. Despite cortical microinfarcts having many unanswered questions, improving our understanding of the pathogenesis and consequences of these small lesions on brain structure and function would be a step closer to aligning preclinical models to clinical work.

REFERENCES

1. Smith, E. E., Saposnik, G., Biessels, G. J., Doubal, F. N., Fornage, M., Gorelick, P. B., Greenberg, S. M., Higashida, R. T., Kasner, S. E., & Seshadri, S. (2017). Prevention of stroke in patients with silent cerebrovascular disease: A scientific statement for healthcare professionals from the American Heart Association/American Stroke Association. *Stroke, 48*(2), e44–e71.
2. Smith, E. E., Schneider, J. A., Wardlaw, J. M., & Greenberg, S. M. (2012). Cerebral microinfarcts: The invisible lesions. *The Lancet Neurology, 11*(3), 272–282.
3. Auriel, E. Westover, M. B., Bianchi, M. T., Reijmer, Y., Martinez-Ramirez, S., Ni, J., … Greenberg, S. M. (2015). Estimating total cerebral microinfarct burden from diffusion-weighted imaging. *Stroke, 46*(8), 2129-2135.
4. van Veluw, S. J., Shih, A. Y., Smith, E. E., Chen, C., Schneider, J. A., Wardlaw, J. M., Greenberg, S. M., & Biessels, G. J. (2017). Detection, risk factors, and functional consequences of cerebral microinfarcts. *Lancet Neurol. 16*(9), 730-740.
5. Wang, Z., Van Veluw, S. J., Wong, A., Liu, W., Shi, L., Yang, J., Xiong, Y., Lau, A., Biessels, G. J., & Mok, V. C. T. (2016). Risk Factors and Cognitive Relevance of Cortical Cerebral Microinfarcts in Patients with Ischemic Stroke or Transient Ischemic Attack. *Stroke, 47*(10), 2450–2455.
6. Sagnier, S., Okubo, G., Catheline, G., Munsch, F., Bigourdan, A., Debruxelles, S., Poli, M., Olindo, S., Renou, P., Rouanet, F., Dousset, V., Tourdias, T., & Sibon, I. (2019). Chronic Cortical Cerebral Microinfarcts Slow Down Cognitive Recovery after Acute Ischemic Stroke. *Stroke, 50*(6), 1430–1436.
7. Bernick, C., Kuller, L., Dulberg, C., Longstreth Jr, W. T., Manolio, T., Beauchamp, N., & Price, T., Cardiovascular Health Study Collaborative Research Group. (2001). Silent MRI infarcts and the risk of future stroke: the cardiovascular health study. *Neurology, 57*(7), 1222-1229.
8. Gupta, A., Giambrone, A. E., Gialdini, G., Finn, C., Delgado, D., Gutierrez, J., … Kamel, H. (2016). Silent Brain Infarction and Risk of Future Stroke: A Systematic Review and Meta-Analysis. *Stroke, 47*(3), 719–725.

9. Brundel, M., De Bresser, J., Van Dillen, J. J., Kappelle, L. J., & Biessels, G. J. (2012). Cerebral microinfarcts: A systematic review of neuropathological studies. *Journal of Cerebral Blood Flow and Metabolism, 32*(3), 425–436.
10. Suter, O. C., Sunthorn, T., Kraftsik, R., Straubel, J., Darekar, P., Khalili, K., & Miklossy, J. (2002). Cerebral hypoperfusion generates cortical watershed microinfarcts in Alzheimer disease. *Stroke, 33*(8), 1986–1992.
11. Olichney, J. M., Hansen, L. A., Hofstetter, C. R., Grundman, M., Katzman, R., & Thal, L. J. (1995). Cerebral infarction in Alzheimer's disease is associated with severe amyloid angiopathy and hypertension. *Arch Neurol. 52*(7), 702-708.
12. Soontornniyomkij, V., Lynch, M. D., Mermash, S., Pomakian, J., Badkoobehi, H., Clare, R., & Vinters, H. V. (2010). Cerebral microinfarcts associated with severe cerebral β-amyloid angiopathy. *Brain Pathology, 20*(2), 459–467.
13. Wang, M., Iliff, J. J., Liao, Y., Chen, M. J., Shinseki, M. S., Venkataraman, A., Cheung, J., Wang, W., & Nedergaard, M. (2012). Cognitive deficits and delayed neuronal loss in a mouse model of multiple microinfarcts. *Journal of Neuroscience*, 32(50), 17948–17960.
14. Summers, P. M., Hartmann, D. A., Hui, E. S., Nie, X., Deardorff, R. L., McKinnon, E. T., Helpern, J. A., Jensen, J. H., & Shih, A. Y. (2017). Functional deficits induced by cortical microinfarcts. *Journal of Cerebral Blood Flow and Metabolism, 37*(11), 3599–3614.
15. Arvanitakis, Z., Leurgans, S. E., Barnes, L. L., Bennett, D. A., & Schneider, J. A. (2011). Microinfarct pathology, dementia, and cognitive systems. *Stroke, 42*(3), 722–727.
16. Kimberly, W. T., Gilson, A., Rost, N. S., Rosand, J., Viswanathan, A., Smith, E. E., & Greenberg, S. M. (2009). Silent ischemic infarcts are associated with hemorrhage burden in cerebral amyloid angiopathy. *Neurology, 72*(14), 1230–1235.
17. Case, N. F., Charlton, A., Zwiers, A., Batool, S., McCreary, C. R., Hogan, D. B., Ismail, Z., Zerna, C., Coutts, S. B., Frayne, R., Goodyear, B., Haffenden, A., & Smith, E. E. (2016). Cerebral Amyloid Angiopathy is Associated with Executive Dysfunction and Mild Cognitive Impairment. *Stroke, 47*(8), 2010–2016.
18. Charidimou, A., Boulouis, G., Gurol, M. E., Ayata, C., Bacskai, B. J., Frosch, M. P., Viswanathan, A., & Greenberg, S. M. (2017). Emerging concepts in sporadic cerebral amyloid angiopathy. *Brain, 140*(7), 1829–1850.

19. Xiong, L., Van Veluw, S. J., Bounemia, N., Charidimou, A., Pasi, M., Boulouis, G., Reijmer, Y. D., Giese, A. K., Davidsdottir, S., Fotiadis, P., Valenti, R., Riley, G., Schwab, K., Gurol, E. M., Biffi, A., Greenberg, S. M., & Viswanathan, A. (2018). Cerebral cortical microinfarcts on magnetic resonance imaging and their association with cognition in cerebral amyloid angiopathy. *Stroke, 49*(10), 2330–2336.
20. Freeze, W. M., Bacskai, B. J., Frosch, M. P., Jacobs, H. I. L., Backes, W. H., Greenberg, S. M., & van Veluw, S. J. (2019). Blood-brain barrier leakage and microvascular lesions in cerebral amyloid angiopathy. *Stroke, 50*(2), 328-335.
21. Arvanitakis, Z., Capuano, A. W., Leurgans, S. E., Buchman, A. S., Bennett, D. A., & Schneider, J. A. (2017). The relationship of cerebral vessel pathology to brain microinfarcts. *Brain Pathol., 27*(1), 77-85.
22. Kapasi, A., & Schneider, J. A. (2016). Vascular contributions to cognitive impairment, clinical Alzheimer's disease, and dementia in older persons. *Biochimica et Biophysica Acta - Molecular Basis of Disease, 1862*(5), 878–886.
23. Zheng, L., Vinters, H. V., Mack, W. J., Zarow, C., Ellis, W. G., & Chui, H. C. (2013). Cerebral atherosclerosis is associated with cystic infarcts and microinfarcts but not alzheimer pathologic changes. *Stroke, 44*(10), 2835–2841.
24. Westover, M. B., Bianchi, M. T., Yang, C., Schneider, J. A., & Greenberg, S. M. (2013). Estimating cerebral microinfarct burden from autopsy samples. *Neurology, 80*(15), 1365–1369.
25. Vinters, H. V., Ellis, W. G,, Zarow, C., Zaias, B. W., Jagust, W. J., Mack, W. J., & Chui, H. C. (2000). Neuropathologic substrates of ischemic vascular dementia. *J Neuropathol Exp Neurol, 59*(11), 931–945.
26. Van Dalen, J. W., Scuric, E. E. M., Van Veluw, S. J., Caan, M. W. A., Nederveen, A. J., Biessels, G. J., Van Gool, W. A., & Richard, E. (2015). Cortical microinfarcts detected in vivo on 3 tesla MRI: Clinical and radiological correlates. *Stroke, 46*(1), 255–257.
27. Lauer, A., van Veluw, S. J., William, C. M., Charidimou, A., Roongpiboonsopit, D., Vashkevich, A., Ayres, A., Martinez-Ramirez, S., Gurol, E. M., Biessels, G. J., Frosch, M., Greenberg, S. M., & Viswanathan, A. (2016). Microbleeds on MRI are associated with microinfarcts on autopsy in cerebral amyloid angiopathy. *Neurology, 87*(14), 1488–1492.

28. Yilmazer-Hanke, D., Mayer, T., Müller, H.-P., Neugebauer, H., Abaei, A., Scheuerle, A., … Rasche, V. (2020). Histological correlates of postmortem ultra-high-resolution single-section MRI in cortical cerebral microinfarcts. *Acta Neuropathologica Communications*, *8*(1), 1-18.
29. Patel, N., Banahan, C., Janus, J., Horsfield, M. A., Cox, A., Li, X., Cappellugola, L., Colman, J., Egan, V., Garrard, P., & Chung, E. M. L. (2019). Perioperative cerebral microbleeds after adult cardiac surgery. *Stroke*, *50*(2), 336–343.
30. Shi, Z. S., Duckwiler, G. R., Jahan, R., Tateshima, S., Gonzalez, N. R., Szeder, V., Saver, J. L., Kim, D., Ali, L. K., Starkman, S., Vespa, P. M., Salamon, N., Villablanca, J. P., Viñuela, F., Feng, L., Loh, Y., & Liebeskind, D. S. (2015). New cerebral microbleeds after mechanical thrombectomy for large-vessel occlusion strokes. *Medicine, 94*(47), e2180.
31. Yan, S., Chen, Y., Zhang, X., Liebeskind, D. S., & Lou, M. (2014). New microbleeds after thrombolysis: contiguous thin-slice 3T MRI. *Medicine, 93*(20), e99.
32. Sonnen, J. A,, Larson, E. B., Crane, P. K., Haneuse, S., Li, G., Schellenberg, G. D., Craft, S., Leverenz, J. B., & Montine, T. J. (2007). Pathological correlates of dementia in a longitudinal, population-based sample of aging. *Ann Neurol, 62*(4), 406–413.
33. Haglund, M., Passant, U., Sjöbeck, M., Ghebremedhin, E., & Englund, E. (2006). Cerebral amyloid angiopathy and cortical microinfarcts as putative substrates of vascular dementia. *Int J Geriatr Psychiatry, 21*(7), 681–687.
34. Schneider, J. A., Wilson, R. S., Cochran, E. J., Bienias, J. L., Arnold, S. E., Evans, D. A., & Bennett, D. A. (2003). Relation of cerebral infarctions to dementia and cognitive function in older persons. *Neurology, 60*(7), 1082–1088.
35. Kapasi, A., Leurgans, S. E., James, B. D., Boyle, P. A., Arvanitakis, Z., Nag, S., Bennett. D. A., & Schneider, J. A. (2018). Watershed microinfarct pathology and cognition in older persons. *Neurobiology of Aging, 70*, 10–17.
36. Buchman, A. S., Yu, L., Boyle, P. A., Levine, S. R., Nag, S., Schneider, J. A., & Bennett, D. A. (2013). Microvascular brain pathology and late-life motor impairment. *Neurology, 80*(8), 712–718.
37. Louis, E. D., & Bennett, D. A. (2007). Mild Parkinsonian signs: an overview of an emerging concept. *Mov. Disord., 22*(12), 1681-1688.

38. Zheng, J. J. J., Delbaere, K., Close, J. C. T., Sachdev, P. S., & Lord, S. R. (2011). Impact of white matter lesions on physical functioning and fall risk in older people. *Stroke, 42*(7), 2086-2090.
39. Buchman, A. S., Leurgans, S. E., Boyle, P. A., Schneider, J. A., Arnold, S. E., & Bennett, D. A. (2011). Combinations of motor measures more strongly predict adverse health outcomes in old age: the rush memory and aging project, a community-based cohort study. *BMC Med, 9*, 42.
40. Shih, A. Y., Hyacinth, H. I., Hartmann, D. A., & van Veluw, S. J. (2018). Rodent models of cerebral microinfarct and microhemorrhage. *Stroke, 49*(3), 803-810.
41. Shih, A. Y., Blinder, P., Tsai, P. S., Friedman, B., Stanley, G., Lyden, P. D., & Kleinfeld, D. (2013). The smallest stroke: occlusion of one penetrating vessel leads to infarction and a cognitive deficit. *Nature Neuroscience, 16*(1), 55-63.
42. Sigler, A., Goroshkov, A., & Murphy, T. H. (2008). Hardware and methodology for targeting single brain arterioles for photothrombotic stroke on an upright microscope. *Journal of Neuroscience Methods, 170*(1), 35-44.
43. Watts, L. T., Zheng, W., Garling, R. J., Frohlich, V. C., & Lechleiter, J. D. (2015). Rose Bengal photothrombosis by confocal optical imaging *in vivo*: a model of single vessel stroke. *Journal of Visualized Experiments, 2015* (100), e52794.
44. Taylor, Z. J., Hui, E. S., Watson, A. N., Nie, X., Deardorff, R. L., Jensen, J. H., Helpern, J. A., & Shih, A. Y. (2016). Microvascular basis for growth of small infarcts following occlusion of single penetrating arterioles in mouse cortex. *Journal of Cerebral Blood Flow & Metabolism, 36*(8), 1357-1373.
45. Macrae, I. M. (2011). Preclinical stroke research – advantages and disadvantages of the most common rodent models of focal ischemia. *British Journal of Pharmacology, 164*(4), 1062-1078.
46. Holland, P. R., Searcy, J. L., Salvadores, N., Scullion, G., Chen, G., Lawson, G., … Horsburgh, K. (2015). Gliovascular Disruption and Cognitive Deficits in a Mouse Model with Features of Small Vessel Disease. *Journal of Cerebral Blood Flow & Metabolism*, *35*(6), 1005–1014.

47. Washida, K., Hattori, Y. & Ihara, M. (2019). Animal models of chronic cerebral hypoperfusion: from mouse to primate. *International Journal of Molecular Sciences, 20*(24), e6176.
48. Rapp, J. H., Pan, X. M., Neumann, M., Hong, M., Hollenbeck, K., & Liu, J. (2008) Microemboli composed of cholesterol crystals disrupt the blood-brain barrier and reduce cognition. *Stroke, 39*(8), 2354– 2361.
49. Silasi, G., She, J., Boyd, J. D., Xue, S., & Murphy, T. H. (2015). A mouse model of small-vessel disease that produces brain-wide-identified microocclusions and regionally selective neuronal injury. *Journal of Cerebral Blood Flow and Metabolism*, *35*(5), 734–738.
50. Balbi, M., Vanni, M. P., Vega, M. J., Silasi, G., Sekino, Y., Boyd, J. D., LeDue, J. M., & Murphy, T. H. (2019). Longitudinal monitoring of mesoscopic cortical activity in a mouse model of microinfarcts reveals dissociations with behavioral and motor function. *Journal of Cerebral Blood Flow & Metabolism, 39*(8), 1486-1500.
51. Bell, A. H., Miller, S. L., Castillo-Melendez, M., & Malhotra, A. (2020). The neurovascular unit: effects of brain insults during the perinatal period. *Frontiers in Neurosciences, 13*(1452), 1-19.
52. Sandoval, K. E., & Witt, K. A. (2008). Blood-brain barrier tight junction permeability and ischemic stroke. *Neurobiology of Disease, 32*(2), 200-219.
53. Kolb, B., & Whishaw, I. Q. (2014). *An introduction to brain and behavior* (4th ed.) (pp.174-175). New York: Worth Publishers.
54. Hone, E. A., Hu, H., Sprowls, S. A., Farooqi, I., Grasmick, K., Lockman, P. R., Simpkins, J. W., & Ren, X. (2018). Biphasic blood-brain barrier openings after stroke. *Neurological Disorders and Stroke International, 1*(2), 1011.
55. Abbott, N. J., Ronnback, L., and Hansson, E. (2006). Astrocyte-endothelial interactions at the blood-brain barrier. *Nat. Rev. Neurosci.7*, 41–53.
56. Carmignoto, G., & Gómez-Gonzalo, M. (2010). The contribution of astrocyte signalling to neurovascular coupling. *Brain Research Reviews, 63*(1-2), 138-148.
57. Persidsky, Y., Ramirez, S. H., Haorah, J., & Kanmogne, G. D. (2006). Blood-brain barrier : structural components and function under physiologic and pathologic conditions. *Journal of Neuroimmune Pharmacology, 1*(3), 223-236.

58. Zhang, W., Zhu, L., An, C., Wang, R., Yang, L., Yu, W., Li, P., & Gao, Y. (2020). The blood-brain barrier in ischemic injury – Disruption and repair. *Brain Hemorrhages*, Article in Press.
59. Daneman, R., & Prat, A. (2015). The blood-brain barrier. *Cold Spring Harb Perspect Biol, 7*, a020412.
60. Knowland, D., Arac, A., Sekiguchi, K., Hsu, M., Lutz, S., Perrino, J., Steinberg, G., Barres, B., Nimmerjahn, A., & Agalliu, D. (2014). Stepwsie recruitment of transcellular and paracellular pathways underlies blood-brain barrier breakdown in stroke. *Neuron, 82*(3), 603-617.
61. Jiang, X., Andjelkovic, A. V., Zhu, L., Yang, T., Bennett, M., Chen, J., Keep, R. F., & Shi, Y. (2018). Blood-brain barrier dysfunction and recovery after ischemic stroke. *Progress in neurobiology, 163-164*, 144–171.
62. Giraud, M., Cho, T. H., Nighoghossian, N., Maucort-Boulch, D., Deiana, G., Ostergaard, I., Baron, J. C., Fiehler, J., Pedraza, S., Derex, L., & Berthezène, Y. (2015). Early blood brain barrier changes in acute ischemic stroke: A sequential MRI study. *J Neuroimaging, 25*(6), 959-963.
63. Krueger, M., Bechmann, I., Immig, K., Reichenbach, A., Härtig, W., & Michalski, D. (2015). Blood—Brain Barrier Breakdown Involves Four Distinct Stages of Vascular Damage in Various Models of Experimental Focal Cerebral Ischemia. *Journal of Cerebral Blood Flow & Metabolism*, *35*(2), 292–303.
64. Kidd, G. A., Hong, H., Majid, A., Kaufman, D. I., & Chen, A. F. (2005). Inhibition of brain GTP cyclohydrolase I and tetrahydrobiopterin attenuates cerebral infarction via reducing inducible NO synthase and peroxynitrite in ischemic stroke. *Stroke, 36*(12), 2705-2711.
65. Kuntz, M., Mysiorek, C., Petrault, O., Petrault, M., Uzbekov, R., Bordet R., Fenart, L., Cecchelli, R., & Bérézowski, V. (2014). Stroke-induced brain parenchymal injury drives blood-brain barrier early leakage kinetics: a combined in vivo/in vitro study. *J Cereb Blood Flow Metab., 34*(1), 95-107.
66. Sadeghian, H., Lacoste, B., Qin, T., Toussay, X., Rosa, R., Oka, F., . . . Ayata, C. (2018). Spreading depolarizations trigger caveolin-1-dependent endothelial transcytosis. *Annals of Neurology, 84*(3), 409-423.

67. Ben-Zvi, A., Lacoste, B., Kur, E., Andreone, B. J., Mayshar, Y., Yan, H., & Gu, C. (2014). Mfsd2a is critical for the formation and function of the blood-brain barrier. *Nature, 509*(7501), 507–511.
68. Kipnis, J. (2016). Multifaceted interactions between adaptive immunity and the central nervous system. *Science, 353*(6301), 766-771.
69. Planas, A. M. (2018). Role of Immune Cells Migrating to the Ischemic Brain. *Stroke, 49*(9), 2261-2267.
70. Lubart, A., Benbenishty, A., Har-Gil, H., Laufer, H., Gedalyahu, A., Assaf, Y., & Blinder, P. (2018). Cortical microinfarcts caused by single penetrating vessel occlusion lead to widespread reorganization across the entire brain in a CX3CR1 dependent manner. *Preprint submitted to Elsevier.*
71. Hartmann, D. A., Hyacinth, H. I., Liao, F.-F., & Shih, A. Y. (2017). Does pathology of small venules contribute to cerebral microinfarcts and dementia? *Journal of Neurochemistry*, *144*(5), 517–526.
72. Coelho-Santos, V., & Shih, A. Y. (2019). Postnatal development of cerebrovascular structure and the neurogliovascular unit. *WIREs Developmental Biology*, *9*(2), e363.
73. El-Bouri, W. K, & Payne, S. J. (2016). A statistical model of the penetrating arterioles and venules in the human cerebral cortex. *Microcirculation*, *23*(7), 580-590.
74. Corbett, D., Carmichael, S. T., Murphy, T. H., Jones, T. A., Schwab, M. E., Jolkkonen, J., … Joy, M. T. (2017). Enhancing the alignment of the preclinical and clinical stroke recovery research pipeline: Consensus-based core recommendations from the Stroke Recovery and Rehabilitation Roundtable translational working group. *International Journal of Stroke*, *12*(5), 462–471.
75. Denk, W., & Horstmann, H. (2004). Serial Block-Face Scanning Electron Microscopy to Reconstruct Three-Dimensional Tissue Nanostructure. PLoS Biology, 2(11), e329.
76. Saunders, N. R., Dziegielewska, K. M., Møllgård, K., & Habgood, M. D. (2015). Markers for blood-brain barrier integrity: how appropriate is Evans blue in the twenty-first century and what are the alternatives?. *Frontiers in neuroscience, 9*, 385, 1-16.
77. Sommer, C., Straehle, C., Kothe, U., & Hamprecht, F. A. (2011). Ilastik: Interactive learning and segmentation toolkit. 2011 IEEE International Symposium on Biomedical Imaging: From Nano to Macro.

78. ANTs. (n.d.). Retrieved from http://stnava.github.io/ANTs/
79. Ardesch, D. J., Balbi, M., & Murphy, T. H. (2017). Automated touch sensing in the mouse tapered beam test using Raspberry Pi. *Journal of Neuroscience Methods, 291,* 221-226.
80. Remington, L. A. (2011). Chapter 11 – Orbital blood supply. *Clinical Anatomy and Physiology of the Visual System* (3rd edition, pp. 202-217). Butterworth-Heinemann.
81. Warach, S. (2004). Evidence of Reperfusion Injury, Exacerbated by Thrombolytic Therapy, in Human Focal Brain Ischemia Using a Novel Imaging Marker of Early Blood-Brain Barrier Disruption. *Stroke, 35*(11_suppl_1), 2659-2661.
82. Merali, Z., Huang, K., Mikulis, D., Silver, F., & Kassner, A. (2017). Evolution of blood-brain-barrier permeability after acute ischemic stroke. *Plos One, 12*(2), e0171558.
83. Heye, A. K., Culling, R. D., Hernández, M. D., Thrippleton, M. J., & Wardlaw, J. M. (2014). Assessment of blood–brain barrier disruption using dynamic contrast-enhanced MRI. A systematic review. *NeuroImage: Clinical, 6,* 262-274.
84. Kassner, A., & Merali, Z. (2015). Assessment of Blood–Brain Barrier Disruption in Stroke. *Stroke, 46*(11), 3310-3315. doi:10.1161/strokeaha.115.008861
85. Zhang, J. H., Badaut, J., Tang, J., Obenaus, A., Hartman, R., & Pearce, W. J. (2012). The vascular neural network—a new paradigm in stroke pathophysiology. *Nature Reviews Neurology, 8*(12), 711-716.
86. Lin, R., Cai, J., Nathan, C., Wei, X., Schleidt, S., Rosenwasser, R., & Iacovitti, L. (2015). Neurogenesis is enhanced by stroke in multiple new stem cell niches along the ventricular system at sites of high BBB permeability. *Neurobiology of Disease, 74,* 229-239.
87. Gotts, J. E., & Chesselet, M. (2005). Vascular changes in the subventricular zone after distal cortical lesions. *Experimental Neurology, 194*(1), 139-150.
88. Zhu, Y., Shwe, Y., Du, R., Chen, Y., Shen, F. X., Young, W. L., & Yang, G. Y. (2006). Effects of angiopoietin-1 on vascular endothelial growth factor-induced angiogenesis in the mouse brain. *Brain Edema XIII Acta Neurochirurgica Supplementum, 96,* 438-443.
89. Zhu, Y., Lee, C., Shen, F., Du, R., Young, W. L., & Yang, G. (2005). Angiopoietin-2 Facilitates Vascular Endothelial Growth Factor-Induced Angiogenesis in the Mature Mouse Brain. *Stroke, 36*(7), 1533-1537.
90. Jaffer, H., Adjei, I. M., & Labhasetwar, V. (2013). Optical imaging to map blood-brain barrier leakage. *Scientific Reports, 3*(1), 1-8.

91. Reeson, P., Tennant, K. A., Gerrow, K., Wang, J., Novak, S. W., Thompson, K., . . . Brown, C. E. (2015). Delayed Inhibition of VEGF Signaling after Stroke Attenuates Blood-Brain Barrier Breakdown and Improves Functional Recovery in a Comorbidity-Dependent Manner. *Journal of Neuroscience*, *35*(13), 5128-5143.
92. Villaseñor, R., Kuennecke, B., Ozmen, L., Ammann, M., Kugler, C., Grüninger, F., . . . Collin, L. (2017). Region-specific permeability of the blood–brain barrier upon pericyte loss. *Journal of Cerebral Blood Flow & Metabolism, 37*(12), 3683-3694.
93. Wang, H., Kuo, E. Y., & Lai, T. W. (2018). Vascular delivery of intraperitoneal Evans blue dye into the blood–brain barrier-intact and disrupted rat brains. *NeuroReport, 29*(11), 924-931.
94. Bussey, T. J., Saksida, L. M., & Rothblat, L. A. (2001). Discrimination of computer-graphic stimuli by mice: A method for the behavioral characterization of transgenic and gene-knockout models. *Behavioral Neuroscience, 115*(4), 957–960.
95. Silasi, G., Boyd, J. D., Ledue, J., & Murphy, T. H. (2013). Improved methods for chronic light-based motor mapping in mice: automated movement tracking with accelerometers, and chronic EEG recording in a bilateral thin-skull preparation. *Frontiers in Neural Circuits, 7*, 1-10.
96. Silasi, G., Xiao, D., Vanni, M. P., Chen, A. C., & Murphy, T. H. (2016). Intact skull chronic windows for mesoscopic wide-field imaging in awake mice. *Journal of Neuroscience Methods*, *267*, 141–149.

APPENDIX A – Animal Log Sheet for Experiment 1 and Experiment 2

Table 1. The number of mice that were included in each experiment with their sex, and genotype. Excluded animals and reasons are provided with mortality rate for each experiment.

		Number of Mice	Sex (M= male; F= female)	Genotype			Excluded	Mortality Rate (%)
				C57BL6	ArcTrap	Thy1-ChR2-YFP		
Experiment 1	Day 1	10	M= 2	-	-	2	3 mice were excluded from the EB analysis due to improper EB injections (Day 1= 1 ArcTrap F; Day 7= 1 Thy1-ChR2-YFP M; Day 14= 1 Thy1-ChR2-YFP M)	9.52% (4 mice died)
			F= 8	3	2	3		
	Day 3	12	M= 11	-	2	9		
			F= 1	-	-	1		
	Day 7	6	M= 3	-	-	3		
			F= 3	-	-	3		
	Day 14	4	M= 4	-	-	4		
			F= 0	-	-	-		
	Day 21	6	M= 3	-	-	3		
			F= 3	-	-	3		
Experiment 2	Sham	14	M= 10	-	-	10	2 mice were excluded from behavioural testing because they were unable to successfully reach for a pellet in the SPRT (1 F and 1 M Thy1-ChR2-YFP)	15.2% (5 mice died)
			F= 4	-	-	4		
	Microinfarct	14	M= 10	-	-	10		
			F= 4	-	-	4		

APPENDIX B – Supplemental Figures for Experiment 2

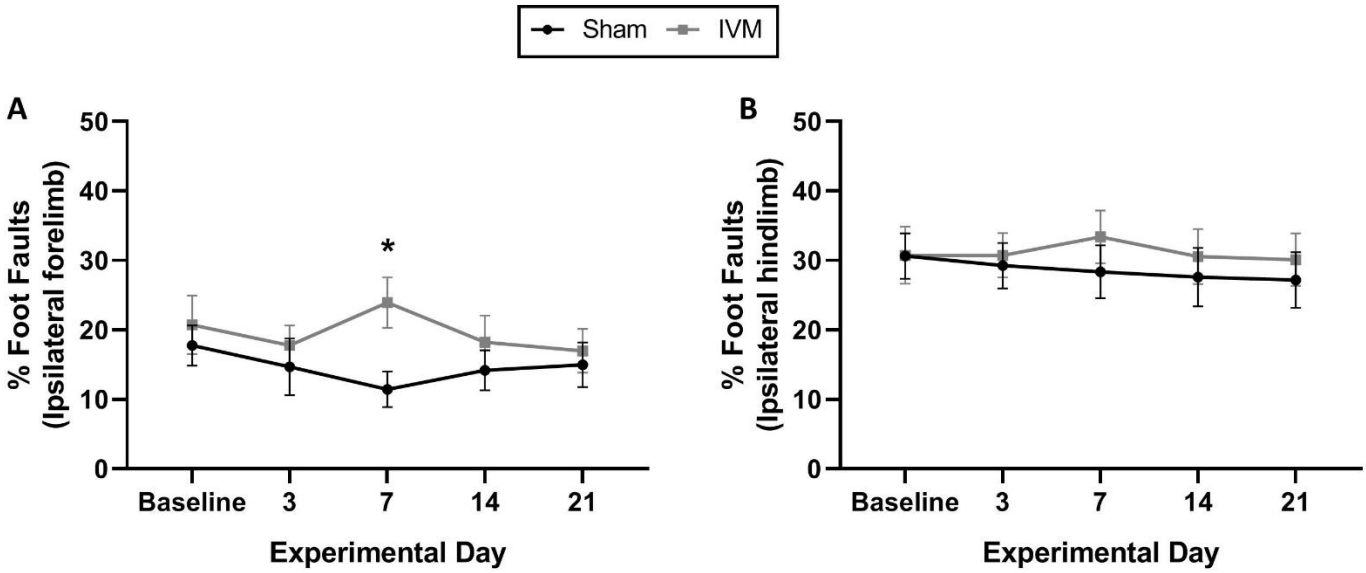

Figure 22. Tapered beam test before and after sham and IVM surgeries. (A) Percent foot faults for the ipsilateral forelimb. A significant group x time interaction (p=0.001) occurred 7 days following surgery (*p=0.034) where IVM mice had a significant increase in the percentage of foot faults using their ipsilateral forelimb when compared to sham mice. No time effects (p=0.828) or group effects (p=0.103) were detected during experimental days compared to baseline performance. (B) Percentage of foot faults for ipsilateral hindlimb (sham=14, IVM=14). No time effects (p=0.796), group x time interaction (p=0.893) or group effects (p=0.581) where observed for the percentage of foot faults made by the ipsilateral hindlimb. Values are presented as sample means ± SEM.

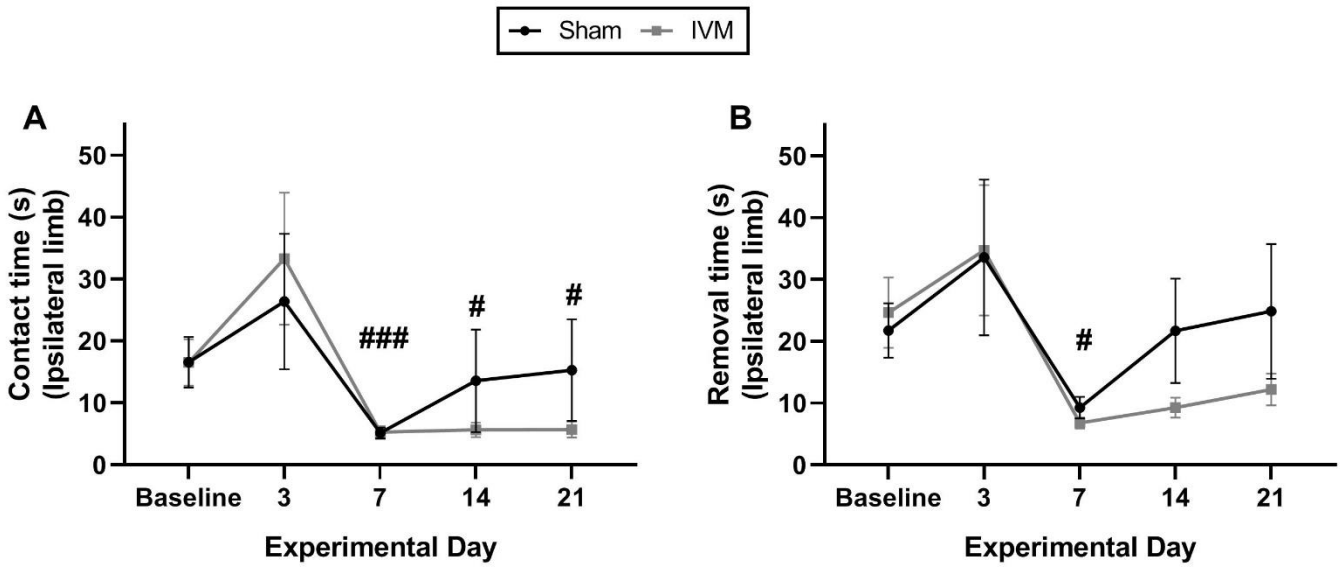

Figure 23. Adhesive removal test before and after sham and IVM surgeries. (A) Contact time made between the ipsilateral forelimb and adhesive tape. No group effects ($p=0.753$) or group x time interaction ($p=0.43$) were observed; however, an effect of time ($p=0.011$) occurred at days 7 (###$p<0.001$), 14 (#$p=0.028$) and 21 (#$p=0.012$) post-surgery. These time effects resulted in both groups of mice; particularly the IVM mice, contacting the tape at a faster rate when compared to baseline performance. (B) Removal time of the adhesive tape with the ipsilateral forelimb. No group effects ($p=0.585$) or group x time interaction ($p=0.317$) were observed; however, a time effect ($p=0.022$) occurred at day 7 post-surgery (#$p<0.001$; sham=14, IVM=14), where both groups of mice became faster at removing the tape from their ipsilateral paw. Values are presented as sample means ± SEM.

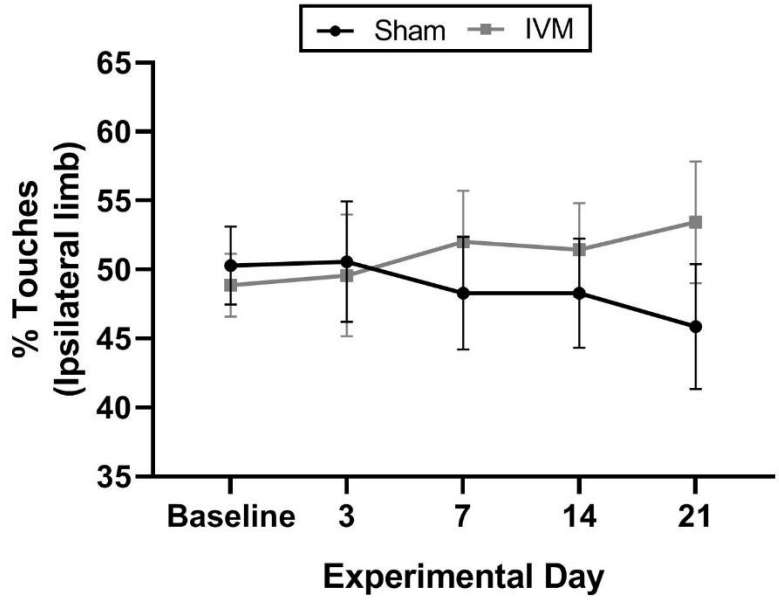

Figure 24. Spontaneous forelimb use in the cylinder test before and after sham and IVM surgeries. Percent touches made by the ipsilateral forelimb against the wall of the cylinder. No group effects (p=0.561), group x time interaction (p=0.415) or time effects (p=1) were observed across experimental days post-surgery (sham=14, IVM=14). Values are presented as sample means ± SEM.

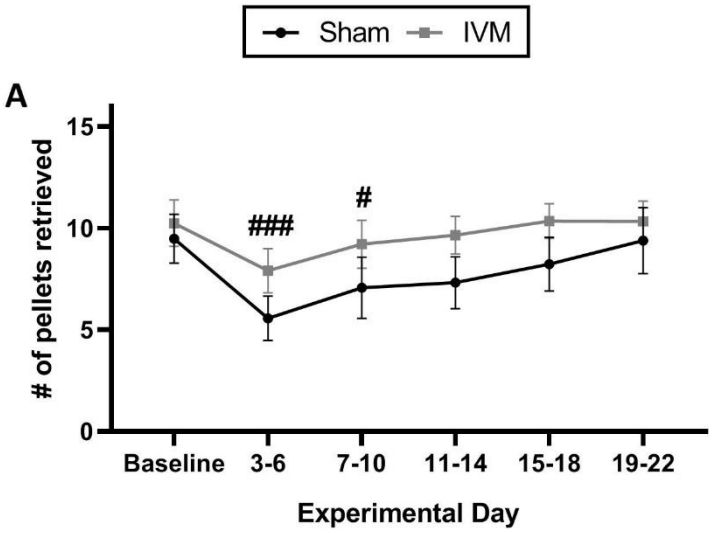
Sham
IVM
A
# of pellets retrieved
15
10
5
0
###
#
Baseline
3-6
7-10
11-14
15-18
19-22
Experimental Day

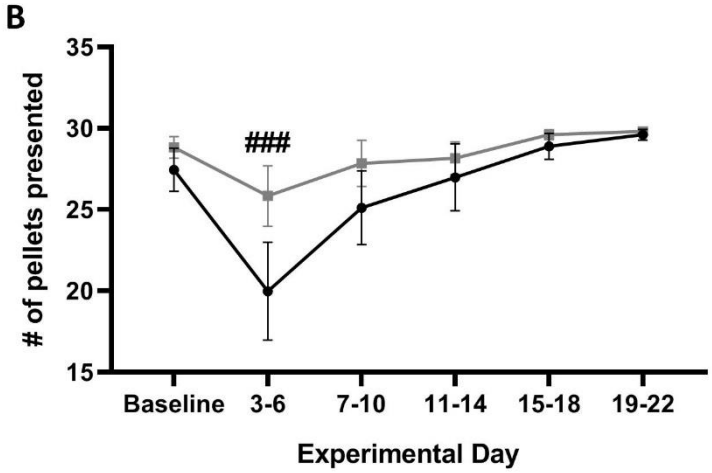
B
# of pellets presented
35
30
25
20
15
###
Baseline
3-6
7-10
11-14
15-18
19-22
Experimental Day

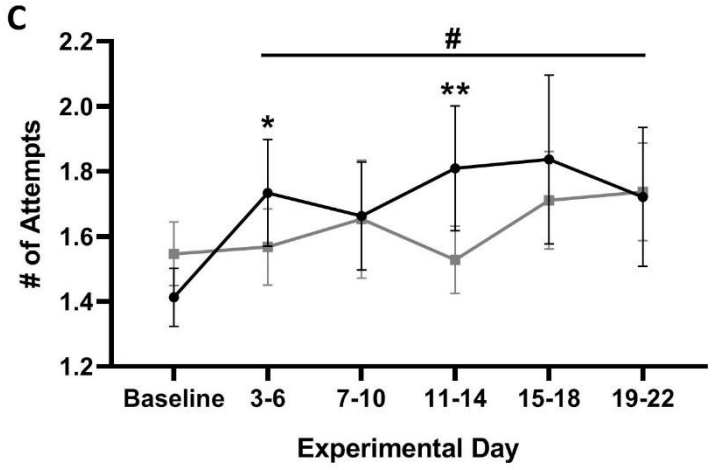
C
# of Attempts
2.2
2.0
1.8
1.6
1.4
1.2
#
*
**
Baseline
3-6
7-10
11-14
15-18
19-22
Experimental Day

Figure 25. Skilled forelimb reaching in the single pellet reaching task before and after sham and IVM surgeries. (A) The average number of successful pellets retrieved across experimental days for both sham (n=14) and IVM (n=14) mice. No group effects (p=0.353) or group x time interaction (p=0.798) were observed; however, time effects (p=0.009) occurred between bins 2 (days 3-6; ### p<0.001) and 3 (days 7-10; # p=0.025) when compared to baseline performance. These time effects occurred for both sham and IVM mice, where both groups retrieved less pellets within the first few days following surgery, followed by a slow increase in pellet retrieval within the following days. (B) The average number of pellets presented during each testing session for both groups across experimental days. No group effects (p=0.269) or group x time interaction (p=0.095) were detected; though a time effect (p<0.001) was observed throughout the second binned data (days 3-6; ### p<0.001) when compared to baseline data. This time effect signified a decrease in the number of pellets presented for both groups of mice, predominantly for the sham mice during the task. (C) The average number of attempts that were made prior to successfully grasping a pellet. There was a significant group x time interaction (p=0.059) between sham and IVM mice that occurred throughout bins 2 (days 3-6; * p=0.036) and 4 (days 11-14; ** p=0.007), where sham mice made more attempts in order to successfully grasp a pellet. A time effect (p=0.003) was further observed throughout all experimental days (# p<0.05; all binned data). This time effect further signified that the sham mice made more attempts to successfully retrieve a pellet across experimental days post-surgery. No group effects were observed (p=0.183).Values are presented as sample means ± SEM.

APPENDIX C – Cognitive Testing

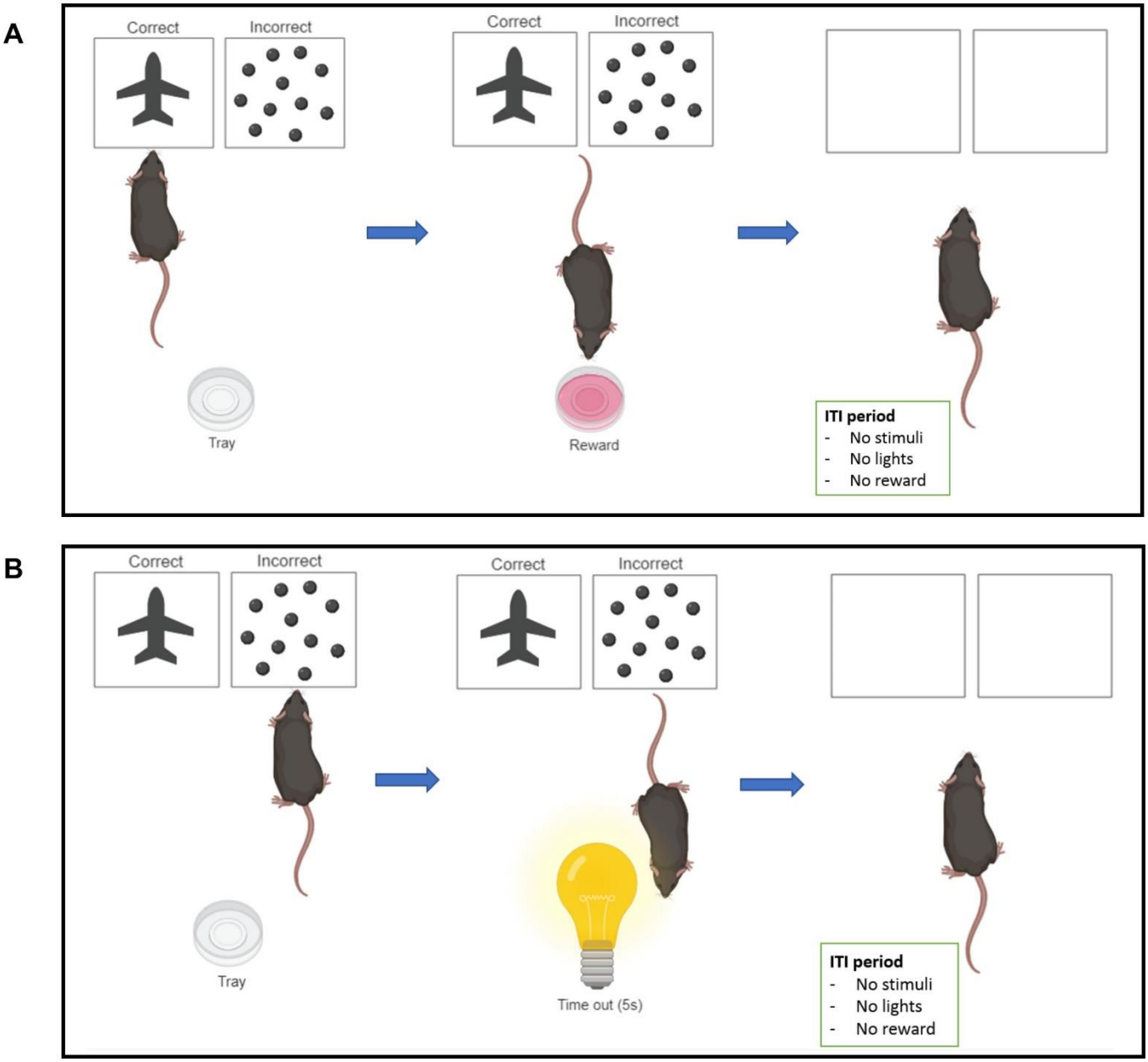

Figure 26. Cognitive testing using the Bussey-Saksida mouse touchscreen chamber [94]. Mice were trained to discriminate between two visual stimuli (i.e. plane and dots) displayed on the touchscreen for both pairwise discrimination (PD) and reversal tasks. (A) After the mouse nose pokes the correct visual stimuli a reward is given, followed by the mouse entering into an inter-trial interval period. (B) If the mouse nose pokes the incorrect stimuli, the animal enters into a time out period where the chamber becomes illuminated (5s). No reward is given if the incorrect stimuli is chosen.

To test for cognitive deficits post-cerebral microinfarction, a Bussey-Saksida mouse touch screen chamber [94] was used to test mice on and a paired-associated learning task. Mice were food deprived throughout the task and their body weight was maintained between 80-85% of their baseline weight. Once mice were habituated to the apparatus and training sessions were completed, the PD task began. A video display unit was placed at the front of the chamber allowing visual stimuli to be presented. Two images were presented at the same time; a correct and incorrect image, where mice had to learn to discriminate between the two visual stimuli. To initiate the task, mice had to put their head into a food well that was placed at the back of the chamber. When mice nose poked the correct visual stimuli, they were rewarded with a liquid reinforcer followed by an inter-trial interval period (ITI; 20 seconds; Figure 27A). If the mouse nose poked the incorrect visual stimuli, a time out session occurred for 5 seconds, where the chamber light turned on and no reward was given (Figure 27B). The mouse then entered into the ITI period, followed by a repeat of the same trial. When the mice reached performance criterion of 80% for 2 consecutive days, the task switched from the PD to the reversal task, in which the correct visual stimuli became the incorrect stimuli and vice versa. Following the baseline reversal task, all mice underwent the IVM surgery (Figure 3; n=4; mortality rate=20%). After a week of rest, the mice were retested on the PD and reversal tasks with a new set of visual stimuli.

A chi-squared test revealed that the PD (Figure 28A; p=0.600) and the reversal (Figure 28B; p=0.5990) survival curves were not significantly different from one another. IVM's did not affect the mice's ability to learn the PD and reversal tasks post-surgery. Multiple regression analyses were performed; however, only the right inter-trial interval (ITI) touches and correct touch latency data were significant. There was no indication that stroke affected the learning ability of the mice post-stroke. For correct touch latency, there was a significant decrease in latency (p=0.036) between PD and reversal tasks and a significant decrease between the two reversal tasks (Figure 28C; p=0.018). These results suggest that the mice have learned the tasks over time. During the pre-stroke training, mice made significantly more touches on the right screen during PD training than during reversal training (p=0.032), indicating that the mice have learned to not touch the screen during the ITI period (no reward given). The slight significant increase (p=0.032) in right ITI touches between pre- and post-stroke data for the reversal task may be due to the microsphere induced mage causing impulsive nose-poking (Figure 28D).

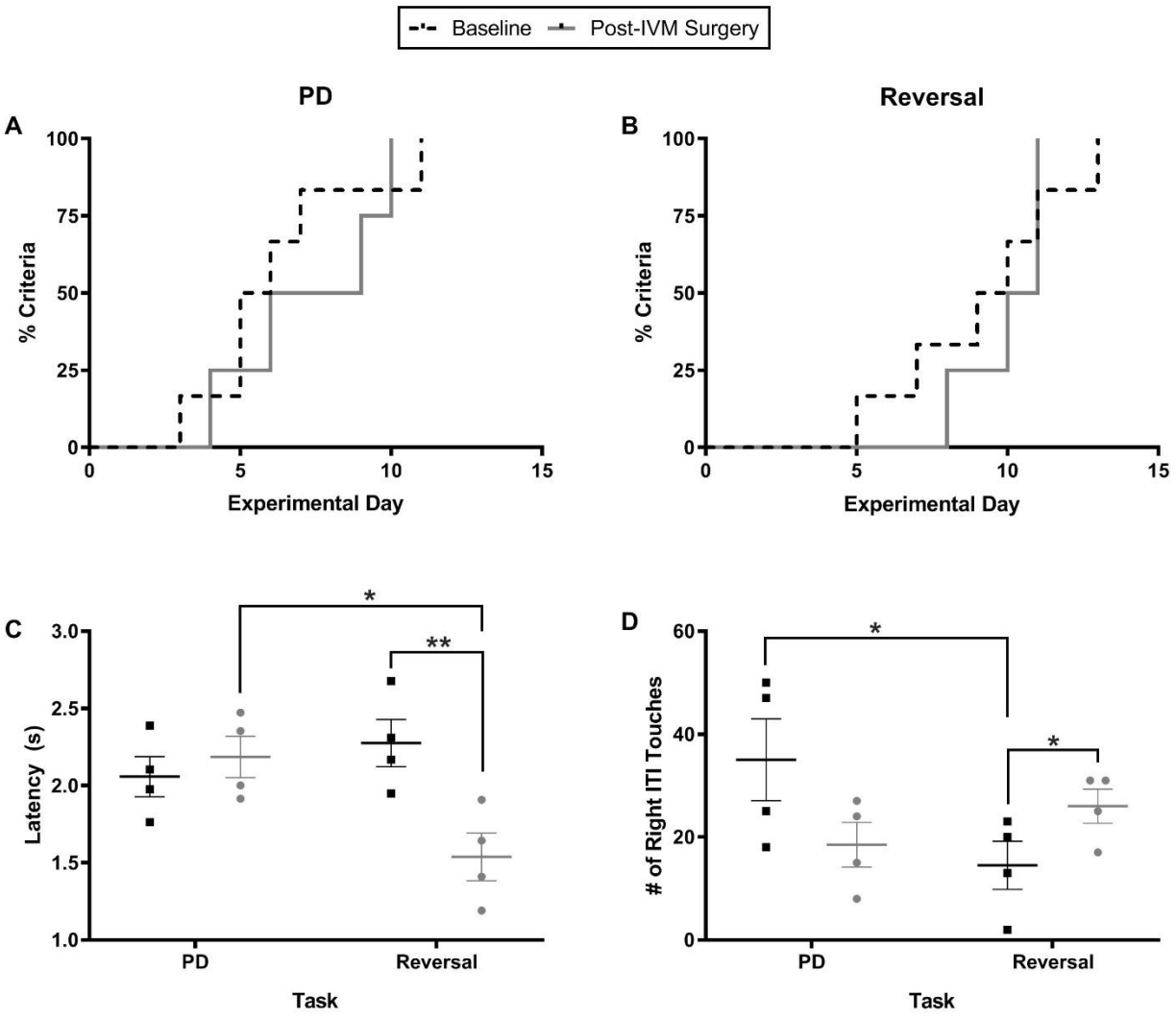

Figure 27. Cognitive testing of pairwise discrimination (PD) and reversal tasks before and after IVM surgery. (A-B) Learning curves for both PD and reversal tasks (baseline=black dashed line, post-IVM surgery=grey solid line). No significant difference between baseline and post-IVM learning curves was observed for the PD (p= 0.6004) and reversal (p=0.5990) tasks. (C) The correct touch latency for PD and reversal tasks before and after surgery (*p=0.036; **p=0.018). Overall, IVM mice became faster during the reversal task post-surgery when compared to the PD task and baseline performance during the reversal task. (D) The number of touches made on the right screen during inter-trial interval (ITI) periods (*p=0.032). IVM mice nose-poked the screen less over time; however an increase in the number of touches occurred during the last task (reversal) post-surgery. Values are presented as sample means ± SEM (n=4).

APPENDIX D – Motor Mapping and Laser Doppler Imaging (LDI)

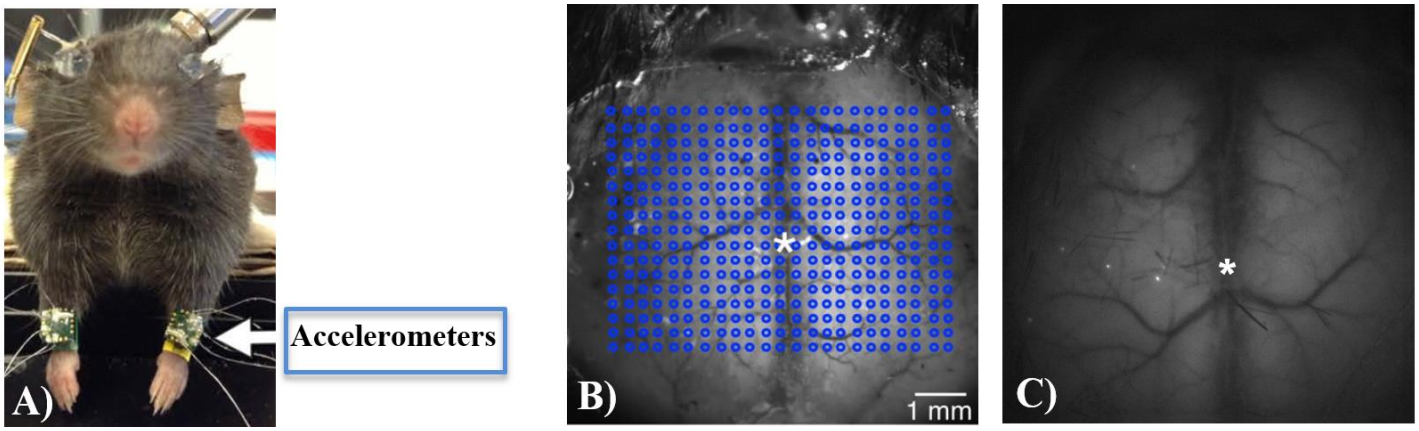

Figure 28. Motor mapping IVM mice set-up. (A-B) Setup for motor mapping with a grid of stimulation sites [95] targeting cortical points through a chronic cranial window [96]. Each stimulation site was visited in a random order by a collimated laser beam (*=Bregma). (C) Blue light fluorescence image of the cranial window showing the IVMs lodged within the brain vasculature.

Thy1-ChR2-YFP mice were anaesthetized with ketamine and xylazine, where evoked movements were quantified with accelerometers attached to each forelimb (Figure 29A) while they received an array of point stimulations (470 nm laser; Figure 29B) [95] over both hemispheres (Figure 30A). Dorsal images were taking for each mouse showing the injected fluorescent microspheres through the cranial window that were lodged within the brain vasculature (Figure 29C). Bilateral maps of forelimb movement amplitude were generated 3 days after the cranial window implant [96] (Baseline). Once baseline maps were completed, all mice underwent the IVM surgery (n=4; mortality rate=43%), followed by bilateral maps being generated at days 3, 7, 14 and 21 days post-IVM surgery. Animals were inject with ketamine/xylazine and blood flow was imaged bilaterally using a scanning laser Doppler imaging system (Moor Instruments) at the same time points as motor maps were generated. Using a two way-repeated measures ANOVA, there were no significant effects that were observed for motor map organization (Figure 30B; $p=0.9329$) or motor output (Figure 30C; $p=0.8077$).

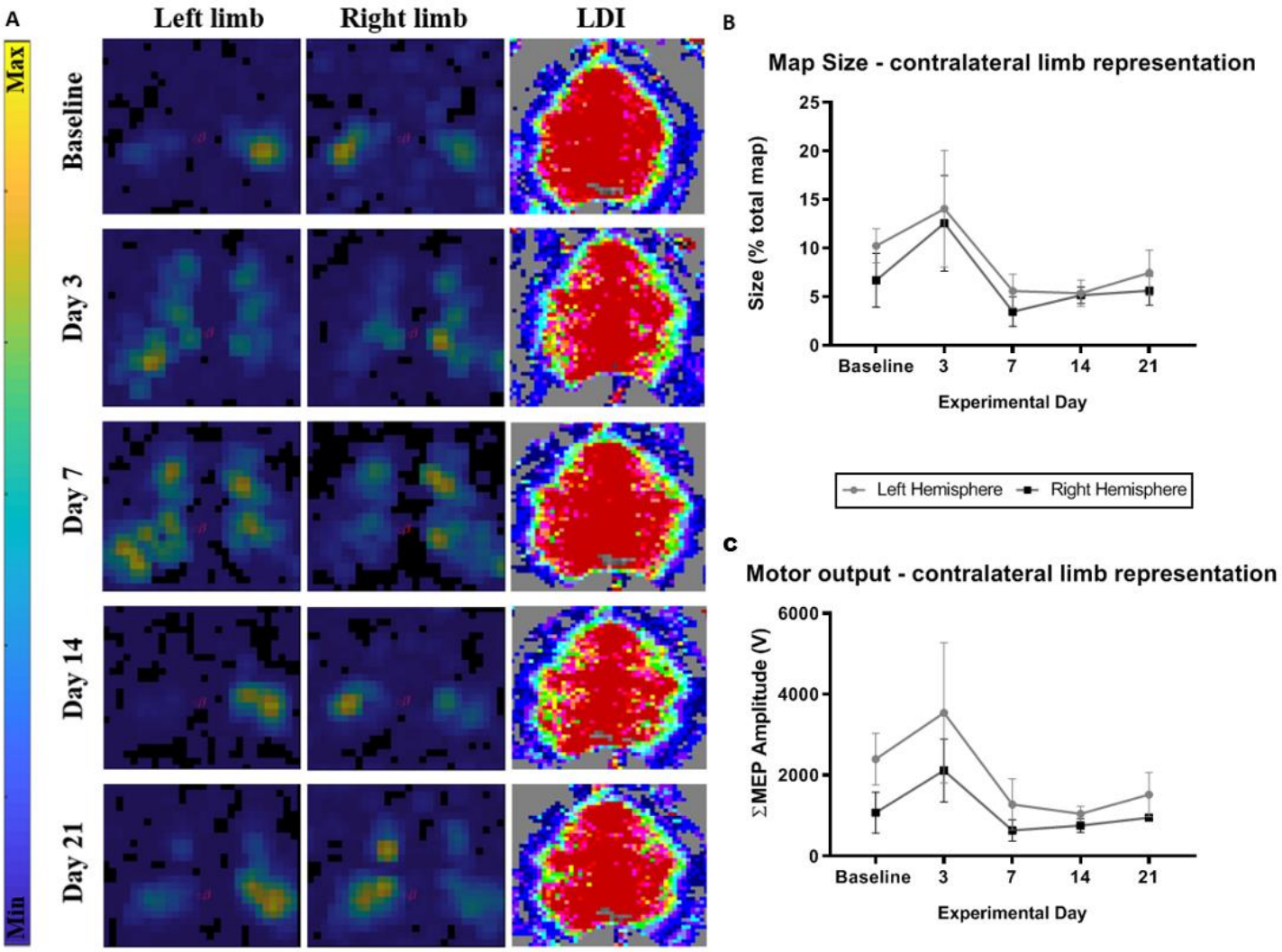

Figure 29. Motor mapping and laser Doppler imaging (LDI) of IVM mice. (A) Motor maps of a representative IVM mouse showing both left and right limb representations and LDI of the cortical blood flow imaged through the cranial windows at different time points. No significant differences were observed for motor map organization. (B) Average map size (% total map) for the right limb representation (C) followed by the average motor output (MEP: motor evoked potentials). No significant differences were observed for motor map organization (p=0.9329) or motor output (p=0.8077). Values are presented as sample means ± SEM (Motor mapping & LDI n=3; NDS n=4).